Design and Analysis of Cascaded Fiber Bragg Grating Structures for Optical Transmission System

THESIS

Submitted in partial fulfilment
of the requirements for the degree of

DOCTOR OF PHILOSOPHY

by

Chaluvadi V Naga Bhaskar

ID No. 2019PHXF0058H

Under the Supervision of

Prof. Prasant Kumar Pattnaik

and

Under the Co-supervision of

Prof. Subhradeep Pal

BITS Pilani
Pilani | Dubai | Goa | Hyderabad

BIRLA INSTITUTE OF TECHNOLOGY AND SCIENCE - PILANI
2024

BIRLA INSTITUTE OF TECHNOLOGY AND SCIENCE - PILANI

CERTIFICATE

This is to certify that the thesis entitled "Design and Analysis of Cascaded Fiber Bragg Grating Structures for Optical Transmission System submitted by Mr. Chaluvadi V Naga Bhaskar , ID No. 2019PHXF0058H for the award of Ph.D. of the Institute embodies original work done by him under our supervision.

Prasant Kumar Pattnaik

Supervisor

Prof. Prasant Kumar Pattnaik

Associate Professor

BITS-Pilani, Hyderabad Campus

Date: 21/03/2024

Subhradeep Pal

Co-Supervisor

Prof. Subhradeep Pal

Assistant Professor

BITS-Pilani, Hyderabad Campus

Date: 21/03/2024

Acknowledgements

In my Ph.D. work, I met many people whose support helped me complete this research work smoothly. In this context, I'm taking the opportunity to acknowledge them all from the bottom of my heart. First and foremost, I would like to express my sincere gratitude to my respectable supervisor Prof. Prasant Kumar Pattnaik, and co-supervisor, Prof. Subhradeep Pal, for their guidance, help, motivation, and unwavering support throughout my thesis. The guidance I have received from them is not limited to the thesis but also to real life. Without their valuable suggestions, this thesis would not be an asset to me. I'm indebted to them for their valuable time spared for me during this work.

I am thankful to Prof. Soumyo Mukherji and Prof. G. Sundar, the present and former Director of BITS-Pilani, Hyderabad campus, respectively, for allowing me to avail of the institute facilities, stipend and financial support for publishing papers. I am grateful to Prof. Alivelu Manga Parimi and Prof. Vamsi Krishna Venuganti, the present and former Associate Dean (AGSRD), and the EEE Doctoral Research Committee (DRC) for their extended support.

I would like to convey my heartfelt thanks to the Doctoral Advisory Committee (DAC): Prof. Sanket Goel and Prof. BVVSN. Prabhakar Rao for their invaluable discussions, help, and continued support. My heartfelt thanks to Prof. Alivelu Manga Parimi and Prof. Subhendu Kumar Sahoo, the former and present heads of the Department of Electrical and Electronics Engineering, respectively, for their help and timely support.

I am also thankful to my fellow doctoral students for their encouragement and support. In particular, I am thankful to my senior, Dr. Samit Kumar Goshfor his help, encouragement and motivation during this journey. I would like to convey my sincere thanks to the entire EEE department, including lab technicians and office assistants for their extended help and support.

My heartfelt acknowledgements to my parents Mrs. Baparatnam chaluvadi and Late Mr. Radha Krishna Chaluvadi, for their unconditional love, motivation, and affection. I would like to acknowledge my beloved brother Mr. Naga Praveen Kumar Chaluvadi for caring about parents and me in all aspects, especially during difficult times in life. I also thank all my family members and friends, who have been supportive and caring.

Last but not least, I would like to thank the administration, library staff, hostel staff, security staff, and workers for their help in various ways during my stay on the lovely campus. Finally, I would like to say my sincere thanks to God almighty for everything that I'm blessed with.

Chaluvadi V Naga Bhaskar

Abstract

Fiber Bragg gratings or FBGs are the passive optical devices formed inside the core of an optical fiber (single mode or multi-mode fiber) by varying the refractive index of the core over some finite length. The reflected light from an FBG can be analyzed to obtain valuable information about the fiber itself or its surrounding environment. This characteristic makes FBGs particularly useful for various sensing applications. However, FBGs have also found extensive use in the field of telecommunications. The key applications of FBGs in communications include gain equalizers, optical filters, dispersion compensation, and wavelength selective components in WDM systems, etc. Nowadays, optical transmission systems are used in long-haul communication links such as submarine cables and intercontinental connections. Enhancing the performance of optical transmission systems allows for longer transmission distances without significant signal degradation, enabling the expansion of global communication networks. Furthermore, improving the performance of optical transmission systems enables faster and more effective data transfer, meeting the rising data needs of modern communication networks.Therefore, to improve the optical transmission system performance, researchers are presently creating a variety of cascaded FBG structures with the aid of the FBG technology.

The desired spectral characteristics of the cascaded FBG structures usually need a narrow bandwidth and minimal number of side-lobes with maximum peak reflectivity in the reflected spectrum for communication or sensing purposes. Often, as the number of cascaded FBGs in the structure increases, reflectivity decreases with reduced full width at half maximum or FWHM and the number of side lobes. In order to improve the reflectivity and narrower FWHM, a cascaded FBG structure has been proposed. Such a proposed structure utilizes cascaded uniform or apodized FBGs of varying lengths works in the C-band are analyzed and simulated. In addition to the uniform or apodized FBGs, we have also formed cascaded structures with chirped FBGs (CFBGs) or apodized CFBGs. In each FBG

or CFBG structure, the reflected signal from the current FBG is utilized as input to the subsequent FBG or CFBG in the structure. The reason for using CFBGs or non-uniformity gratings in the core is to reduce the side lobes in the reflection spectrum, which are undesirable as in their uniform counterpart. They are also used for dispersion compensation and pulse shaping purposes. Compared to the CFBGs, apodized linearly chirped fiber Bragg gratings (LCFBG) have proved to be an effective solution to compensate for the chromatic dispersion of high bit-rate optical communication systems. Hence, we have also used cascading of apodized LCFBGs to get a narrow-band spectral profile. Analytical formulation based on the piecewise uniform approach or PUA approach of the proposed cascaded CFBG structure(s) is incorporated. Moreover, the effect of temperature on the proposed devices shifts the Bragg peak enabling it to be used for sensing purposes also presented.

In this work, initially, the design, analysis and simulation of various cascaded FBG or CFBG structures operated in the C-band are proposed. Subsequently, based on the better spectral characteristics of the proposed structures, we have used the same structure either in an optical transmission system or as a narrow-band filter for communication purposes. In particular, such a proposed structure with narrower FWHM has been placed immediately next to the optical source to reduce the source spectral width. Thus enhancing the system performance in terms of bit error rate or BER and Q-factor by reducing the dispersion in the fiber. Since the cascaded structure formed with apodized FBGs has given a narrower FWHM of 0.07 nm than any other structure. Such a cascaded structure integrated with the optical transmission system has given better performance thanin the absence of the structure. At the maximum operating distance, a BER of 9.5321×10^{-12} corresponding to a Q-factor of 6.712 has been attained with the proposed structure in the system.

Keywords: Fiber Bragg gratings, apodization, chirped FBGs, cascaded FBGs, FWHM, reflectivity, piecewise uniform approach, dispersion, BER.

Contents

List of Tables

List of Figures

List of Abbreviations

ASE	**A**mplified **S**pontaneous **E**mission
ATMM	**A**pproximated **T**ransfer **M**atrix **M**odel
CFBG	**C**hirped **F**iber **Bragg G**rating
CMT	**C**oupled **M**ode **T**heory
CTE	**C**oefficient of **T**hermal **E**xpansion
CW	**C**ontinuous **W**ave
DCF	**D**ispersion **C**ompensation **F**iber
DUT	**D**evice **U**nder **T**est
DWDM	**D**ense **W**avelength **D**ivision **M**ultiplexing
EDFA	**E**rbium **D**oped **F**iber **A**mplifier
FBG	**F**iber **B**ragg **G**ratting
FBGRR	**F**iber **B**ragg **G**ratting **R**ing **R**esonator
FEM	**F**inite **E**lement **M**ethod
FWHM	**F**ull **W**idth at **H**alf **M**aximum
GI	**G**raded **I**ndex
GVD	**G**roup **V**elocity **D**ispersion
Hi-Bi FBG	**H**ighly **B**irefringent **F**iber **B**ragg **G**rating
IL	**I**nsertion **L**oss
ISI	**I**nter **S**ymbol **I**nterference
LDC	**L**inearly **D**ecreased **C**hirp
LIC	**L**inearly **I**ncreased **C**hirp

LPF	**L**ow **P**ass **F**ilter
MMF	**M**ulti **M**ode **F**iber
MZ	**M**ach **Z**ehnder
NF	**N**oise **F**igure
NRZ	**N**on **R**eturn to **Z**ero
OADM	**O**ptical **A**dd **D**rop **M**ultiplexer
OFC	**O**ptical **F**iber **C**ommunications
OSA	**O**ptical **S**pectrum **A**nalyzer
PAM	**P**ulse **A**mplitude **M**odulation
PD	**P**hoto **D**etector
PMMA	**P**oly **M**ethyl **M**eth **A**crylate
POF	**P**olymer **O**ptical **F**iber
PS-FBG	**P**hase **S**hifted- **F**iber **B**ragg **G**rating
PUA	**P**iecewise **U**niform **A**pproach
ROGUE	**R**andom **O**ptical **G**rating by **U**ltroviolet **L**aser **E**xposure
r.i.	**r**efractive **i**ndex
SHM	**S**tructural **H**ealth **M**onitoring
SLSR	**S**ide **L**obe **S**uppression **R**atio
SMF	**S**ingle **M**ode **F**iber
SSMF	**S**tandard **S**ingle **M**ode **F**iber
WDM	**W**avelength **D**ivision **M**ultiplexing

Chapter 1

Introduction

This chapter gives a brief introduction to the work presented in this thesis. The fundamental description of the fiber Bragg grating or FBG and the numerous applications of this technology are explored in Section 1.1. In Section 1.2, a brief mathematical background on FBG, while the classifications of FBG are discussed in Section 1.3. Measurement of temperature and strain with generalized analysis is presented in Section 1.4 and Section 1.5, respectively. A comparative study between the various recently reported FBG based temperature and strain sensors is compared within the respective sections. Also, we have incorporated the recently reported cascaded FBG based devices for filtering or communication purposes in section 1.6. Finally, the chapter ends with the description of the motivation, organization and scope of the thesis.

1.1 Fiber Bragg gratings and their applications

The fiber Bragg gratings (FBGs), a passive optical device, contain a periodic refractive index (RI) modulations in the core of an optical fiber (single mode or multi-mode fiber) over

some finite length [1, 2, 3]. These periodic RI variations are usually a perturbation in the photosensitivity property of the core of the fiber. These periodic variations can be formed by utilizing a number of techniques including holographic [4], phase mask [5], and point-by-point techniques [6]. FBGs owing to their primary advantages like high sensitivity and resolution, lightweight, and wide dynamic range, finds tremendous applications as sensors in various fields of measurement, as dispersion compensating elements in optical fiber transmission systems.Also, FBGs are currently deployed in different sectors such as oil and gas [7, 8, 9, 10, 11], civil [12, 13, 14, 15], industrial [16, 17, 18, 19], energy [20, 21, 22, 23], biomedical [24, 25, 26, 27], aerospace [28, 29, 30, 31], transport [32, 33, 34], and optical communications [35, 36, 37] etc. In the oil and gas sector, FBGs are used for monitoring pipeline related problems, temperature and gas pressure measurement, oil density measurement, and detection of gases in oils, etc. In civil, FBGs are mainly used for Structural Health Monitoring (SHM) of structures. In industry apart from sensing and SHM, FBGs are also used to measure AC current or voltage signals [17], and physical parameters like strain and stress [38]. In the energy sector, FBGs can be used for monitoring the mechanical behavior of wind turbine blades, bending deflection of wind turbine towers, pressure measurement in geothermal wells [20, 21, 22, 23]. In biomedical sector, FBGs are primarily used for cardiovascular diagnostics, gastroenterology, urology, neurologic diagnostics, blood pressure monitoring, and endoscopic purposes [24]. Similarly, SHM of aircraft structures [30, 31] and in-flight load measurement [29] are two important applications of FBGs in aerospace sector. Furthermore, FBGs can be utilized to track trains, detect subway incursions, defect identification of train wheels, and to monitor health of the tracks which extends the applications in the transportation sector [32, 33, 34]. In optical fiber transmission systems, FBGs are mainly used for dispersion compensation [35, 39], filtering [37], gain equalizing [40], and optical add-drop multiplexing (OADM) in WDM systems [36].

In these applications, SHM requires accurate measurement of strain [12, 13, 14, 21, 28, 41] which can be easily achieved by FBGs. Also, temperature measurement for safety and stability purposes in various industrial sectors is necessary [18, 19, 25, 42]. In this chapter,

our objective is to review the various techniques to measure the temperature and strain using FBGs in different industrial sectors. An In-depth analysis of FBG is also incorporated in relevant sections to fully analyze the performance of the FBGs in such a measurement scheme. We have also done a comparative analysis of the various FBG based temperature measurement and strain measurements. Also, we have incorporated the recently reported cascaded FBG based devices for filtering or communication purposes.

1.2 Mathematical foundation of FBG

Refer to Fig. 1.1 which depicts a simple FBG with a grating period Λ and grating length L. Assume the RI profile along the longitudinal direction (z) can be modelled using the following relation [43],

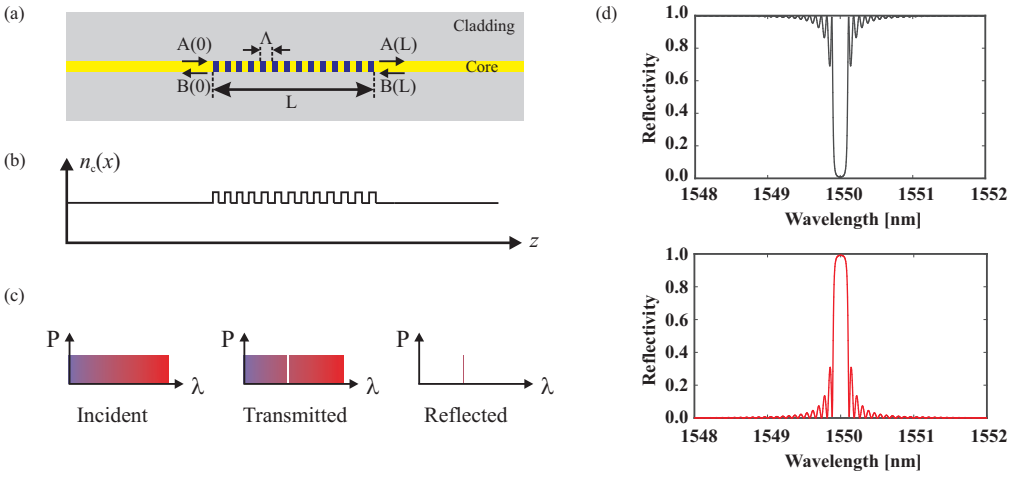

Figure 1.1: Schematic of an fiber Bragg grating sensor: (a) structure of a conventional FBG with different notations used for analytical formulation; (b) RI profile of the core region of the FBG; (c) ideal spectrum of the incident, transmitted, and reflected signal into a ideal FBG; (d) simulated transmitted (in grey) and reflected signal (in red) spectrum from a realistic FBG.

$$n(z) = n_c + \delta n \left[1 + \cos\left(\frac{2\pi z}{\Lambda}\right)\right] \tag{1.1}$$

where δn denotes the strength of RI perturbation while n_c is RI of the fiber core. The frequency selectivity of an FBG originates from the multiple Fresnel's reflections from the index perturbations and their coherent interference. For simple coupled-mode analysis, let us consider the forward and backward propagating wave to be denoted as $A(z)$ and $B(z)$, and they can be represented as [43, 44],

$$\frac{dA(z)}{dz} = -j\Delta\beta A(z) - j\kappa B(z) \tag{1.2}$$

$$\frac{dB(z)}{dz} = j\Delta\beta B(z) + j\kappa A(z) \tag{1.3}$$

Here $\kappa \simeq \pi(1 - V^{-2})\delta n\lambda^{-1}$ is the coupling coefficient between forward and backward waves, δn denotes the strength of RI perturbation, V is the V-number of the fiber, $\Delta\beta = \beta - \pi/\Lambda$ is the difference between the propagation constants along the longitudinal direction (z-direction) and Λ denotes the grating period .Solving the coupled mode equation we get,

$$\begin{bmatrix} A(L) \\ B(L) \end{bmatrix} = \begin{bmatrix} S_{11} & S_{12} \\ S_{21} & S_{22} \end{bmatrix} \begin{bmatrix} A(0) \\ B(0) \end{bmatrix} \tag{1.4}$$

where the scattering matrix (S) - parameters for the FBG are,

$$S_{11} = \frac{e^{\gamma L} - \rho^2 e^{-\gamma L}}{1 - \rho^2} \tag{1.5}$$

$$S_{12} = \frac{\rho(e^{-\gamma L} - e^{\gamma L})}{1 - \rho^2} = -S_{21} \tag{1.6}$$

$$S_{22} = \frac{e^{-\gamma L} - \rho^2 e^{\gamma L}}{1 - \rho^2} \tag{1.7}$$

Here, the amplitude reflectivity $\rho = j(\Delta\beta + \gamma)/\kappa$ and the parameter $\gamma = \sqrt{\kappa^2 - \Delta\beta^2}$. Similar analysis as mentioned in [43],S-parameters provide information about reflection and transmission characteristics of the FBG at each port. In a four port FBG device, each port represents a different optical path. Usually, these parameters can describe how light is reflected and transmitted between these ports, allowing for a comprehensive understanding of device's optical behaviour. For example, S_{11},S_{22} represents the reflection coefficient at port

1 and port 2 respectively whereas S_{21} and S_{12} denotes the transmission coefficients from port 1 to port 2 and port 2 to port 1 respectively. Similarly, one can use the S-parameter measurements to validate theoretical models, refine device designs, and optimize the parameters such as grating length, apodization profile, or coupling coefficients leading to the development of more efficient and reliable optical devices. The reflectivity of the FBG can be represented as [43],

$$R = -\frac{S_{21}}{S_{22}} = \rho \left[\frac{e^{-2\gamma L - 1}}{e^{-2\gamma L} - \rho^2} \right] \tag{1.8}$$

The power reflectivity and phase shift introduced by the FBG has band-pass characteristics and quasi-linear response near the Bragg-wavelength $\lambda_B = 2\Lambda n_{eff}$. Where n_{eff} is the effective refractive index of the mode travelling through the grating. The corresponding full width at half maximum (FWHM) of the power reflectivity spectra is given by [44],

$$\Delta\lambda = \frac{\lambda^2}{2\pi n_{eff} L} \sqrt{\pi^2 + \kappa^2 L^2} \tag{1.9}$$

Similarly, the nearest notch (λ_n) of the peak reflectivity can be written as [44],

$$\lambda_n = \lambda_B \left[1 + \frac{\lambda_B \Delta\beta}{2\pi n_{eff}} \right] \tag{1.10}$$

For the non-uniform coupling coefficient ($\kappa(z)$) and or grating period ($\Lambda(z)$), a similar kind of analysis can be made to calculate the various parameters of FBG. Such FBGs can be modelled using a large number of short sections considering κ and Λ constant within each section. The transfer-matrix relations for such FBG can be written as [43],

$$\begin{bmatrix} A(L) \\ B(L) \end{bmatrix} = \left(\prod_{m=1}^{N} \begin{bmatrix} S_{11}^m & S_{12}^m \\ S_{21}^m & S_{22}^m \end{bmatrix} \right) \begin{bmatrix} A(0) \\ B(0) \end{bmatrix} \tag{1.11}$$

A similar kind of formulation analysing the performance of FBG subject to external non-uniform strain will be discussed later in this chapter.

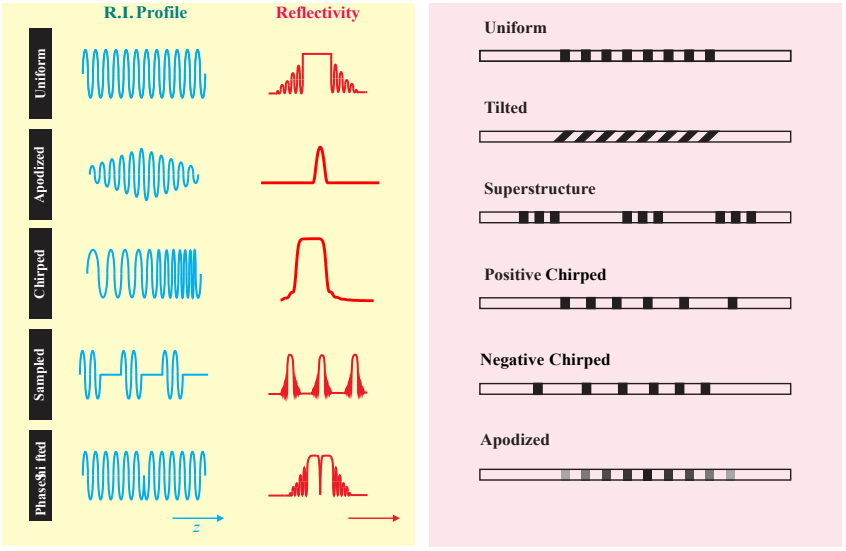

Figure 1.2: Some commonly used primary FBGs in single mode fiber: (a) the RI profile as a function of length of the fiber gratings with its expected wavelength dependent reflectivity; (b) schematic of the core region of the single mode fiber subjected to different index perturbation in some common FBGs.

1.3 Classification of FBGs

Generally, the FBGs can be inscribed in both single-mode fibers (SMF) and multi-mode fibers (MMF), while the RI profile of such fiber may be either step-index (SI) or graded-index (GI). Depending on the inscription in the core of the fiber, FBGs can be categorized into single-mode FBGs (SM-FBGs), and multi-mode FBGs (MM-FBGs) [3]. Single-mode FBGs can be further classified into primary FBGs (type-I FBGs or standard gratings) and secondary FBGs (secondary-type-In gratings). In this section, we have classified and briefly discussed the various SM-FBGs.

1.3.1 Primary Gratings

Primary FBGs or type-I FBGs, can generally be sub-categorized into uniform, apodized, chirped, super-structure, phase-shifted, tilted FBGs, and ROGUE gratings [44, 45, 46] and

typically they can operate up to $350°$C [47]. Fig. 1.2 represents the schematic of RI profile and its reflectivity as a function of wavelength for some commonly used FBGs. Another couple of variants of such primary FBG is Type-Ia and Type-II. Type-Ia FBGs are typically formed in hydrogen-loaded fibers, and it supports operating temperature up to $500°$C while type-II FBGs find application up to $1000°$C. It is interesting to note that type-II FBGs offer better thermal performance as a result of physical damage-based periodical design [47]. Type-I gratings result from the color variation center and the related modification of the absorption spectrum. Despite the better thermal performance,type-II suffers from a bad spectral response of the reflected light which limits the sensor's performance. Additionally, type-II FBG offers high loss in the lower wavelength range, making it unsuitable for multiplexed sensor arrays. However, type-IIa FBGs, a new variant, offer thermal performance in between type-I and type-II with respect to temperature stability [48]. Generally, primary FBGs are used for both communication and sensing applications, whereas secondary FBGs find applications in sensing and fiber lasers. However, it is interesting to note that multimode copper-coated FBGs offer better sensitivity compared to its single-mode counterpart in the case of temperature measurements [3].

In the uniform gratings, the grating pitch or period remains unchanged throughout the device length. In the case of apodized gratings, the grating period remains constant while the RI profile varies along the grating length. Such RI profile may modelled as Gaussian or raised cosine function [44]. These gratings exhibit lower index modulation strength towards the edges than compared with the central region. As a result, a lower Fresnel's reflection will occur at the edges of the Bragg wavelength (λ_B) compared to the uniform gratings. Thus, apodized gratings are useful in suppressing the side lobes of the reflected signal [49]. Advanced apodization techniques, such as chirped or tapered apodization, further enhance side-lobe suppression compared to uniform gratings. Similarly, advanced apodized gratings can achieve ultra-narrow bandwidths, making them suitable for applications requiring high-resolution spectral filtering, such as wavelength-division multiplexing (WDM), fiber lasers,

and optical coherence tomography (OCT) systems. In chirped FBGs (CFBG), a linear variation in the grating pitch is achieved by varying the RI profile of the grating or varying the effective RI along the direction of propagation. The non-uniform pitch could be considered as several FBGs cascaded with variations in the grating pitches in each sub-FBGs. If the grating pitch varies linearly, then the reflected signal from the CFBG also varies linearly, which results in the broadening of the reflected spectrum. Generally, these kinds of gratings are used for compensating dispersion in optical transmission systems [25, 50].

Super-structured FBGs can be modelled as several FBGs with periodic RI variation is connected to one another in close vicinity. Because of the comb-like filter response of such FBGs, they can be used as optical filters in transmission networks and in optical sensor systems [51]. Such FBGs also enable multichannel applications like multichannel multiplexers-demultiplexers, multichannel dispersion compensation, and so on in DWDM systems [52]. Super-structured can serve multiple functions within a single grating structure. By incorporating complex modulation patterns or multiple sections with different properties, they can simultaneously perform functions such as dispersion compensation, spectral shaping, polarization control, and mode conversion. Some super-structured gratings can exhibit adaptive or reconfigurable properties, allowing for dynamic control of their spectral or dispersion characteristics. This capability enables tunable filtering, dispersion compensation, and wavelength-selective switching, offering flexibility in optical network architectures and reconfigurable photonic devices. In a π-phase shifted FBG, 180° phase shift is introduced at the center of the periodic gratings, which enables practical realization of narrowband transmission filters at the desired operating wavelength. Depending on the location and the amount of phase shift introduced by the RI perturbation in the FBG, the narrowband notch characteristics can be changed using these gratings [53]. These gratings can be used to generate non-linear phenomena such as four-wave mixing (FWM), self-phase modulation (SPM), and cross-phase modulation (XPM) in optical fibers, enabling applications in non-linear optics and signal processing due to their complex phase profiles. Similarly, with these gratings one can achieve ultra-narrow bandwidths, making them suitable for

applications requiring high-resolution spectral filtering, such as wavelength-division multiplexing (WDM), fiber lasers, and optical sensing systems.

For the tilted FBGs, the index perturbation oriented at a finite and predetermined angle with respect to the fiber axis. By doing so, we can gain control over the coupling strength and λ_B. Furthermore, mode coupling can also be improved to some degree of extent by using these types of FBGs [54]. These tilted gratings can exhibit polarization-dependent characteristics due to the tilted geometry of the grating structure. This polarization sensitivity enables polarization control and manipulation, making tilted gratings useful in polarization-maintaining fiber systems and polarization-sensitive devices. Long period gratings (LPGs) are optical fiber devices characterized by periodic variations in the refractive index over a longer length scale compared to traditional fiber Bragg gratings (FBGs). The period of these variations typically ranges from hundreds of micrometers to several millimeters. Unlike FBGs, which rely on the Bragg scattering phenomenon, LPGs operate based on the coupling of light between the core mode and the cladding modes of the optical fiber. LPGs are commonly used as wavelength-selective filters in optical communication systems. They can selectively attenuate or transmit specific wavelengths of light based on the resonance condition between the core mode and cladding modes. On the other hand, Long period gratings are employed in fiber-optic sensors for various sensing applications. These gratings are sensitive to external perturbations such as temperature, strain, pressure, refractive index changes, and bending. LPG-based sensors are used in structural health monitoring, environmental sensing, biomedical sensing, and industrial process monitoring. Alternatively, LPGs are incorporated into fiber lasers and amplifiers for spectral shaping, mode selection, and stabilization. They enable control over the laser output characteristics, such as wavelength stability, linewidth, and spectral purity, contributing to the performance optimization of fiber-based laser systems.

Another new variant of FBG is Random Optical Grating by Ultraviolet or ultrafast laser

Exposure (ROGUE). From eqn. (1.9), it is evident that $\Delta\lambda$ is inversely related to L. Interestingly in the case of ROGUE FBGs, $\Delta\lambda$ is independent of L. Such type of FBGs can be utilized to improve the accuracy and precision of strain, and temperature sensing [46]. This new type of structure offers a backscatter cross-section, usually several orders of magnitude higher than SMF-28 optical fiber, turning it ideal for sensing applications. The technology that achieves those new sensing properties consists of adding noise when writing FBG in the core, thereby creating a ROGUE, a grating with a very broadband, very short FBG-like spectrum that can spread an indefinite length. In particular, the amplitude and frequency of the noise added during the writing process are usually generated from the function generator, much greater than the environmental noise, which will affect the amount of backscatter but has no impact on the bandwidth of the backscattered spectrum. This results in broadband reflected spectrum whose bandwidth is independent of grating length. The resulted spectrum can be modeled as a series of very small, randomly out-of-phase FBGs. This structure will give us a weak reflective grating whose reflectivity is more than typical Rayleigh backscatter but maintains a large bandwidth, unlike a typical long weak FBG. This kind of gratings can be used for distributed sensing using optical frequency domain reflectometry (OFDR), which allows a significant increase in signal-to-noise ratio for temperature and strain measurement [46].

1.3.2 Secondary Gratings

As discussed in the previous section, a new variant of type-IIa FBG offers thermal performance in between type-I and type-II FBGs [47, 48]. Grating stabilities higher than $500°$C is very common in such FBGs. It is important to note that such FBGs are generally associated with a negative refractive index change. Such a negative index variation introduces two important changes. As the temperature increases, the grating reflectivity starts reducing. Secondly, the reference Bragg wavelength observed during the writing process also starts to reduce as the temperature increases. Thus, type-IIa FBGs are also known to be the negative

index gratings. However, as the further temperature increases, a secondary grating growth can be observed. Such type-IIa FBGs offer a stable performance typically up to $1100°$C. As secondary Bragg grating growths are common in type-IIa FBGs, it is also known to be regenerated gratings. Regenerated FBG is usually fabricated by post-annealing on over-saturated type-I FBG written in a heavily hydrogen loaded fiber [47, 48]. However in recent years, this type-IIa FBGs are formed in different fibers including B/Ge or Sn/Ge co-doped fibers [55, 56], highly Ge-doped fibers [48], photonic crystal fibers [57], or in microfibers [58]. Even rare-earth-doped fibers can be used for type-IIa FBGs [59]. Such FBGs can be utilized in high-temperature resistant fiber lasers [60], thermally triggered lasers [61], and even in higher harmonic grating fiber lasers [62]. The further fabrication process can be well studied from [47].

1.4 Measurement of temperature using with FBGs

Measurement of temperature, a crucial parameter in various sectors of industries, can be done with the help of FBGs. Theoretically, both low and high temperatures can be measured using FBGs with equal accuracy. However, measurement of low temperature with FBGs poses some additional challenges compared to others. In this section, we shall discuss the FBG-based temperature sensors subjected to no variation in other physical parameters of the FBG.

1.4.1 Analytical formulation for temperature measurement

As discussed in Section 1.2, the Bragg wavelength (λ_B) of an FBG can be expressed as [5, 63],

$$\lambda_B(T) = 2n_{eff}(T)\Lambda(T) \tag{1.12}$$

Hence, a small change in operating temperature T will result a change in the peak wavelength which can be represented as [63],

$$\begin{aligned}\delta\lambda_B = \frac{\mathrm{d}\lambda_B}{\mathrm{d}T}\delta T &= 2\left(\Lambda\frac{\mathrm{d}n_{eff}}{\mathrm{d}T} + n_{eff}\frac{\mathrm{d}\Lambda}{\mathrm{d}T}\right)\delta T \\ &= \lambda_B\left(\frac{1}{n_{eff}}\frac{\mathrm{d}n_{eff}}{\mathrm{d}T} + \frac{1}{\Lambda}\frac{\mathrm{d}\Lambda}{\mathrm{d}T}\right)\delta T \end{aligned} \tag{1.13}$$

In the absence of any variation related to other physical parameters of the FBG, $\delta\lambda_B$ can be extended to [18, 63, 64],

$$\delta\lambda_B = \lambda_B(\alpha_{n,T} + \alpha_{\Lambda,T})\delta T = \lambda_B(\zeta + \beta_T)\delta T \simeq \lambda_B\,\xi\,\delta T \tag{1.14}$$

where β_T or $\alpha_{\Lambda,T}$ is the coefficient of thermal expansion (CTE), ζ or $\alpha_{n,T}$ is the thermo-optic coefficient, and ξ is the Bragg wavelength thermal coefficient which can be expressed as the sum of thermo-optic and thermal expansion coefficients. Therefore, $\delta\lambda_B$ in terms of wavelength temperature sensitivity ψ_T can be determined to be,

$$\delta\lambda_B = \psi_T\,\delta T \tag{1.15}$$

where $\psi_T = \lambda_B\,\xi$. At room temperature, the typical value of ψ_T for a bare FBG (inscribed in Ge-doped silica core) of Bragg wavelength 1.5 μm is approximately 13.7 pm/°C . In temperature measurements, ψ_T is weakly dependent on the temperature (above the ice temperature and up to the FBG upper-temperature limit of $\sim 10^3$ K). So, the change in the temperature can be retrieved directly from $\Delta\lambda_B$ [65],

$$\Delta T = \int \frac{1}{\psi_T(T)} d\lambda_B \cong \frac{\Delta\lambda_B}{\psi_T|_{avg}} \tag{1.16}$$

where $\Delta\lambda_B$ is the total Bragg wavelength change. This approximation works well for the temperatures above room temperature. For temperatures below the ice point, one cannot use a single value of wavelength temperature sensitivity as ζ, and ξ are changing with the

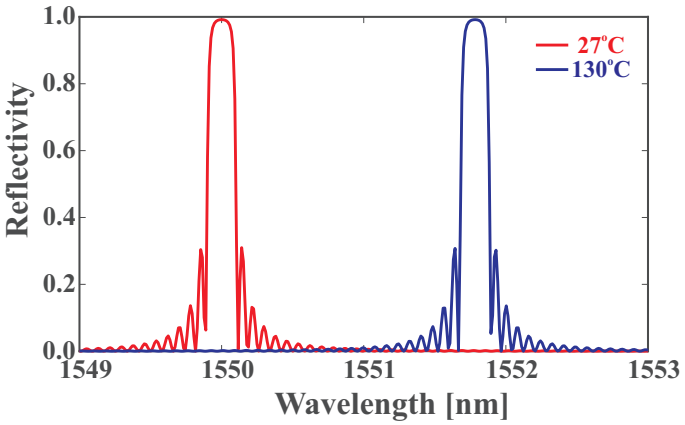

Figure 1.3: Effect of operating temperature variation in Bragg wavelength in a normal FBG. Consider 27°C is the reference temperature. λ_B shifted to 1551.78 nm from 1550.01 nm due to a change in temperature of 130°C. Other simulation parameters are: $L = 10$ mm, $\lambda_B = 1550.01$ nm, reflectivity at room temperature = 0.991, and $\kappa L = 3$.

temperature. Below the ice point temperature (273 K), the sensitivity of the sensor becomes poor. In such operating conditions, the sensor provides a non-linear response. FBG-based low temperature sensor response for different low temperatures are indicated in [66, 67, 68, 69, 70, 71, 72, 73]. The FBGs are generally used for temperature sensing at room and high temperature [66, 68, 74]. The effect of temperature on a standard FBG is simulated with the help of in-house MATLAB R2021a script and presented in Fig. 1.3.

1.4.2 Measurement procedure

Theoretically, the FBGs can also be used for low temperature (below the ice point) measurements. But, at low temperatures bare FBG sensitivity decreases as the temperature decreases [65, 66, 70, 73]. Due to this phenomenon, these sensors are not extensively used for low temperatures. However, the sensitivity of the bare FBGs for low-temperature measurements can be improved by coating the FBGs with different chemical materials, or polymers or even metals with different thermal expansion coefficients. This improvement

in the sensitivity at the cost of enhanced non-linear responses and hysteresis of the measurement system [65, 75]. The non-linearities primarily originate due to the temperature dependency of the thermal expansion coefficients of the coating material. A way around to these non-linearities, is to use the coated FBGs in a packaged form. However, this solution fails where the FBG is free to move. It is better to understand and model the thermo-opto-elastic properties of the fiber materials used in the FBGs and choose the suitable sensors as per the temperature. Such a solution will offer better performance, and the used FBG(s) can be bare, coated, embedded, or even etched.

In the case of FBG-based temperature sensors, one has to consider the material of the fiber since the property of the FBG will be strongly dependent on the chemical and thermal properties of the fiber core. Generally, the core of SSMF is made of Ge-doped silica, which offers almost 0.19 dB/km of attenuation in the C-band (1530-1565 nm). Such a fiber can be used to inscribe FBG for low- temperature measurement, while for measuring higher temperatures, the core material should be changed as per the requirement [63, 65]. Pure silica in low temperature offers a wide range of inertness to most of the other materials, making it suitable for measurement of the temperature of gases [65]. In such a case, FBGs can be either coated or bare. Together with cryogenic compatibility, bare FBGs can be used to achieve optical refrigeration of solids [65]. However, as mentioned earlier, the sensitivity to temperature of the wavelength of a conventional FBG reduces by five-fold at 77 K compared to the same at 295 K. This reduction in sensitivity is also accompanied by a non-linear sensor response around that temperature [65, 70, 72]. It is worthwhile to mention that the sensitivity parameter as reported in [65, 70, 71, 72, 73] varies widely due to different coatings, and materials of core of the fiber. On the other hand, measurement of room and high temperatures are more suitable with the standard silica fiber based FBGs [47, 61] which are readily available due to the recent developments in optical fiber based telecommunication devices.

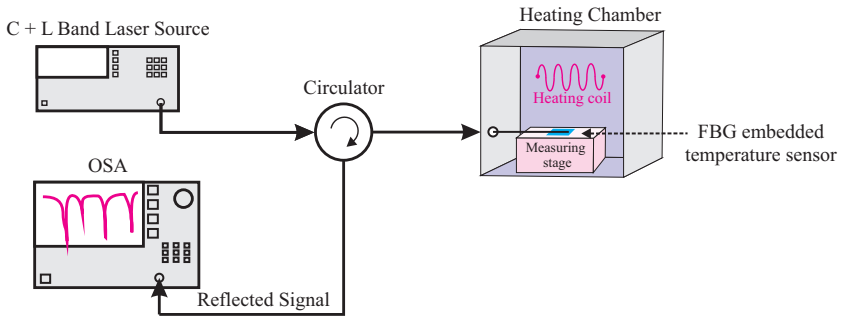

Figure 1.4: Schematic of temperature measurement using FBG based temperature sensor.

A typical system for measuring the temperature of a process or substance using an FBG-based sensor is depicted in Fig. 1.4. [65, 76]. A laser light source of C and/ L-band is connected to an optical circulator which is then connected to an FBG placed in a chamber whose temperature is required to be monitored. The other terminal of the circulator can be connected to an optical spectrum analyzer or OSA. Any change in the temperature in the chamber will impose a perturbation in the property of the FBG resulting in a change in the peak wavelength shift. Eqn. (1.12) can be utilized to understand the perturbation caused by the temperature change. Now this variation of the peak wavelength of the reflected signal can be identified using the OSA as described in [76]. Generally, this shift in the peak wavelength and change in operating temperature has a linear relationship between 313 K to 673 K as mentioned in [76]. However, other papers have even achieved a higher range by altering the core material or incorporating some foreign material coatings as described in [77, 78].

1.4.3 Comparative study of various FBG based temperature sensors

A comparative study of different FBG-based temperature sensors has been presented in Table-1.1. In Table-1.1, both low and high temperature measuring FBG-based sensors have been compared in terms of maximum and minimum temperature range, sensitivity, and resolutions. For measuring temperature ranging up to 1273 K, a linear cavity fiber-laser

coupled FBG-based temperature sensor has been reported in [79]. In this reported sensor, a quadratic relationship between λ_B and T has been observed over the temperature range between 273 K to 1273 K. However, the quadratic relationship can be approximated by a linear one without introducing significant error in the measurand over the range 573 K to 1273 K. The recorded sensitivity is found to be 15.9 pm/°C from the linear fitting. A novel FBG coated with molybdenum(Mo)-copper(Cu) functional gradient layer, and Ni protective layer can measure up to 800°C [80]. Such Ni-coating also ensures excellent thermal stability and thus improves the overall reliability of the sensor. In [81], a 3rd and 4th order FBGs are inscribed in SMF-28 fiber, which offers a sensitivity of 15 pm/°C and 13 pm/°C, respectively. Such a sensor can operate in the range 298 K to 1173 K. Distributed FBGs based temperature sensor can measure the temperature in the range of 473 K to 773 K under a challenging operating environment consisting of high-EMI, and high voltage [82]. Furthermore, sapphire fiber-based FBGs can be used for temperature measurements higher than 1273 K in harsh environments [77]. Due to sapphire's high melting point, optical transparency, and chemical stability, single-crystal optical fibers made with materials crystalline Al_2O_3, ZrO_2, Ta_2O_5, and graphite have been very attractive for the construction of FBG based temperature sensors for harsh environments [77, 83, 84, 85]. An FBG inscribed in sapphire fiber using line-by-line scanning method by a femtosecond (fs) laser can be used for the measurement of high temperature and strain sensing in harsh environment structural health monitoring [86]. The introduced sapphire FBG temperature sensing characteristics are observed up to 1873 K and have a given temperature and strain sensitivities of 34.96 pm/°C and 1.45 pm/$\mu\epsilon$ respectively.Alternatively, FBGs in a multimode single-crystalline air clad sapphire fiber used for the temperature sensing up to 2173 K shown in [97]. Such an FBG based sensor will give us a resolution of ± 1 K for temperatures greater than 1773 K with the introduced sapphire and due to the high refractive index of step (0.745 for the sapphire/air interface) and the large core diameter, the optical spectra of sapphire FBG differ from conventional single-mode FBG is emphasized and claim that the reflected spectrum of a sapphire FBG is broadband in nature. Further, it reports that due to the high refractive

Table 1.1: Performance comparison of various recently reported FBG-based temperature sensors in chronological order.

Year	Ref.	Measuring Temperature [K]		Sensitivity	Resolution
		Minimum	Maximum		
1998	[73]	4.2	350	-	-
2001	[70]	77	300	150 pm/K	-
2004	[67]	243	353	-	-
2011	[71]	77	300	12.85 pm/K	-
2014	[65]	77	-	-	0.25 K
2016	[87]	-	533	-	0.5°C
2016	[82]	473	773	13.2 pm/°C	-
2016	[78]	373	923	14 pm/°C	-
2018	[88]	298	453	48 pm/°C	-
2019	[89]	298	343	11 pm/°C	-
2019	[79]	573	1273	15.9 pm/°C	-
2020	[90]	300	700	14.42 pm/°C	6.3×10^{-7}°C
2020	[81]	298	1173	15 pm/°C	-
2020	[77]	-	1773	30 pm/°C	-
2021	[91]	78	298	10.71 pm/°C	-
2021	[92]	273	329	8.75 pm/°C	smaller than 1°C
2022	[93]	253	353	20.22 pm/°C	-
2022	[94]	318	348	13.5 pm/°C	0.74°C
2023	[95]	268.5	296.5	-0.057 pm/°C	3.49×10^{-4}°C
2023	[96]	293	723	15.17 pm/°C	-

index of the sapphires, FBGs inscribed in sapphire fibers are suitable to various environments to measure the temperature and strain. However, sapphire FBGs can also be used for distributed sensing to measure temperature in boilers at the commercial power plant is presented in [83].

Measuring moderate temperatures in the range of 298 K to 343 K using FBG-based sensor is reported in [89]. Such sensor offers a sensitivity of 11 pm/°C. For low temperatures, the temperature dependence of λ_B of the fiber Bragg gratings in the range of 4.2 K to 350 K for different fibers used in space applications is reported [73]. The authors also emphasized that gratings embedded in composite materials show the same Bragg wavelength dependence on temperature as their non-embedded counterparts. An FBG fixed on Teflon substrate can be used for low temperature sensing in the range of 77 K to 300 K and

has given a sensitivity of 150 pm/K at room temperature [70]. A non-linearity response of an FBG based sensor for different temperatures in the range of 243 K to 353 K has been used in [67]. The sensitivity given by a regular FBG can be enhanced to three times with a polymer-coated FBG used for cryogenic temperature sensing in the range of 77 K to 300 K. The sensitivity given by the sensor was found to be 12.85 pm/K [71]. The thermal sensitivity of an FBG based sensor can be modelled as non-linear due to the non-linearity of both thermal expansion and thermo-optic coefficients of fiber materials [65].

As discussed in the earlier sections, coating on the FBG can improve sensitivity and/or measurement range of temperature. In [78], a chromium nitride (CrN)-coated FBG sensor is compared with bare FBG in the temperature range of 373 K to 923 K and found that CrN coated FBG has given 14 pm/°C greater sensitivity compared to the bare FBG. An FBG coated with different metals (Ni, Al, Cu, Zn, Pb), and In with different thickness has been studied extensively in [98]. The optimized thickness of various materials for achieving maximum sensitivity at different fixed temperatures has also been reported in [98]. A high resolution FBG sensor operating in the range of 300 K to 700 K , has achieved a sensitivity of 14.42 pm/°C [90]. Twisted FBG can also be employed for temperature measurement up to 533 K [87]. Such a sensor can also be modelled using a Bayesian linear model. However, to increase the temperature-induced strain effect of FBG at cryogenic temperatures, a secondary material that has a higher thermal expansion coefficient than silica must be coated on FBG. So, the coated materials must have a higher thermal expansion coefficient to gain good thermal strain from the grating even at low temperatures and the coated materials must have higher Young's modulus and good adhesion to the bare FBG. Good adhesion generally indicates the good strain transfer to the FBG. Materials satisfying the above requirements are the polymers. Two polymer coatings that can be used to increase the thermal sensitivity are epoxy coating and acrylate recoating. A polymer resin was used as a coating material on FBG to improve the temperature sensitivity at cryogenic temperatures reported in [88]. Such a polymer coating on bare FBG improves thermal sensitivity by ten-fold. It also has a fair measurement range between 298 K to 453 K with improved sensitivity of 48 pm/°C,

and the problem of cross-sensitivity was solved byencapsulating the FBG sensor in an aluminum capillary tube is presented. An etched FBG coated with reduced graphene oxide offers a temperature sensitivity of 33 pm/°C, which is almost three times higher compared to the bare FBG [99]. An FBG coated with titanium nitride (TiN) using sputtering technology for cryogenic temperature sensing has developed. The developed sensor reflection spectrum is compared with the bare FBGs within a range of 78 to 298 K. Based on the results obtained, it emphasizes that TiN-coated FBG has given a sensitivity of 10.71 pm/°C has reported in [91]. However, a quasi distributed FBG sensing technique for thermal monitoring at various blind spots (critical non-monitored regions) of the data center environment has been presented in [92]. Such a technique can be used to sense the temperature variations during GPU and CPU stressing tests have been reported up to 329 K. The sensor has given a thermal sensitivity of 8.75 pm/°C with a resolution smaller than 1°C. On the other hand, an FBG based sensor system developed in [93] can be used to monitor the bolt loosen angle for the bride structures. Such a developed sensor prototype has also been tested up to a temperature of 353° with a sensitivity of 20.22 pm/°C. In [94], the experimental results show that the proposed sensor cascaded with FBG can measure the temperature up to 348 K with a sensitivity of FBG as 13.5 pm/°C and resolution of 0.74°. However, the temperature measurement range of a solc-like filter increased eight times by cascading the filter with an FBG is experimentally demonstrated in [95]. The measurement range of the proposed sensor is recorded as 268.5 K to 249.5 K with a sensitivity of -0.057 pm/°C. In [96], a sensor was introduced by merging of grapefruit photonic crystal fiber and FBG based on sagnac interferometer. The proposed sensor can measure temperature using FBG in the range of 293 K- 723 K with a sensitivity of 15.17 pm/°C. Furthermore, the deployment of a thermally regenerated packaged FBG to measure temperature in highly radiated and hazardous chemical environment applications like in a nuclear fuel cycle facility has been developed and presented in [100]. The sensor has given a Bragg wavelength shift of $\sim$35 pm for 1 megagray (MGy) accumulated gamma radiation dose. The average sensitivity and the operating lifetime of the grating were checked up to 1173 K.

1.5 Measurement of strain using with the FBGs

In this section, we discuss briefly both the measurement of uniform and non-uniform strain using the uniform FBGs. The requirement of thermal compensation for such measurement is also discussed here. Finally, comparative studies on the recent trends in FBG based strain measurement are also incorporated.

1.5.1 Analytical formulation for uniform strain measurement

When a finite amount of strain is applied on the FBG, which is kept at a constant temperature (T), the grating pitch and or effective RI(n_{eff}) in the grating region varies. This results in a shift in the reference Bragg wavelength ($\Delta\lambda_B$) which can be measured easily. Depending on the number of wavelength shifts, one can easily measure the applied strain and even determine its tensile or compressive nature. Now considering a variation in both applied uni-axial strain (ϵ) and operating temperature (ΔT), $\Delta\lambda_B$ can be estimated as [101],

$$\Delta\lambda_B = 2\left[\Lambda\frac{\partial n_{eff}}{\partial L} + n_{eff}\frac{\partial\Lambda}{\partial L}\right]\Delta L + 2\left[\Lambda\frac{\partial n_{eff}}{\partial T} + n_{eff}\frac{\partial\Lambda}{\partial T}\right]\Delta T \tag{1.17}$$

Assuming $\Delta T = 0$, and the linear elastic region of operation eqn.(1.17) reduces to,

$$\Delta\lambda_B = \lambda_B(1-\rho_e)\epsilon \tag{1.18}$$

where ρ_e is the effective elastic-optic constant and is given by [5, 101]:

$$\rho_e = \frac{n_{eff}^2}{2}(\rho_{12} - \sigma(\rho_{11}+\rho_{12})) \tag{1.19}$$

Here ρ_{11}, ρ_{12} are the coefficients of elastic-optic tensor and σ is the Poisson's ratio, respectively. For a typical SiO_2-based SMF, $\rho_{12} = 0.252$, $\rho_{11} = 0.113$, $\sigma = 0.16$ and

$n_{eff} = 1.482$. Plugging the values in the relevant equations, $\Delta\lambda_B$ for an applied strain of $1\ \mu\epsilon$ is 1.2 pm. It is important to note that n_{eff}, and the period of the grating planes, varies with temperature, which in return, alters λ_B. The fractional change in the wavelength shift to a temperature change ΔT can be written as [101]:

$$\Delta\lambda_B = \lambda_B(\beta_T + \zeta)\Delta T \tag{1.20}$$

For silica based fiber, $\beta_T \simeq 0.55 \times 10^{-6}$, denotes the thermal expansion coefficient and ζ is the thermo-optic coefficient which ranges near 8.6×10^{-6}. For a generalized definition of β_T and ζ one can use the following relations.

$$\beta_T = \frac{1}{\Lambda} \cdot \frac{\partial\Lambda}{\partial T} \tag{1.21}$$

$$\zeta = \frac{1}{n_{eff}} \cdot \frac{\partial n_{eff}}{\partial T} \tag{1.22}$$

Utilizing the eqn. (1.21), and (1.22), thermal sensitivity of λ_B is determined to be approximately 13.7 pm/°C. Finally, the sensitivity of the FBG sensor due to both strain and temperature can be written as [102, 103],

$$\frac{\Delta\lambda_B}{\lambda_B} = (1 - \rho_e)\epsilon + (\beta_T + \zeta)\Delta T \tag{1.23}$$

From eqn.(1.23), it is clear that $(\Delta\lambda_B)$ is interrelated between ϵ and ΔT. Thus, thermal compensation is required for measurement of strain.

1.5.2 Analytical formulation for non-uniform strain measurement

So far, we have considered a uniform strain distribution on the FBG, and thus, mathematical analysis becomes relatively easy. However, in a practical scenario, FBG based strain sensor

suffers from two significant problems. The first problem is that the strain and temperature collectively contribute to the peak wavelength shift. This problem is relatively easy to solve and will be discussed elaborately in the next subsection. The second problem with the FBG-based strain sensor is its response under non-uniform strain distribution on the FBG. We shall consider it in this section. Under uniform strain distribution, the peak wavelength shift in the reflected spectrum and applied strain is linear, which may not be true for the non-uniform strain distribution. An example of such a case is FBG in SHM, where FBG is embedded inside the composite material. Near to the crack or deformation in the material will results in non-uniform strain distribution resulting in a complicated strain measurement using the previous model. When subject to non-uniform strain fields, each segment of the FBG will experience a different strain and each segment will result in a different peak wavelength shift along the length of the sensor. As a result, the net shift of the peak wavelength subject to the linearised model will lead to a significant estimation error in the mean strain value [104]. This problem is also well addressed in [105, 106] for composite materials.

To tackle this problem, researchers have employed an approximated transfer matrix model (ATMM) of the conventional FBG and proposed a new algorithm to minimize the estimation error [104]. In the case of ATMM, it is assumed that traditional TMM can be employed if a sufficiently small segment of the FBG is considered. In case of TMM, the relation between the forward and backward propagating waves over the complete FBG is given by [104],

$$\begin{bmatrix} A_m \\ B_m \end{bmatrix} = \prod_{i=1}^{m} F_i \begin{bmatrix} A_0 \\ B_0 \end{bmatrix} \tag{1.24}$$

where F_i for each segment can be estimated as,

$$F_i = \begin{bmatrix} \cosh(\gamma_i \Delta z) - j\Delta\beta_i \gamma_i^{-1} \sinh(\gamma_i \Delta z) & -j\kappa_i \gamma_i^{-1} \sinh(\gamma_i \Delta z) \\ j\kappa_i \gamma_i^{-1} \sinh(\gamma_i \Delta z) & \cosh(\gamma_i \Delta z) + j\Delta\beta_i \gamma_i^{-1} \sinh(\gamma_i \Delta z) \end{bmatrix} \tag{1.25}$$

In the above eqn. (1.25), $\gamma_i = \sqrt{\kappa_i^2 - \Delta\beta_i^2}$, κ_i denotes coupling coefficient between forward and backward waves and $\Delta\beta_i$ is difference between the propagation constant along the longitudinal direction. The reflected spectrum can be determined as,

$$R(\lambda) = \left| \frac{F_{21}}{F_{11}} \right|^2 \tag{1.26}$$

In the case of ATMM model as described in [104], F_i for sufficiently small Δz can be rewritten as,

$$F_i \simeq \begin{bmatrix} e^{-j\Delta\beta_i\Delta z} & -j\kappa_i\Delta z \ \text{sinc}(\Delta\beta_i\Delta z) \\ j\kappa_i\Delta z \ \text{sinc}(\Delta\beta_i\Delta z) & e^{j\Delta\beta_i\Delta z} \end{bmatrix} \tag{1.27}$$

Further analysis for $R(\lambda)$ using a suitable new algorithm is presented in [104]. This ATMM also produces side lobes very closely matched with the practical results. This type of approximated model is also partially discussed in section 1.2.

1.5.3 Thermal compensation and other performance metrics

Direct measurement of strain or temperature requires protection for the device from the perturbation of the other variable. When FBG requires protection from strain, it can be easily achieved using certain methods. However, if one tries to measure strain, the operating temperature is required to be constant, which is not easy to achieve. This is due to the fact, as the measuring FBG (FBG1) generally not be placed inside a thermal encapsulation to protect it from varying operating temperature. An alternative way to achieve this is to employ another compensating FBG inside an encapsulation. This compensating FBG (FBG2) is connected in cascade with FBG1 and saved from any external strain. Any variation in strain and temperature for FBG1 will alter the value of λ_B of the same from its reference value, while in the case of FBG2 the same will be caused only due to a change in operating temperature. This can be well understood by using the following mathematical model [101,

107, 108]. The combined effect of strain and temperature on FBG1 can be written from eqn.(1.23) as

$$\Delta\lambda_{B1} = K_{\epsilon 1}\Delta\epsilon + K_{T1}\Delta T \tag{1.28}$$

where $K_{\epsilon 1} = (1 - \rho_e)\lambda_{B1}$, and $K_{T1} = (\beta_T + \zeta)\lambda_{B1}$. As there is no strain effect in FBG2, the shift in Bragg wavelength for the same can be expressed as,

$$\Delta\lambda_{B2} = K_{T2}\Delta T \tag{1.29}$$

where $K_{T2} = (\beta_T + \zeta)\lambda_{B2}$. However, the inherent assumption is that both FBG1 and FBG2 are made of same material and have similar design parameters. Rearranging eqn.(1.28) and eqn.(1.29) we have,

$$\begin{bmatrix} \Delta\epsilon \\ \Delta T \end{bmatrix} = \begin{bmatrix} K_{\epsilon 1} & K_{T1} \\ 0 & K_{T2} \end{bmatrix}^{-1} \begin{bmatrix} \Delta\lambda_{B1} \\ \Delta\lambda_{B2} \end{bmatrix} = \frac{1}{K_{\epsilon 1}K_{T2}} \begin{bmatrix} K_{T2}\,\Delta\lambda_{B1} - K_{T1}\,\Delta\lambda_{B2} \\ K_{\epsilon 1}\Delta\lambda_{B2} \end{bmatrix} \tag{1.30}$$

Solving for $\Delta\epsilon$, and ΔT results

$$\Delta\epsilon = \frac{1}{K_{\epsilon 1}K_{T2}}(K_{T2}\,\Delta\lambda_{B1} - K_{T1}\,\Delta\lambda_{B2}) \tag{1.31}$$

$$\Delta T = \frac{1}{K_{\epsilon 1}K_{T2}}(K_{\epsilon 1}\Delta\lambda_{B2}) \tag{1.32}$$

From the eqn.(1.31) the real strain applied over FBG1 can be estimated. Simulations using MATLAB R2021a is carried out to observe the effect of strain on an uniform FBG. For simulations, we have assumed the utilized single mode fiber is SMF-28. Clearly from Fig. 1.5, a shift of 1.2 nm in λ_B is observed with the application of ± 1000 $\mu\epsilon$ strain. Note that, the side lobes presented in the results are originating due to the periodic RI variations along the grating length as discussed in Section 1.2.

The performance of an FBG based sensor in most applications is usually expressed

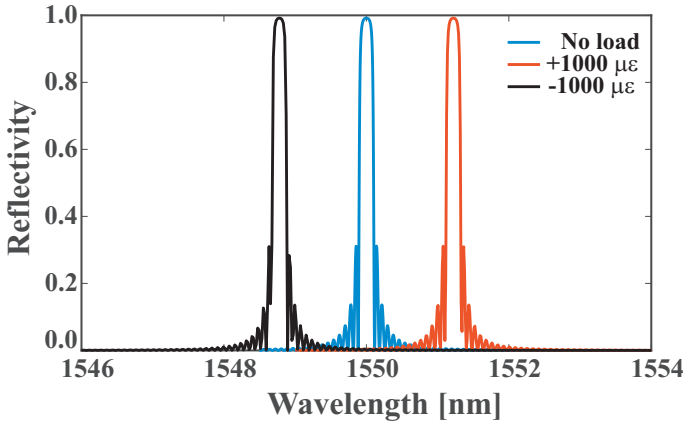

Figure 1.5: Variation in Bragg wavelength (λ_B) of a uniform FBG due to presence of tensile and compressive strain. Other simulation parameters are: grating length = 10 mm; $\lambda_B = 1550.0$ nm, reflectivity at zero strain = 0.991, $\kappa L = 3$. Note $+$ and $-$ sign denotes tensile and compressive strain, respectively.

in terms of sensitivity and resolution. A good FBG based sensor should offer both high sensitivity and high resolution. High sensitivity provides a significant change or a large shift in $\Delta\lambda_B$ even for small variations in the measurand. Mathematically it can be as a 'scale factor' when the sensor output varies linearly with the measurand. On the other hand, the resolution of a sensor is defined to be the smallest detectable change in the measurand. Apart from these parameters, the bandwidth and the accuracy of a measurement are the two other key factors of characterizing an FBG based sensor. With this basic concept, we now discuss two different classes of FBG-based strain sensors.

1.5.4 FBG embedded fiber ring resonator for strain measurement

In the FBG based all-fiber ring resonators (FBGRR), the FBGs are embedded in an optical fiber which is coupled to the other fibers using two different fiber-based couplers as shown in Fig. 1.6. Since a ring resonator structure itself is highly wavelength-dependent, their slight perturbation due to the applied strain will result in a high change in λ_B. For their excellent sensitivity and resolution, these types of FBG based strain sensors are widely used for SHM in civil infrastructures, energy, aerospace, and maritime operation fields [41]. Compared to the traditional FBG based strain sensor, FBGRRs are insensitive to environmental

disturbances resulting in reliable and accurate measurements [41, 109, 110, 111, 112]. In this structure, the resonance lines are formed by the two counter-propagating modes [41]. These resonance lines which are asymmetric in nature are also represented by improved cavity enhanced resolution. However, further improvement in the performance can be made by introducing π-phase shift in the middle position of the grating region as shown in Fig. 1.6(b). Similar other structures can be possible by extending the grating length throughout the entire ring region as depicted in Fig. 1.6 (c), and they are called extended FBGRR. Similarly, the design π-shifted FBGRR can be modified by extending the grating region as mentioned in extended FBGRR, shown in Fig. 1.6(d). These new structures improve the sensitivity and resolution immensely, as reported in [113, 114]. Mathematically, the transfer function of FBGRR can be expressed as [115],

$$T = \frac{1}{4}\left[\frac{\kappa^2 e^{-0.5j\beta L} a(t+r)}{1-\tau^2 e^{-j\beta L} a^2(t+r)} + \frac{\kappa^2 e^{-0.5j\beta L} a(t-r)}{1-\tau^2 e^{-j\beta L} a^2(t-r)}\right]^2 \tag{1.33}$$

where L represents the total resonator length, and a denotes the overall attenuation in the $L/2$ due to the attenuation of α per unit length. τ and κ are the coupling coefficient of the lossless coupler present in the structure. Similarly, t and r are the fractions of the optical field amplitudes transmitted and reflected via the FBG, respectively. Rigorous analysis for the sensitivity of this FBGRR in terms of strain can be expressed as [115],

$$\frac{\partial S_\lambda}{\partial \epsilon} = -\frac{\lambda^2}{\pi n L}\sqrt{\frac{R_\lambda}{1-R_\lambda}} \tag{1.34}$$

where n is the effective fiber RI Similar analysis for π-shifted FBGRR yields the transfer function to be,

$$T = \frac{1}{2}\left[-\frac{\kappa^2 e^{-0.5j\beta L}(t+r)}{1-\tau^2 e^{-j\beta L}(t+r)} + \frac{\kappa^2 e^{-0.5j\beta L}(r-t)}{1+\tau^2 e^{-j\beta L}(r-t)}\right] \tag{1.35}$$

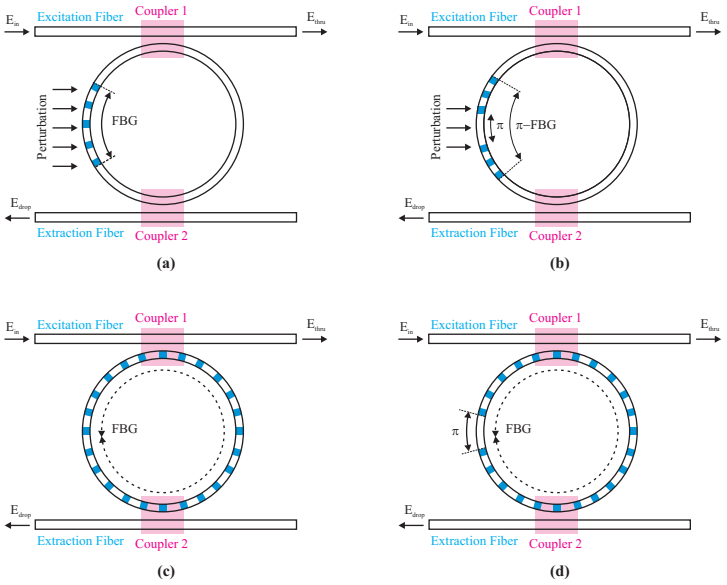

Figure 1.6: Schematic of different FBGs embedded fiber based ring resonator for strain measurement: (a) FBGRR; (b) π-FBGRR; (c) Extended FBGRR; (d) Extended π-FBGRR.

1.5.5 FBG embedded cantilever for strain measurement

Another technique of FBG based strain measurement employs a cantilever structure. In this technique, multiple π-phase shifted (PS) FBG are embedded in a cantilever as depicted in Fig. 1.7. A broadband source is connected to an optical circulator whose direct output is connected to the cantilever, and the return path is connected to an optical spectrum analyzer (OSA) [116]. The cantilever is being made of epoxy resin will bend subjected to external strain. This bending will also result in a change in strain on the bonded PS-FBGs and will result in a shift in the λ_B. Such change in λ_B can be easily detected with the connected OSA. Due to the usage of PS-FBGs, it is expected that the sensitivity and resolution of the complete setup will be good. In [116], the authors have reported a sensitivity of approximately 0.00124 nm/$\mu\epsilon$.

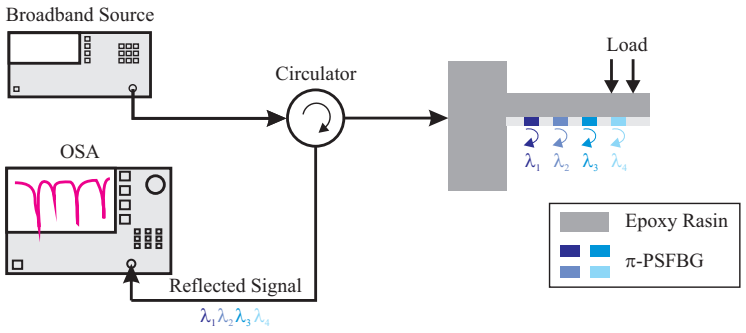

Figure 1.7: Schematic of π-PSFBG embedded cantilever based strain sensor.

1.5.6 Comparative Study of various FBG based strain sensor

The extraction of the measurand in terms of sensitivity and resolution from the measured reflected spectra obtained from the FBG-based strain sensor is another important aspect [41, 102, 117, 118, 119, 120]. A comparative study of recently reported FBG-based strain sensor are listed in Table-1.2.An SMF-based 3 mm long FBG offering a sensitivity, and resolution of 61.6 pm/$\mu\epsilon$, 700 nϵ, respectively, is reported in [124]. However, in [126] FBG based strain sensor offers approximately 1.65 pm/$\mu\epsilon$ of sensitivity for an etched region, and 1.24 pm/$\mu\epsilon$ for an un-etched region. A better sensitive strain sensor (with sensitivity 4.5 pm/$\mu\epsilon$) compared to [126] is reported in [125]. A dual-FBG based strain sensor in Polymethyl methacrylate (PMMA) microstructured in a polymer optical fiber (POF) is presented in [122]. The measured sensitivity of such sensor is 0.73 pm/$\mu\epsilon$. Another variant of strain sensor as reported in [121] provided a sensitivity of 1.4 pm/$\mu\epsilon$.

Alternatively, a resolution of 10 nϵ can be achieved with the design mentioned in [123]. In [137], a fiber ring laser cavity has been proposed to measure the strain with respect to the beat frequencies. The strain monitoring sensitivities are found to be 0.511 kHz/$\mu\epsilon$, -0.853 kHz/$\mu\epsilon$ and -1.606 kHz/$\mu\epsilon$ for beat frequencies of 0.429 GHz, 1.008 GHz, and 1.459 GHz, respectively.The proposed sensor in [131] has reported the maximum strain sensitivity of 37.5 pm/$\mu\epsilon$ while the same reported in [130] has achieved the sensitivity of 0.627 pm/$\mu\epsilon$ with the resolution of 27.95/$\mu\epsilon$. Similarly, in [138], the proposed sensor with a 3D

Table 1.2: Performance comparison of various recently reported FBG-based strain sensors in chronological order.

Year	Ref.	Sensitivity	Resolution
2010	[121]	1.4 pm/$\mu\epsilon$	-
2011	[122]	0.73 pm/$\mu\epsilon$	-
2013	[123]	-	10 nϵ
2014	[124]	104.1 pm/$\mu\epsilon$–Wavelength 61.6 pm/$\mu\epsilon$-FWHM	700 nϵ
2014	[125]	4.5 pm/$\mu\epsilon$	-
2014	[112]	-	320 p$\epsilon/\sqrt{Hz}$ at 0 Hz
2015	[120]	2.8 to 10.4 dB/nm	-
2016	[126]	1.65 pm/$\mu\epsilon$- etched region 1.24 pm/$\mu\epsilon$- un etched region	-
2016	[109]	2.86 pm/$\mu\epsilon$	-
2017	[127]	0.0762 pm/$\mu\epsilon$	13.13 $\mu\epsilon$
2017	[128]	5.24 pm/$\mu\epsilon$	-
2018	[129]	1.2 pm/$\mu\epsilon$	-
2020	[130]	0.627 pm/$\mu\epsilon$	27.95 $\mu\epsilon$
2020	[131]	37.5 pm/$\mu\epsilon$	-
2021	[132]	$\sim$6.65 pm/$\mu\epsilon$	$\sim$150 nϵ
2022	[133]	3.21 pm/$\mu\epsilon$	-
2022	[134]	1.14 pm/$\mu\epsilon$	-
2023	[135]	17.08 pm/$\mu\epsilon$	1.17$\mu\epsilon$
2023	[136]	33.22 pm/$\mu\epsilon$	-

printed spring is expected to measure an enormous strain ranging to $1.5 \times 10^7 \mu\epsilon$. Other designs employing a multi-core fiber inscribed with FBGs can be used as strain sensors to measure a multi-segment catheter's pose [139]. An FBG based stress sensor presented in [140] provides a way of online monitoring for the foundation deformation of transmission lines. A sensor reported in [112] is used to find out the high sensitivity strain in the low-frequency regime using π-phase-shifted FBG based on fiber ring cavity has a given a resolution of 320 p$\epsilon/\sqrt{Hz}$ at 0 Hz. The splitting variations due to the mechanical deformations of the grating can be tracked in real-time by interrogating a cavity resonance with a locked-carrier scanning-sideband technique demonstrated experimentally. However, a simple concept based on shifted optical Gaussian filters is used to interrogate a broad

spectrum of ultra FBGs for distributed measurements, giving a wide strain sensitivity tuning range from 2.8 to 10.4 dB/nm is presented in [120]. Similar to the sensor [112], coupled π-FBGRR introduced in [109] provides better performance than π-FBGRR for strain sensing. The splitting sensitivity of the sensor was found as 2.86 pm$/\mu\epsilon$. However, a short FBG inscribed in an MMF fiber has improved sensitivity to 5.24 pm$/\mu\epsilon$, to measure the strain experimentally with a single core resonance mode at high temperature (600 - 900°C) is presented in [128]. A polymer-coated silica FBG sensor has been designed to detect the immense strain of composite material on a solid rocket motor (SRM). The strain sensitivity and resolution of the sensor are 0.0762 pm$/\mu\epsilon$ and 13.13 $/\mu\epsilon$, respectively [127]. In [129], type-II FBGs inscribed and demonstrated experimentally in multicore photonic crystal fiber made up of pure silica used for optical fiber sensing at high temperatures has given the strain sensitivity of 1.2 pm$/\mu\epsilon$. Alternatively, an etched FBG coated with nanolayer molybdenum disulfide (MoS_2) using physical vapor decomposition (PVD) is highly sensitive and consistent to be used in the applications like detection of seismic vibrations and underwater acoustic signals. With the help of this sensor, an intrinsic strain sensitivity of $\sim$6.65 pm$/\mu\epsilon$ with a resolution of $\sim$150 nϵ can be achieved with optimized MoS_2 coating is reported in [132]. On the other hand, a strain sensor of the substrate type with a sensitization structure proposed in [133] has given a strain sensitivity of 3.21 pm$/\mu\epsilon$. However, the impact load borne by landing gear during the take-off and landing of aircraft is an importantparameter in structural health monitoring. So, in [134], the package of the FBG strain sensor which takes carbon fiber as material of substrate authors designed can adapt to the flight environment of aircraft. The test results of the sensor performance show that the strain sensitivity of the sensor reaches 1.14 pm$/\mu\epsilon$, which is close to that of bare optic fibre, but much more reliable than bare optic fibre, can meet the monitoring requirements of engineering. Further, a sensor system proposed in [135] will give us high strain sensitivity and large measurement range by combining a Sagnac interferometer with polarization mode fiber and FBG. The strain sensitivity was recorded as 17.08 pm$/\mu\epsilon$ while the measurement range can be note as 0-5187$/\mu\epsilon$. Such a sensor has given a resolution of 1.17 $/\mu\epsilon$. In [136] , a vernier sensor basedon chirp grating – Fabry Perot Interferometer for the detection of small strain variation

in Lithium polymer battery has been experimentally demonstrated. Such a sensor has give a high strain sensitivity of 33.22 pm/$\mu\epsilon$.

Generally, to calibrate the FBG strain, bending deformation of the beam or strain gauge strain methods is in use. For example, calibration utilizing strain gauge strain requires the design of a strain calibration electrical circuit is an indirect method that leads to poor calibration will give us problems like low sensitivity and stress transfer. So, in [141], a direct and high-precision new calibration method based on optical amplification is proposed to calibrate the strain of an FBG. In particular, a strain calibration method based on the optical lever has been presented. An optical lever contains an instrument for calculating Young's elastic modulus, a meter ruler, some weight, a narrow line, and a micrometer. With the help of an optical lever, strain calibration of an FBG has performed both theoretically and experimentally shown. The experimental results give a strain calibration sensitivity of 1.13 pm/$\mu\epsilon$ using an optical lever at room temperature demonstrated. Alternatively, an FBG based strain sensor to measure the little amplitude micro-strain in harsh industrial conditions is reported [142]. Such a sensor can amplify the strain in the FBG area mechanically using an elastic substrate with a lever structure. The strain sensing principle of the reported sensor is analysed using material mechanics theory. Experimental tests and the finite element method (FEM) are used to validate the strain sensing model of the sensor. Such a sensor has given a better experimental strain sensitivity than the sensor developed in [141]. The value of the strain sensitivity offered by the sensor is found as 6.2 pm/$\mu\epsilon$.However, a novel FBG based sensor reported in [143]has given an experimental strain sensitivity of 10.84 pm/$\mu\epsilon$. Such a sensor is designed with the help of a flexible hinge bridge structure to measure the strain of a mechanical surface. The sensor's strain sensitization factor was determined theoretically using strain energy theory and the flexible matrix method. The sensor reported is best suited to accurate dynamic strain monitoring of mechanical structures in a temperature environment up to 338 K. In [144], a sensor has been proposed to monitor the strain in lithium-ion batteries for state estimation purposes in energy storage applications. The proposed sensor has given a strain sensitivity of 11.55 pm/$\mu\epsilon$, which is 11.55 times greater than a bare FBG

sensor. Such a sensor has given better strain sensitivity than compared to the sensor reported in [143].

In addition to the literature mentioned above, an FWHM used as a cross-sensitivity indicator for simultaneous measurement of temperature and strain using a single FBG on tilted cantilever beam has been proposed recently in [145]. Such a proposed sensor has given a temperature sensitivity of 14.2 pm/°C with no change in FWHM and strain sensitivity of 0.453 pm/$\mu\epsilon$ with a change in FWHM given by a quadratic equation presented. However, to discriminate the cross-sensitivity problem for the simultaneous measurement of temperature and strain, a tilted FBG sensor with a tilt angle of 5° has been designed using optigrating software [146]. The developed sensor has given a strain sensitivity of 1.25 pm/$\mu\epsilon$ within a range 0 to 500 $\mu\epsilon$ for different modes and the temperature sensitivity of 75 pm/°C for the core mode in a temperature range 298 K to 348 K. In [147], measurement of multiple physical parameters like temperature and strain with a single FBG based sensing technology has been reported. A new combined FBG based sensor designed to measure the temperature, strain, and the vibration is analysed and simulated using the FEM [148]. Such a sensor has given a strain sensitivity, linearity, and the measurement error in a fixed temperature environment as 5.44 pm/$\mu\epsilon$, 99.94%, and 2.05% F.S. in the range 0 to 580 $\mu\epsilon$, respectively. Similarly, the sensor's temperature sensitivity, linearity, and measurement error were recorded and shown as 16.12 pm/°C, 99.93%, and 2.15% F.S. respectively in the measurement range 273 K to 1373 K.

A sensing system developed can measure the temperature consistently up to 873 K and able to detect the cracks on the metal pipes shown in [149]. In [150], a hybrid FBG based sensor for simultaneous measurement of temperature and strain using double cladding fiber has been demonstrated. Such a sensor has given the maximum strain and temperature sensitivities as 0.76 pm/$\mu\epsilon$ and 13.2 pm/°C. However, a novel sawtooth stressor-assisted highly birefringent FBG or Hi-Bi FBG has been proposed for simultaneous strain and temperature measurement[151]. The proposed sawtooth stressor developed near the core of the fiber

using femtosecond laser direct inscription. Such a proposed stressor can produce the strain and high birefringence in the FBG and create a maximum birefringence of 2.96×10^{-4}. The strain sensitivity of the stressor-assisted Hi-Bi FBG found to be as 1.24 pm/$\mu\epsilon$ in λ_B and 2.14×10^{-2} pm/$\mu\epsilon$ in birefringence induced wavelength difference (λ_D) whereas temperature sensitivity as 9.52 pm/°C in λ_B and 0.13 pm/°C in λ_D. Also, the strain and temperature sensitivity in λ_D given by the sawtooth stressor were higher in the magnitude of several orders than a straight-stressor assisted Hi-Bi FBG emphasized. This kind of sawtooth stressor-assisted Hi-Bi FBG will find applications in innovative structures and intelligent robotics. In addition to the applications mentioned in this chapter, FBG technology can also be used for explosive detections, and the internet of things (IoT) applications [152, 153].

1.6 Cascaded fiber Bragg gratings for communication applications

In order to build a narrow-band filter or to enhance the optical transmission system performance, researchers are presently creating a variety of cascaded FBG structures with the aid of this technology. For filtering applications in optical communications, the desired characteristics of a cascaded FBG structure requires a narrow bandwidth with reduced number of sidelobes in the reflected signal spectrum is reported in [154]. Such a cascaded FBG structure has given reduced reflectivity stage by stage. However, the bit error rate (BER) performance of a SMF based transmission system is studied in depth, by positioning the cascaded FBGs immediately after the source and thereby after the modulator in [35]. It had been observed that the BER performance increases in both cases by reducing the spectral linewidth of the continuous wave (CW) laser source before the modulator and reducing the number of sidelobes after modulation [35]. Similar to this, [155] describes the performance of a wavelength division multiplexing (WDM) optical link using a cascaded Bragg grating design with different apodization functions. To compensate the dispersion effects in an optical network, a four stage tanh apodized FBG structure along with maximum time

division multiplexing technique had been implemented in [156]. In addition to the above mentioned cascaded FBG or Chirped FBG structures to reduce the dispersion in a WDM link, various cascaded FBG/CFBG structures along with the different modulation schemes are reported in [157, 158]. However, the performance of dense wavelength division multiplexing (DWDM) system improved with four same types of CFBGs is presented in [39]. Alternatively, to reduce the dispersion of a 10 Gbps WDM link with SSMF of length 70 km, a four stage cascading of apodized linearly chirped fiber Bragg gratings (CFBGs) of the identical type are considered in [159].

1.7 Motivation

Optical transmission systems are used in long-haul communication links, such as undersea cables and intercontinental connections. Enhancing the performance of optical transmission systems allows for longer transmission distances without significant signal degradation, enabling the expansion of global communication networks. Also, enhancing the performance of optical transmission systems allows for faster and more efficient data transfer, accommodating the increasing data demands of modern communication networks.In optical communication systems, when a range of wavelengths is emitted from the light source, it propagates along the optical fiber with different velocities and arrives at the receiver at different times, causing dispersion in the optical fiber. Dispersion is considered an important limiting factor for data transmission. Dispersion decreases the optical transmission system performance. Hence, the source spectral width of the pulse, which is proportional to the dispersion in the fiber, should be reduced for narrow-band filtering or communication purposes. Similarly, for better performance of an FBG-based device for sensing or communication purposes, the reflectivity should be greater than 50%, FWHM or narrow-bandwidth is less than 0.2 nm, and SLSR should be greater than 45 dB. Achieving all these values with single FBG based device or with the optimized single FBG may not be possible as the SLSR of the single FBG is less than 45 dB. Hence, to achieve all these values, researchers are creating a variety

of cascaded FBG-based devices.Similarly, to improve the optical transmission system performance, researchers are presently creating a variety of cascaded FBG structures with the aid of FBG technology. As cascaded FBG structures offer narrow bandwidth and a minimal number of side lobes in the reflected spectrum, designing a cascaded FBG-based device with better spectral characteristics will surely enhance the system's performance. Hence, there is always a demand to design the cascaded FBG-based device with better spectral characteristics. Narrow bandwidth or narrower full width at half maximum (FWHM) can improve the capturing capability of a filter to a specific wavelength, whereas the minimization of side lobes indicates the reduction of inter-channel crosstalk. So, in this work, we have initially aimed to design a cascaded FBG or chirped FBG structure which gives better spectral characteristics in terms of narrow bandwidth with a reduced number of side lobes. Once the structure has been designed, we need to use it in the optical communication system to enhance its performance. Particularly, the designed structure can be used immediately next to the optical source in the communication system to reduce source spectral width. As the source spectral width is proportional to the dispersion in the fiber, reducing it will reduce the fiber's dispersion and thus enhance the optical system performance.

1.8 Objectives of the Thesis

Cascaded FBG structures offer narrow bandwidth and minimal side lobes in the reflected spectrum. Design and analysis of cascaded FBG/CFBG-based devices with better spectral characteristics for communication and sensing purposes is the main objective of the thesis.

- To study and simulate the physical parameters like temperature and strain etc., and their effect on the optical properties of FBGs.
- To design and simulate the cascaded FBG/CFBG-assisted optical device with better spectral characteristics (narrow bandwidth with minimal number of side lobes) in the reflection spectrum for communication purposes.

- To study and simulate the effect of temperature on the designed cascaded FBG/CFBG assisted optical device for sensing purpose.
- Performance enhancement of long haul optical transmission system integrated with designed cascaded FBG structure or FBG assisted dispersion mitigation system.

1.9 Organization of the Thesis

The thesis is organized into six chapters. In addition to the current introduction, there are four main chapters and conclusions arrived at as follows.

Chapter 2 presents the spectral characteristics of a cascaded FBG structure of varying lengths operated on the C-band is simulated and analyzed for communication purposes. This chapter also deals with analyzing cascaded apodized FBG structure for better spectral characteristics. In this chapter, we have also presented the effect of temperature on the proposed device.Finally, it covers the comparative study reflecting the importance of cascaded FBG structure over the single optimized FBG in terms of different spectral characteristics. In the end, conclusions are drawn based on the proposed device characteristics.

Two designs for narrow-band spectral characteristics using cascaded CFBG and apodized CFBG based structures capable of operating on the C-band are proposed and analyzed in chapter 3 and chapter 4 respectively. Obtaining narrow-band spectral profiles from the designed cascaded CFBG based device using a piecewise uniform approach (PUA) is also incorporated. Simulation results corroborating the analytical formulation of the proposed designs are also included in both chapters. Further, the effect of temperature on the narrow-band spectral profiles is also discussed in both chapters. Finally, conclusions are drawn at the end of both chapters.

Chapter 5 discusses the system-level integration of designed cascaded FBG based device

and its effect on the system's performance. Among all the optical devices proposed in chapters 2,3 and 4, the optical device introduced in chapter 2 has given a narrow FWHM. Hence, we have used such a device to enhance the performance of the optical communication system in chapter 5. In particular, such a device has been kept immediately next to the optical source to reduce the source spectral width is discussed in this chapter. Accordingly, the dispersion in the fiber will be reduced and thus enhances the system performance, as presented in chapter 5. Simulation results reveal that the system formed with the proposed device has given better performance for various operating distances than in the absence of a device incorporated. The system's performance has also been tested with four level non-return to zero (NRZ) modulation format. Finally, conclusions drawn based on simulations are presented at the end of the chapter. Chapter 6 concludes with asummary of the total contributions to this thesis. It also gives future research possibilities.

Chapter 2

Spectral Characteristics of Cascaded Uniform and Apodized FBGs of Varying Lengths

2.1 Introduction

The spectral characteristics of cascaded FBGs are usually expressed in reflectivity, bandwidth, or Full Width at Half Maximum (FWHM) and the side lobes. The desired spectral properties of the cascaded arrangement of FBGs usually need a narrow bandwidth and minimal number of side-lobes with maximum peak reflectivity in the reflected spectrum for communication and sensing purposes. Often, as the number of cascaded FBGs of the same lengths increases, reflectivity decreases with reduced FWHM and number of side lobes [35, 154, 155]. In order to improve the reflectivity and narrower FWHM, a cascaded FBG structure has been proposed in this chapter. Such a proposed structure utilizes cascaded

uniform or apodized FBGs of varying lengths works in the C-band are analyzed and simulated. The proposed structure maintains almost constant reflectivity even for more number of stages. Further enhancement of FWHM at the expense of reflectivity can also be attained with the apodized FBGs in the proposed structure. Section 2.2 describes the analytical formulation of the single uniform FBG and the proposed cascaded FBG structures (formed with uniform and apodized FBGs) using CMT and TMM. However, a proposed experimental setup for a practical perspective is incorporated in section 2.3. Simulation results corroborating the analytical formulation of the proposed structure are included in Section 2.4. The effect of temperature on the proposed structure and a comparison of a single FBG with the cascaded FBGs with different parameters is also demonstrated in section 2.4. Finally, we have concluded the chapter in Section 2.5.

2.2 Analytical Formulation

2.2.1 Single Uniform FBG Structure

As depicted in Fig. 2.1, FBG can be assumed as a four port device with four fields. P_{01} and R_{M1} represents the input fields whereas Q_{01} and S_{M1} denotes the output fields. Here, we have assumed that the considered FBG is operated in reflective mode and is produced in single mode fiber (SMF). The incident and reflected fields in transfer matrix form can be expressed as [25, 44, 104, 160],

$$\begin{bmatrix} P_{01} \\ Q_{01} \end{bmatrix} = \begin{bmatrix} \cosh(\gamma L) - i\frac{\hat{\sigma}}{\gamma}\gamma^{-1}\sinh(\gamma L) & -i\kappa\gamma^{-1}\sinh(\gamma L) \\ i\kappa\gamma^{-1}\sinh(\gamma L) & \cosh(\gamma L) + i\frac{\hat{\sigma}}{\gamma}\gamma^{-1}\sinh(\gamma L) \end{bmatrix} \begin{bmatrix} R_{M1} \\ S_{M1} \end{bmatrix} \tag{2.1}$$

where $\gamma = \sqrt{\kappa^2 - \hat{\sigma}^2}$, κ denotes 'ac' coupling coefficient between the waves travelling forward and backward,$\hat{\sigma}$ is the 'dc' self-coupling coefficient and L denotes the length of an

uniform FBG. For simplicity eqn. (2.1) is designated as,

$$\begin{bmatrix} P_{01} \\ Q_{01} \end{bmatrix} = \begin{bmatrix} T_{11} & T_{12} \\ T_{21} & T_{22} \end{bmatrix} \begin{bmatrix} R_{M1} \\ S_{M1} \end{bmatrix} \tag{2.2}$$

For a reflective grating, the input field amplitude P_{01} is normalized to unity whereas the

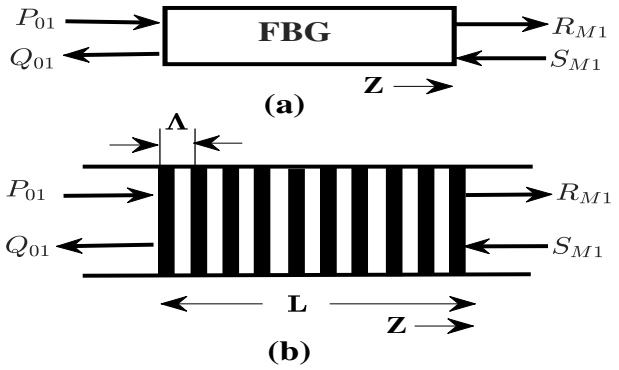

Figure 2.1: Schematic of single uniform FBG structure: (a) Block diagram representation, (b) RI variation inside the fiber core along the grating length.

amplitude of the reflected field S_{M1} at the output of the grating is considered zero. The reason for taking S_{M1} as zero is due to no perturbation further from the end of the grating. Hence, eqn. (2.2) can be rewritten as,

$$\begin{bmatrix} 1 \\ Q_{01} \end{bmatrix} = \begin{bmatrix} T_{11} & T_{12} \\ T_{21} & T_{22} \end{bmatrix} \begin{bmatrix} R_{M1} \\ 0 \end{bmatrix} \tag{2.3}$$

The transmitted field amplitude from the FBG can be estimated as $R_{M1} = 1/T_{11}$ and the reflected field amplitude obtained using eqn. (2.3) and the R_{M1} as $Q_{01} = T_{21}/T_{11}$.The reflectivity of a uniform FBG structure shown in Fig. 2.1 can be represented as [41, 44, 161],

$$r(L,\lambda) = \left|\frac{Q_{01}(\lambda)}{P_{01}(\lambda)}\right|^2 = \left|\frac{T_{21}}{T_{11}}\right|^2 = \frac{\sinh^2(\sqrt{\kappa^2 - \hat{\sigma}^2}L)}{\cosh^2(\sqrt{\kappa^2 - \hat{\sigma}^2}L) - \frac{\hat{\sigma}^2}{\kappa^2}} \tag{2.4}$$

where $r(L,\lambda)$ is the reflectivity. The value of $\hat{\sigma}$ expressed in terms of 'dc' coupling coeffi-

cient σ and the detuning wave vector as [44, 160],

$$\hat{\sigma} = \sigma + 2\pi n_{eff}\left(\frac{1}{\lambda} - \frac{1}{\lambda_B}\right) - \frac{1}{2}\frac{\mathrm{d}\phi}{\mathrm{d}z} \tag{2.5}$$

where λ is the operating wavelength. The value of σ can be made equal to $\frac{2\pi}{\lambda} \times \Delta n$. Where Δn represents the maximum RI perturbation of a uniform FBG.The resonance peak obtained at a wavelength called Bragg wavelength (λ_B) due to the RI variation inside the fiber core along the z direction of a FBG can be determined as$\lambda_B = 2n_{eff}\Lambda$. Where n_{eff} is the effective RI of the fiber core and Λ is the grating pitch. The derivative term in eqn. (2.5) determines the chirp of the grating pitch and can be considered as zero for a uniform FBG. The reflected peak from an FBG has a bandwidth or full width at half maximum (FWHM) is given by [101],

$$\text{FWHM} = \lambda_B m\sqrt{\left(\frac{\Delta n}{2n_{eff}}\right)^2 + \left(\frac{1}{M}\right)^2} \tag{2.6}$$

where M denotes the number of periods, and m is equals to 0.5 for weak grating whereas a strong grating structure allows a value of one.

2.2.2 Proposed Cascaded Uniform FBG Structure of Varying Lengths

Refer to Fig. 2.2, which depicts a four stage cascaded uniform FBG structure of different lengths with P_{0j} and R_{Mj} as the input signal field amplitudes while Q_{0j} and S_{Mj} denotes the output or reflected signal field amplitudes of a respective grating. Where j represents the stage number taken in the range 1 to 4 as the number of the stages considered is four. Cascading of FBGs have been performed by connecting the reflected signal output of the j^{th} stage FBG (available at Q_{0j}) utilized as input to the $(j+1)^{th}$ stage FBG (available at $P_{0(j+1)}$) results a condition $P_{0(j+1)}$= Q_{0j}. The reflected optical signal obtained at Q_{04} is the intended optical signal.In the proposed structure, the length of each FBG has been varied

linearly and considered as $a = (L + (j-1))$ mm. The spectral response of each FBG in the structure can be obtained using CMT and TMM as discussed in section 2. Hence, the reflectivity offered by each FBG in a four stage cascaded FBG structure is given by,

$$r(a,\lambda) = \left|\frac{Q_{0j}(\lambda)}{P_{0j}(\lambda)}\right|^2 = \frac{\sinh^2(\sqrt{\kappa^2 - \hat{\sigma}^2}a)}{\cosh^2(\sqrt{\kappa^2 - \hat{\sigma}^2}a) - \frac{\hat{\sigma}^2}{\kappa^2}} \tag{2.7}$$

The reflectivity of a four stage cascaded FBG arrangement can be expressed as [155, 162],

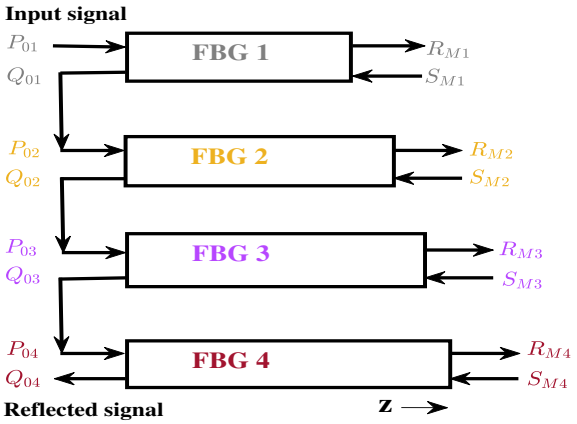

Figure 2.2: Schematic of four stage cascaded FBG structure of different lengths.

$$R_{cascaded\ 4}(\lambda) = \left|\frac{Q_{04}(\lambda)}{P_{01}(\lambda)}\right|^2 \tag{2.8}$$

Since FBG 4 receives the reflected optical signal from FBG 3, then eqn. (2.8) can be described as,

$$R_{cascaded\ 4}(\lambda) = \left|\frac{Q_{04}(\lambda)}{P_{04}(\lambda)} \times \frac{Q_{03}(\lambda)}{P_{01}(\lambda)}\right|^2 \tag{2.9}$$

Similarly, when FBG 3 receives the reflected optical signal from FBG 2 then eqn. (2.9) can be estimated as,

$$R_{cascaded\ 4}(\lambda) = \left|\frac{Q_{04}(\lambda)}{P_{04}(\lambda)} \times \frac{Q_{03}(\lambda)}{P_{03}(\lambda)} \times \frac{Q_{02}(\lambda)}{P_{01}(\lambda)}\right|^2 \tag{2.10}$$

Since FBG 2 receives the reflected optical signal from FBG 1 then the above equation is expressed as,

$$R_{cascaded\ 4}(\lambda) = \left| \frac{Q_{04}(\lambda)}{P_{04}(\lambda)} \times \frac{Q_{03}(\lambda)}{P_{03}(\lambda)} \times \frac{Q_{02}(\lambda)}{P_{02}(\lambda)} \times \frac{Q_{01}(\lambda)}{P_{01}(\lambda)} \right|^2 \tag{2.11}$$

Rearranging the above equation (i.e., eqn. (2.11)) results as,

$$R_{cascaded\ 4}(\lambda) = \left| \frac{Q_{04}(\lambda)}{P_{04}(\lambda)} \right|^2 \times \left| \frac{Q_{03}(\lambda)}{P_{03}(\lambda)} \right|^2 \times \left| \frac{Q_{02}(\lambda)}{P_{02}(\lambda)} \right|^2 \times \left| \frac{Q_{01}(\lambda)}{P_{01}(\lambda)} \right|^2 \tag{2.12}$$

eqn. (2.12) represents the reflectivity of the proposed cascaded structure. To get the spectral attributes of each FBG and the proposed structure we have employed eqn. (2.7) and eqn. (2.12), respectively to write the in-house developed code in MATLAB® R2021a. In order to get the reflectivity of the proposed structure or to implement eqn. (2.12) one can consider the following the sequence of steps,

1. Initially, the reflectivity of first FBG needs to be obtained using the eqn. (2.7) by defining the grating parameters such as Λ, L, and κ.
2. Next, follow the above step for calculating the reflectivity of the second FBG by varying the L value.
3. Later, multiply both the reflectivity obtained in step 1 and step 2.
4. Here, obtain the reflectivity of third FBG as mentioned in step-1.
5. Multiply the result obtained in step 3 with step 4
6. Finally, calculate the reflectivity of fourth FBG and multiply the same with the result obtained in step-5.

The obtained spectral profiles are designed at a λ_B of 1550.00 nm are shown in Fig. 2.3.It has been observed from Fig. 2.3 that as the number of cascaded FBGs increases then the FWHM of the reflected spectral profile decreases from 0.202 nm (shown in grey color) to 0.175 nm (represented in brown color). Hence, a narrow bandwidth with reduced strength

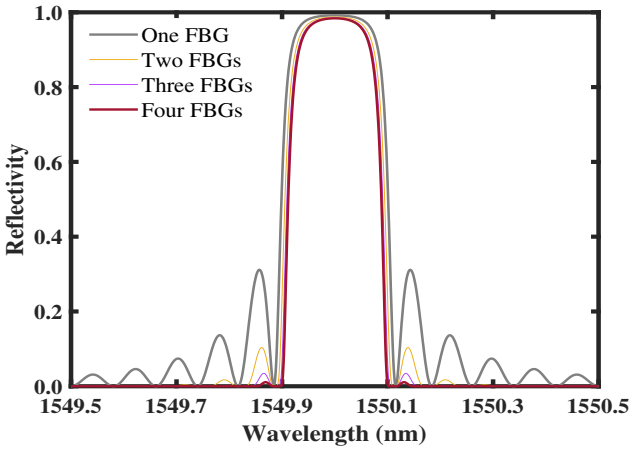

Figure 2.3: Spectral characteristics of cascaded FBG structure of varying lengths. Simulation parameters considered are: L=10 mm for first FBG, $\Delta n = 2 \times 10^{-4}$ and $\lambda_B = 1550.00$ nm.

of side lobes can be accomplished with the proposed structure. Similarly, the recorded reflectivity has come down to $98.39\ \%$ (mentioned in brown color) as the number of cascaded FBGs increases. The reason for the reduced reflectivity stage-by-stage is that the reflecting capability of eachFBG varies in the structure with its length at the designed wavelength, and the output of the one FBG is used as input to the subsequent FBG in the structure. To mitigate this effect one can change the induced refractive index of the grating which in turn effect the FWHM and SLSR of the reflected profile. Similarly, the reason for considering the four stages is that the side-lobe suppression ratio (SLSR) threshold value is achieved at the fourth stage. As per the literature, the SLSR must be greater than or equal to 45 dB for better performance of an FBG-based device. Also, the reflectivity and the FWHM are greater than 50% and less than or equal to 0.2 nm, respectively [163, 164]. Hence, in the fourth stage, we can achieve the required values. Further consideration of stages will give us no significant improvement in reflectivity and FWHM. Also, increases the complexity and cost of the system. The detailed values of spectral characteristics can be seen from Table-2.1.As per the above discussion, one can conclude that the proposed cascaded structure reduces the spectral width of the optical pulse launched. However, the extent of pulse broadening usually termed as 'dispersion' in the fixed fiber length L_f depends on the spectral width of the

Table 2.1: Spectral Characteristics of Cascaded FBGs at λ_B of 1550.00 nm

Number of FBGs cascaded	**Reflectivity (%)**	**FWHM (nm)**	**SLSR (dB)**
One	99.19	0.202	11.578
Two	98.75	0.188	22.694
Three	98.52	0.178	33.570
Four	98.39	0.175	45.767

pulse launched [165]. Hence, it is important to consider the effect of source spectral width on the system performance. As different spectral components of the pulse will receive the other end of the fiber at different time instants, the optical pulse launched gets broadened resulting in inter-symbol interference (ISI), thus reducing the performance of the system. Therefore, placing the proposed structure in the optical communication system reduces the source spectral width and thus improves system performance.

2.2.3 Cascaded Apodized FBG Structure of Varying Lengths

As per the discussion we had in the preceding section, one can note that the FWHM is reduced stage by stage with the cascaded FBG structures. Further enhancement of FWHM can be achieved by considering the apodized FBGs in the structure. The spectral response of a single apodized FBG can be obtained using coupled-mode theory (CMT) solved based on the transfer matrix method (TMM). A cascaded FBG structure formed with apodized FBGs is shown in Fig.2.4. However, apodization refers to the the suppression of the side lobes in the reflection spectrum by gradually raising the coupling coefficient with penetration into the grating and gradually decreasing it when exiting the grating. Generally, apodization is used to improve the grating response. Clearly, one can say that in an apodized FBG, the amplitude of the r.i perturbation inside the core can't be a constant uniform variation rather it is non-uniform in nature [25, 44, 166]. So, the κ changes with z in an apodized FBG. The coupling coefficient of an FBG can be estimated as [5] [101],

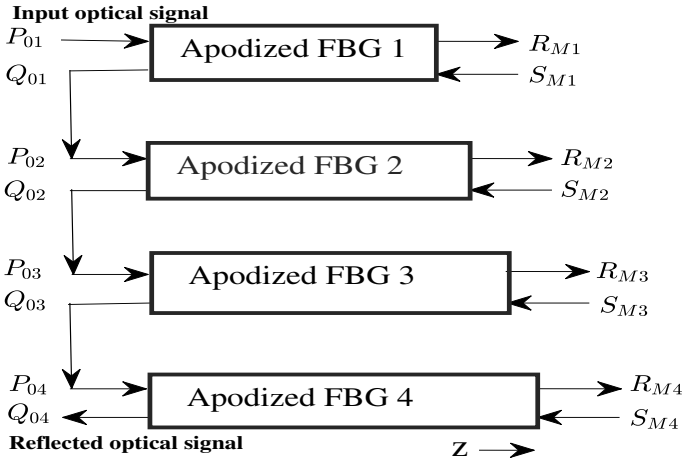

Figure 2.4: A four stage cascaded arrangement of apodized FBGs.

$$\kappa(z) = \frac{\pi}{\lambda}\,\Delta n\,(1 - V^{-2})\,G(z) \tag{2.13}$$

where $G(z)$ is the apodization function. For a uniform FBG, the value of $G(z)$ can be considered as 1. If we consider Gaussian apodization function to improve the grating response, the value of κ can be written as,

$$\kappa(z) = \frac{\pi}{\lambda}\,\Delta n\,(1 - V^{-2})\,\exp\left[-\alpha\left(\frac{z - L/2}{L}\right)^2\right] \tag{2.14}$$

where α is a Gauss width parameter. However, owing to advantages such as non-abrupt declining slopes toward the margins or edges, a broad flat region around the center wavelength, and a lower side-band reflectivity, the hyperbolic tangent profile usually will give a better grating response [167]. Hence, if we consider such a function then the $G(z)$ can be approximated as [25],

$$G(z) = 0.5 \times \left[1 + Tanh\left(\beta \times \left(1 - 2\left|\frac{2z}{L}\right|^{\alpha}\right)\right)\right] \tag{2.15}$$

where α and β are the width parameters of Tanh profile. Hence, the κ varies with z can be written by using eqn. (2.13) as,

$$\kappa(z) = \frac{\pi}{2\lambda}\Delta n(1 - V^{-2}) \left[1 + Tanh\left(\beta\left(1 - 2\left|\frac{2z}{L}\right|^{\alpha}\right)\right)\right] \tag{2.16}$$

The reflectivity of the proposed cascaded apodized FBG structure can be obtained by using eqn. (2.12). But, the value of κ in eqn. (2.7) can be considered by utilizing eqn. (2.14) and eqn. (2.16) for Gaussian and Hyperbolic tangent apodization respectively.

2.3 Proposed Experimental Setup

For a practical perspective, one can employ the experimental setup depicted in Fig. 2.5. As illustrated, the four FBGs are to be connected using four broadband optical circulators. The input optical signal generated from a C-band amplified spontaneous emission (ASE) source is given to terminal 1 of circulator 1. The output from circulator 1 (refer to port 2) will excite FBG 1. Since the FBG will reflect only narrow-band of light, one cannot collect the entire band of the input light at terminal 3 of circulator 1. That means most of the light will pass through FBG 1. However, the reflected signal (port 3 of circulator 1) will retain its spectral purity assuming very strong spectral isolation among the ports of the circulator. To visualize the transmitted spectrum of the FBG, an optical spectrum analyzer (OSA) can be connected to the output terminal of FBG 1. The reflected signal from FBG 1 is then transmitted to FBG 2 through circulator 2. The final reflected signal will be received at terminal 3 of circulator 4 as a result of an operation similar to that earlier mentioned. Also, optical amplifiers can be used to compensate for the circulator insertion losses while using the proposed device in the optical system.

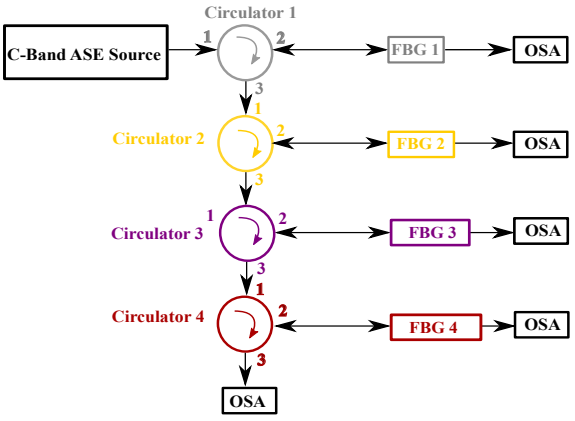

Figure 2.5: Experimental setup for four stage cascaded FBG structure of varying lengths

2.4 Simulation Results and Discussion

It is evident from Fig. 2.6 that as the number of cascaded apodized FBGs of varying lengths increases, an enhanced narrow-band with the reduced number of side-lobes has been achieved. The behavior of the proposed device at each stage is observed with the help of MATLAB® R2021a software. A broadband light operated on C-band (1530 to 1565 nm) as an input optical signal encounters at the first apodized FBG in Fig. 2.4, and the reflected signal can be taken from FBG 4. For simulations, we have considered each apodized FBG built on SMF-28 and chosen the first FBG of length 10 mm, and the rest chosen according to the relation mentioned in section-2.2.2. For $\alpha = 1$, the reflectivity and FWHM of a single apodized FBG (Shown in red color of Fig. 2.6 (a)) are recorded as 96.85 $\%$ and 0.16 nm, respectively. As the number of stages increases, we can accomplish a narrow band of 0.13 nm with a 93.08 $\%$ reflectivity (Shown in pink color of Fig. 2.6 (a)). By changing the α from 1 to 4, we can achieve an FWHM of 0.06 with reduced strength in the side lobes. The detailed values of reflectivity and FWHM of a cascaded FBG structure with Gaussian apodization furnished in Table-2.2.

On the other hand, one can use the FBGs apodized with hyperbolic tangent function in Fig. 2.4. It has been observed from the simulated results depicted in Fig. 2.7 that

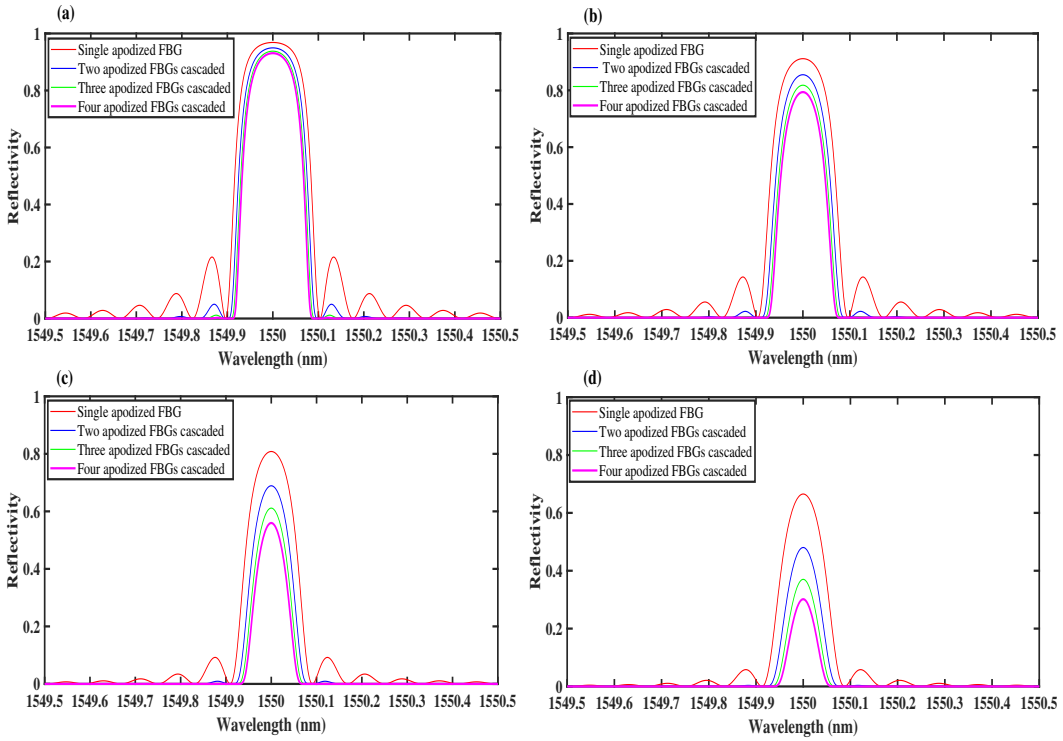

Figure 2.6: Simulated reflected spectral profile of a proposed structure: (a) $\alpha = 1$ (b) $\alpha = 2$ (c) $\alpha = 3$ (d) $\alpha = 4$.

Table 2.2: Spectral characteristics of cascaded FBGs with Gaussian apodization

Number of FBGs Cascaded	$\alpha = 1$		$\alpha = 2$		$\alpha = 3$		$\alpha = 4$	
	R (%)	**FWHM (nm)**	**R (%)**	**FWHM (nm)**	**R (%)**	**FWHM (nm)**	**R (%)**	**FWHM (nm)**
Single FBG	96.85	0.16	91.13	0.14	80.82	0.12	66.52	0.10
Two FBGs	94.95	0.15	85.48	0.12	68.89	0.10	48.03	0.08
Three FBGs	93.79	0.14	81.79	0.11	61.13	0.09	37.02	0.07
Four FBGs	**93.08**	**0.13**	**79.37**	**0.10**	**55.95**	**0.08**	**30.15**	**0.06**

the introduced cascaded arrangement given narrow-band spectral attributes with reduced number of side-lobes. Also, it is evident from the Fig. 2.7 that the proposed device has given us improved spectral attributes (in terms of FWHM and number of side-lobes) as the number of stages escalates from one to four. However, the spectrum in red is designated for a single apodized FBG, while the pink color is used for cascading four apodized FBGs. Similarly, the spectrum in blue is used for the cascading of two FBGs whereas the green color is for cascading of three FBGs. Here, we haveobserved the spectral characteristics of the proposed

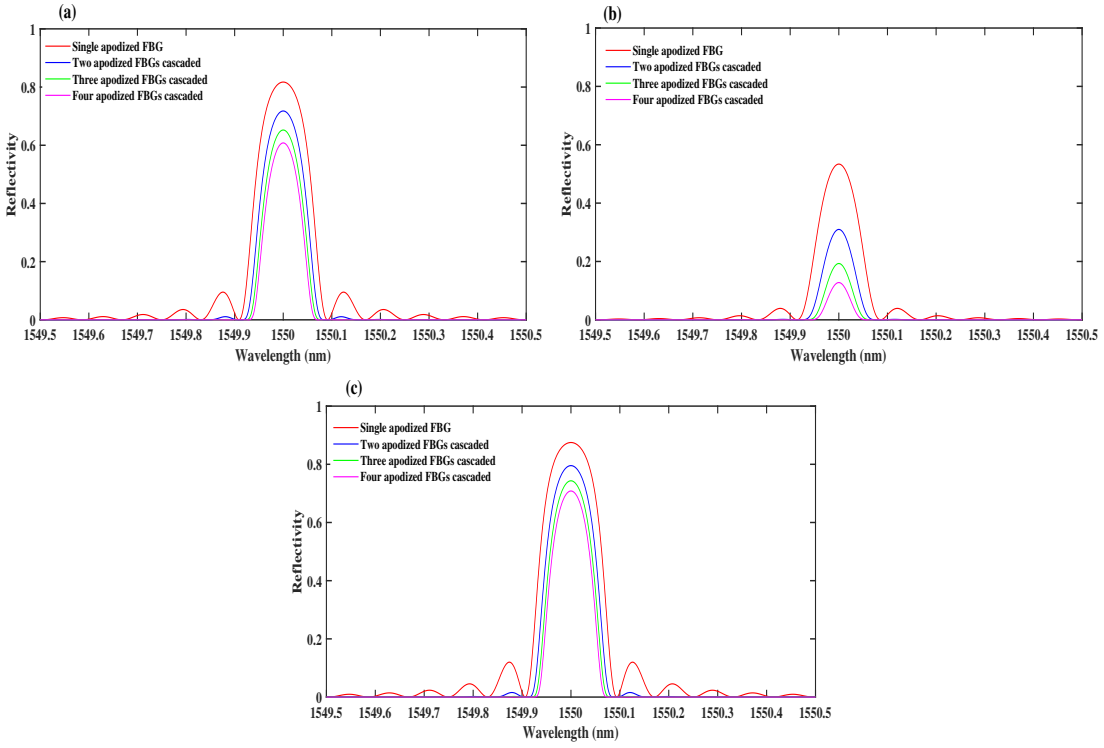

Figure 2.7: Spectral attributes of a four stage cascaded apodized FBGs with hyperbolic tangent function for the case: (a) $\alpha = \beta$ with α and β are considered as 0.1. (b) $\alpha < \beta$ with α and β are taken as 0.1 and 1.2, respectively (c) $\alpha > \beta$ with α and β are considered as 1.2 and 0.1, respectively

cascaded arrangement for three different cases. Initially using the relation $\alpha = \beta$ followed by $\alpha < \beta$ and $\alpha > \beta$. The values of α and β are considered for the simulation are 0.1 and 1.2, respectively. For $\alpha = \beta$, the reflectivity of the proposed cascaded structure changes from 81.72% to 59.81% while the FWHM changes from 0.12 nm to 0.07 nm as the cascaded FBGs changes from one to four. The same can be verified by looking at Fig. 2.7(a). In Fig. 2.7 (b), one can observe the reflected profiles for the case $\alpha < \beta$. In this case, the reflectivity is changes from 53.37% to 12.77% and the FWHM changes from 0.10 nm to 0.05 nm as the cascaded FBGs escalates from one to four. Hence, the maximum reflectivity and minimum FWHM are noted as 53.37% and 0.05 nm, respectively. Also, it is shown from Fig. 2.7(c) that the reflectivity changes from 87.49% to 70.82% whereas the FWHM alters from 0.14 nm to 0.09 nm. Therefore, one can achieve a maximum reflectivity of 87.49% and minimum

FWHM of 0.09 nm using the case $\alpha > \beta$. The detailed values of reflectivity and FWHM of a cascaded FBG structure with Hyperbolic tangent apodization are furnished in Table-2.3. It is concluded from the above discussion that depending on the profile parameter of the chosen apodization function, one can vary the spectral characteristics of the proposed device and hence will affect the performance of the optical transmission system. Since the dispersion in the fiber is proportional to the spectral width of the pulse launched, varying the spectral width using a cascaded apodized structure will affect the system's performance

Table 2.3: Spectral attributes of four stage cascaded apodized FBGs with hyperbolic tangent function

Number of FBGs Cascaded	$\alpha = 0.1, \beta = 0.1$		$\alpha = 0.1, \beta = 1.2$		$\alpha = 1.2, \beta = 0.1$	
	R (%)	**FWHM (nm)**	**R (%)**	**FWHM (nm)**	**R (%)**	**FWHM (nm)**
Single FBG	81.72	0.12	53.37	0.10	87.49	0.14
Two FBGs	70.31	0.10	30.98	0.08	79.54	0.12
Three FBGs	62.85	0.08	19.30	0.06	74.33	0.10
Four FBGs	**59.81**	**0.07**	**12.77**	**0.05**	**70.82**	**0.09**

2.4.1 Effect of Temperature on the Proposed Structure

Usually, the performance of FBGs are sensitive to temperature variations. Hence, the study of temperature effect on the proposed structure containing uniform FBGs will help the designer for any athermal variations. A small change in the temperature will results in the change of the peak wavelength. The same has been described in a mathematical manner in the preceding chapter. Here, initially, we have assumed that the proposed structure was kept in a place where the temperature is maintained at $100^{\circ}C$. Since the FBGs in the proposed structure are at $100^{\circ}C$, then one can observe a Bragg wavelength shift of 1.37 nm from a reference value (in this case 1550.0 nm) and the same can be confirmed from Fig. 2.8. That means for every $1^{\circ}C$ rise in temperature will results a Bragg wavelength shift of 13.6 pm. The dependence of λ_B on ΔT can be described by using the relation as mentioned in eqn. (1.14) or eqn. (1.16). In Fig. 2.8, the solid color lines indicate the proposed structure

at reference temperature (ΔT=0°C) while the dotted line designates the shift in the Bragg wavelength for ΔT of 100°C.It is evident from Fig. 2.8 that as the temperature changes

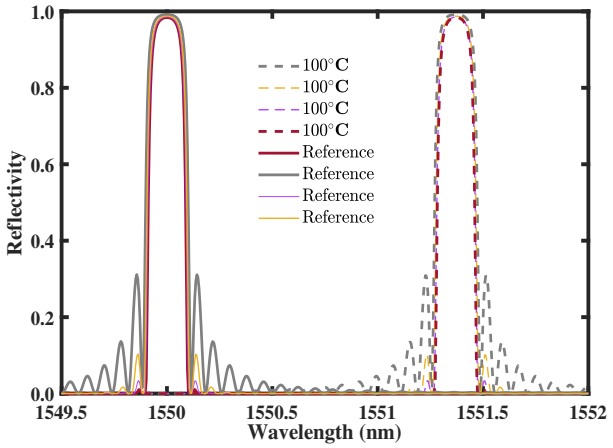

Figure 2.8: Effect of temperature in the Bragg wavelength of the proposed structure containing uniform FBGs at 100°C

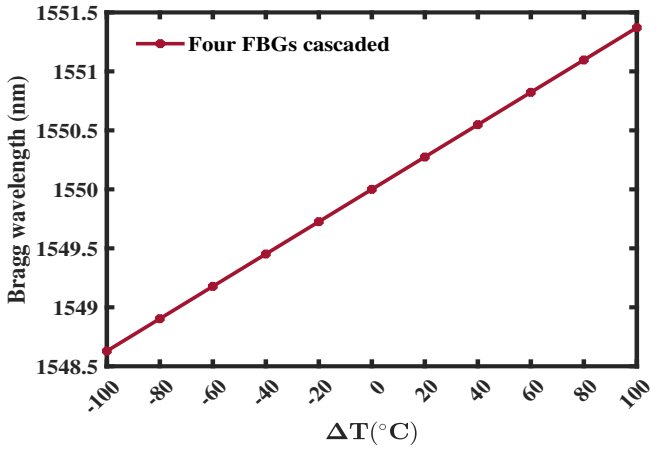

Figure 2.9: Estimated values of λ_B w.r.t ΔT for -100°C to +100°C

by 100°C from a reference value (ΔT=0°C), then the spectrum is shifted to 1551.36 nm from 1550.00 nm . The shift of λ_B for the corresponding change of ΔT in step of 20°C can be obtained from Fig. 2.9. Similarly, the variation of λ_B from 1550 nm to 1548.64 nm for a change of ΔT from 0°C to -100°C can be seen from Fig. 2.9. However, the Bragg wavelength shift towards left from 1550 nm in steps of 0.27 nm variation for every 20°C

change in temperature can be seen from the same figure. Clearly, one can confirm that for positive temperature variation, the λ_B shifts towards the right while it shifts to the left from 1550 nm for negative temperatures. This investigation of temperature on the proposed structure reveals a linear dependence of λ_B on ΔT when temperature changes from -100$^\circ C$ to +100$^\circ C$.

2.4.2 Comparative study

Here, the performance comparison of a single FBG with the cascaded FBG structure of four stages is presented and the same can be found from Table-2.4. For the simulation we have used the L=10 mm for first FBG, $\Delta n = 2 \times 10^{-4}$ and $\lambda_B = 1550.00$ nm. It has been observed from Table-2.4 that an FWHM of 0.11 nm can be attained with the optimized single FBG (or FBG apodized with Hyperbolic Tangent function [25]). But with the use of cascaded FBG structure, the value can be narrow down to 0.07 nm.Similarly, the

Table 2.4: Performance comparison of a single FBG with the cascaded FBGs of varying lengths

Spectral characteristics	Single uniform FBG	Cascaded uniform FBGs (At fourth stage)	Single apodized FBG		Cascaded apodized FBGs	
			Gaussian apodization	Hyperbolic tangent	Gaussian apodization	Hyperbolic tangent
Reflectivity (%)	99.19	98.39	80.82	81.72	55.95	59.81
FWHM (nm)	0.20	0.17	0.12	0.11	0.08	0.07
SLSR (dB)	11.57	45.76	21.71	22.67	87.38	89.41
Roll-off rate (dB/nm)	4.14	9.64	13.87	23.75	41.54	42.01

corresponding side-lobe suppression ratio or SLSR can be attained to 22.67 dB for single FBG whereas with cascaded structure, the value can be enhanced to 89.41 dB. It is also deduced from the Table-2.4 that compared to the uniform FBG, apodized FBG has given as better spectral characteristics in terms of FWHM and SLSR. On the other hand, compared with the apodized FBG, cascaded apodized FBG structure has given us good performance. Similarly, the corresponding reflectivity of each apodized FBG with the cascaded apodized FBGs of varying lengths are demonstrated. Here, the reflectivity of cascaded apodized

FBGs are lesser in value than compared to the single apodized FBG or single uniform FBG. In particular, the value of reflectivity for a cascaded apodized FBG structure (in which FBGs apodized with Hyperbolic Tangent function) is recorded as 59.81$\%$ while it was recorded as 81.72$\%$ and 99.19$\%$ for the single apodized and single uniform FBG respectively. Although the reflectivity value is still lower, one can consider it as it is greater than the threshold value.One can also deduce from the Table-2.4 that the cascaded FBG structure formed with hyperbolic tangent apodized FBGs has given higher roll-off rate than the other structure(s). The highest value recorded for this structure is 42.01 dB/nm. It means, for every nanometre shift in wavelength away from the peak reflection wavelength, the reflectivity decreases by 42.01 dB. However, the reason for using cascaded FBG structure over the optimized single FBG is to get the narrow-bandwidth and maximum SLSR.

2.5 Conclusion

In this chapter, a cascaded FBG structure of varying lengths operated on the C-band is proposed. A suitable analytical formulation for such a structure based on TMM is incorporated. It is evident from the simulation results that the proposed device can attain a maximum reflectivity of 98.39 $\%$ corresponding to the FWHM of 0.175 nm. However, to improve the FWHM of the proposed device, we have used apodized FBGs in the structure. It is emphasized from the simulation results that the proposed device can attain an FWHM of 0.08 nm corresponding to a reflectivity of 55.95$\%$ with the Gaussian apodization with a width parameter of 3. Further improvement in FWHM or a narrow bandwidth of 0.07 nm corresponding to a reflectivity 59.81 $\%$ (for the case $\alpha = \beta$) can be achieved with the Hyperbolic tangent apodized FBGs in the structure. The detailed spectral characteristics at each stage of the constructed device have been incorporated for both uniform and apodized FBGs. Also, the effect of temperature on the spectral characteristics of the proposed structure is studied. Simulation results reveal that λ_B of the proposed cascaded structure has a linear dependence

on ΔT. Finally, the performance comparison of a single FBG with the single apodized FBG and the cascaded apodized FBGs of varying lengths are studied.

Chapter 3

Narrow-band Optical Band-pass Filter using Dual Cascaded Chirped FBGs

3.1 Introduction

The chirped fiber Bragg gratings (CFBGs) can be mathematically modelled using a number of uniform FBGs with varying refractive index (RI) perturbation and/or the period of the RI perturbation along the grating length [168, 169, 170]. As CFBGs offer reduced side-lobes in the reflected spectrum, they are now widely used in distributed sensing of temperature, thermal hotspots, strain discontinuities [50, 171, 172] and communication related applications [44]. Other applications of CFBGs include dispersion compensation [39, 173, 174, 175] , pulse shaping [175, 176, 177], microwave photonics [178], optical frequency domain reflectometry [179], and optical backscattering reflectometry [180]. Owing to advantages such as narrow bandwidth and reduced strength of sidelobes in the reflection spectrum, the cascaded FBG or CFBG structures for communication purposes are currently being in use [39, 154, 158, 159]. This chapter proposes and analyzes cascaded chirped fiber Bragg grating or CFBG-based narrow-band bandpass filter capable of operating in C-band. Here, we

have cascaded two CFBGs in such a way that the reflected output of the linearly increased chirp (LIC) FBG is given as input to the linearly decreased chirp (LDC) FBG. The resultant reflected output from the LDC FBG is the intended spectral profile of narrower FWHM. The chirp rate of the two CFBGs may be the same or different. Section 3.2 describes the analytical formulation based on a piecewise uniform approach (PUA) for the proposed structure(s). Simulation results corroborating the analytical formulation of three different cascaded CFBG structures are included in Section 3.3. Also, the temperature's effect on the proposed devices' spectral profile is discussed here. At last, we conclude the chapter in Section 3.4.

3.2 Analytical Formulation

3.2.1 Piecewise Uniform Approach (PUA) for CFBG

As the RI of the CFBG varies with its length L along the mode propagation direction z, we can divide the grating region into N-uniform FBG sections of length L_g shown in Fig. 3.1(a). The position of the j-th section can be calculated as $z_j = (j-1)L/N$ where $j = 1, \cdots N$. The accuracy of the piecewise uniform approach (PUA) is a strong function of N. In PUA, it is assumed that each section will reflect one Bragg wavelength $\lambda_{B,N}(z)$ related to its period $\Lambda_N(z)$ which can be estimated as [25, 44, 101, 176, 181],

$$\lambda_{B,N}(z) = \left(2n_0(z) + \Delta n_{max}\left[1 + G(z)cos\left(\tfrac{2\pi}{\Lambda_1}z + \phi(z)\right)\right]\right)\Lambda_N(z) \qquad (3.1)$$

where $n_0(z)$ denotes the average RI of the guided mode equals to $(n_{eff} + (\Delta n_{max}/2))$ in which n_{eff} is the effective refractive index and Δn_{max} represents the maximum RI perturbation amplitude. $G(z)$ is the apodization function, Λ_1 is the grating period of the first section in CFBG, and $\phi(z)$ describes the 'chirp' or additional phase variation in the

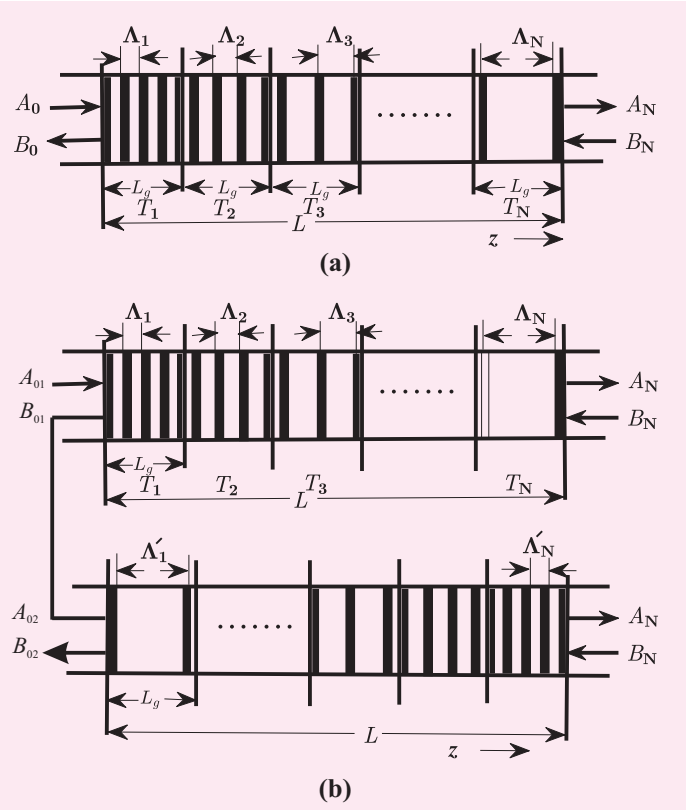

Figure 3.1: Schematic for (a) piecewise uniform approach (PUA) of CFBG, (b) cascaded CFBGs for narrow-band filtering applications.

CFBG region. In the CFBG, the grating period and linear chirp parameter x are related as $\Lambda_N(z) = \Lambda_1 + xz_N$, where x can be taken in terms of (nm/cm). The reflectivity from the j-th section of the CFBG can be estimated using [44],

$$r_j(\lambda) = \frac{\sinh^2(\sqrt{\kappa_j^2 - \hat{\sigma_j}^2} L_g)}{\cosh^2(\sqrt{\kappa_j^2 - \hat{\sigma_j}^2} L_g) - \frac{\hat{\sigma_j}^2}{\kappa_j^2}} \tag{3.2}$$

where λ is the operating wavelength, κ is the AC coupling coefficient. The DC self-coupling coefficient ($\hat{\sigma}$), detuning wave vector (δ), and DC coupling coefficient (σ) are related as [44],

$$\begin{aligned} \hat{\sigma} &\simeq \sigma + \delta - \frac{1}{2}\frac{\mathrm{d}\phi}{\mathrm{d}z} \\ &\simeq \sigma + 2\pi n_{eff}\left(\frac{1}{\lambda_D} - \frac{1}{\lambda}\right) - \frac{1}{2}\frac{\mathrm{d}\phi}{\mathrm{d}z} \end{aligned} \tag{3.3}$$

Note in eqn.(3.3), $\lambda_D = 2n_{eff}\Lambda$ is the design wavelength and the last derivative term is the chirp of the grating period. For CFBG eqn.(3.3) can be rewritten as,

$$\hat{\sigma} \simeq \sigma + 2\pi n_{eff}\left(\frac{1}{\lambda_D} - \frac{1}{\lambda}\right) + \frac{4\pi n_{eff} z}{\lambda_D^2}\,\frac{\mathrm{d}\lambda_D}{\mathrm{d}z} \tag{3.4}$$

For a single-mode Bragg reflection in a uniform FBG, σ and κ can found as [5, 44, 101],

$$\sigma = \frac{2\pi}{\lambda}\,\Delta n \tag{3.5}$$

$$\kappa = \frac{\pi}{\lambda}\,\Delta n\,(1 - V^{-2})\,G(z) \tag{3.6}$$

where Δn is the maximum RI perturbation along the length of the uniform grating. It ranges in between 10^{-5} to 10^{-2}. V is the dimension-less waveguide parameter. In this chapter, we have not considered any apodization profile of the gratings and hence $G(z) = 1$.Utilizing the PUA, the reflected spectrum of a single CFBG can be written as [50, 161],

$$R(\lambda) = 1 - \prod_{j=1}^{N}(1 - r_j(\lambda)) \tag{3.7}$$

and the corresponding full width at half maximum (FWHM) for an uniform FBG is [101],

$$\text{FWHM} = \lambda_B \alpha \sqrt{\left(\frac{\Delta n}{2n_{eff}}\right)^2 + \left(\frac{1}{M}\right)^2} \tag{3.8}$$

where M is the number of periods in a uniform FBG, and $\alpha = 0.5$ or 1 for weak-grating and strong grating structures, respectively.

3.2.2 PUA for Proposed Cascaded CFBG Structures

Refer to Fig. 3.1(a), which depicts a single CFBG with A_j and B_j are the amplitude of propagating mode and reflected mode, respectively for the j-th section. Cascading CFBGs can be done by connecting the reflected signal output of the first CFBG of type LIC (with

varying periods as $\Lambda_1 < \Lambda_2 .... < \Lambda_N$) to the input of the next CFBG of kind LDC (with varying periods as $\Lambda_1^{'} > \Lambda_2^{'} .... > \Lambda_N^{'}$) as shown in Fig. 3.1(b). Now the chirp parameter of both these CFBGs may be equal or different. All of the cases have been incorporated in this chapter. Cascading FBGs improve the spectrum rejection capability, and thus the same is expected when CFBGs are connected in cascade. In this chapter, we have proposed three different schemes, which are marked as III, IV, and V of Fig. 3.2

A good approximation to estimate the spectral characteristics of a FBG can be obtained using CMT and TMM [44, 101]. In Fig. 3.1, the length of a CFBG has been divided in to N piecewise uniform FBG sections with linearly varying periods. The propagation of a incident mode through each uniform section can be modelled by a 2×2 transfer matrix T_j as,

$$\begin{bmatrix} A_j \\ B_j \end{bmatrix} = T_j \begin{bmatrix} A_{j-1} \\ B_{j-1} \end{bmatrix} = \begin{bmatrix} T_{11} & T_{12} \\ T_{21} & T_{22} \end{bmatrix} \begin{bmatrix} A_{j-1} \\ B_{j-1} \end{bmatrix} \tag{3.9}$$

where the transfer matrix for j-th section are

$$T_j = \begin{bmatrix} \cosh(\gamma_j L_g) - i\hat{\sigma}\gamma_j^{-1}\sinh(\gamma_j L_g) & -i\kappa_j\gamma_j^{-1}\sinh(\gamma_j L_g) \\ i\kappa_j\gamma_j^{-1}\sinh(\gamma_j L_g) & \cosh(\gamma_j L_g) + i\hat{\sigma}\gamma_j^{-1}\sinh(\gamma_j L_g) \end{bmatrix} \tag{3.10}$$

where $\gamma_j = \sqrt{\kappa_j^2 - \hat{\sigma_j}^2}$. The reflected spectrum of a single CFBG can be given by [35, 50, 101],

$$R(\lambda) = \left|\frac{B_0(\lambda)}{A_0(\lambda)}\right|^2 = \left|\frac{T_{21}}{T_{11}}\right|^2 = 1 - \prod_{j=1}^{N}(1 - r_j(\lambda)) \tag{3.11}$$

The chirp of a CFBG can be either increasing or decreasing linearly. It is expected that the reflected signal spectrum of a single CFBG (for both LIC and LDC) will give broader bandwidth. To achieve a narrow band reflected spectrum, cascaded CFBGs can be utilized. Refer back to Fig. 3.1(b), which is similar to the structure III of Fig. 3.2. In this case, the

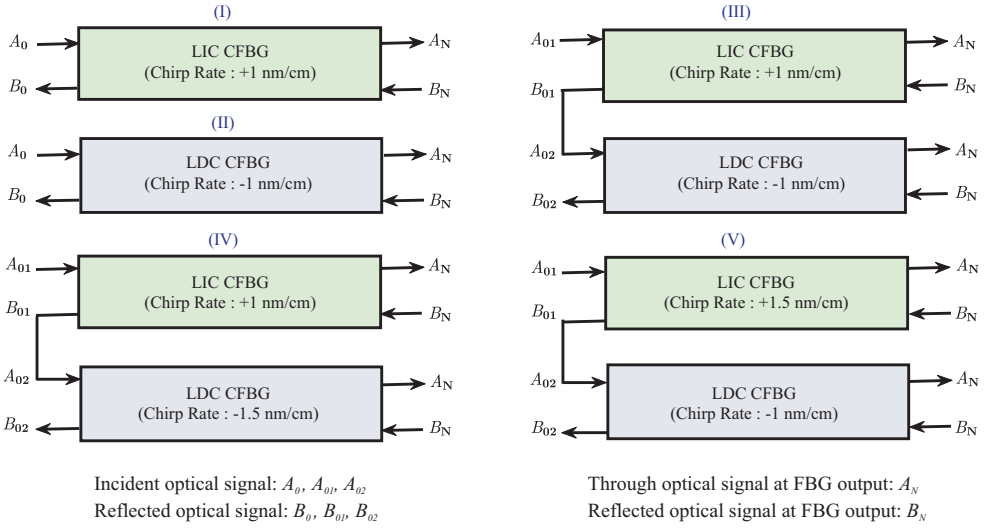

Figure 3.2: Block diagram representation of various CFBGs. Structure I and II indicates individual LIC and LDC CFBG. Structure III, IV and V indicates cascading scheme of LIC and LDC CFBGs with same and different chirp rates.

reflected optical signal B_{01} from a LIC CFBG is given as the input optical signal A_{02} to a LDC CFBG and thus gives a condition $B_{01} = A_{02}$. Similar kind of profile can be observed even chirp rate of the CFBGs are varied. The varying chirp rate cases are considered in the proposed structures IV and V. Mathematically, the reflected signal of the proposed cascaded CFBG structure can be written as,

$$R_{cascaded}(\lambda) = \left|\frac{B_{02}(\lambda)}{A_{01}(\lambda)}\right|^2 = \left|\frac{B_{01}(\lambda)}{A_{01}(\lambda)}\right|^2 \left|\frac{B_{02}(\lambda)}{A_{02}(\lambda)}\right|^2 \tag{3.12}$$

The above equation (i.e., eqn. (3.12)) can also be estimated as,

$$R_{cascaded}(\lambda) = \left[1 - \prod_{j=1}^{N}(1 - r_j(\lambda))\right]\left[1 - \prod_{k=1}^{N}(1 - r_k(\lambda))\right] \tag{3.13}$$

where r_j is the reflection from j^{th} section of LIC grating and r_k is the reflection from k^{th} section of LDC grating. Considering equal number of sections in both LIC and LDC CFBGs,

eqn. (3.13) can further be reshaped as,

$$R_{cascaded}(\lambda) = 1 - 2\prod_{m=1}^{N}(1 - r_m(\lambda)) + \prod_{m=1}^{N}(1 - r_m(\lambda))^2 \tag{3.14}$$

In the proposed structures we have incorporated the serial cascading of two CFBGs using circulator(s). However, one can utilize the same principle of dual cascading of two CFBGs in transmission mode too. In such case, the overall system will behave as a narrow-band optical band-stop or band-reject filter. The performance metrics of such band-reject filter will remain fairly same when compared to bandpass filter.

3.2.3 PUA Approach for Tilted Fiber Bragg Gratings

The PUA approach for titled fiber Bragg gratings becomes slightly different since we need to consider several other propagating modes as mentioned in [182, 183, 184]. For a weakly tilted FBGs, the light is coupled from fundamental LP_{01} mode to a backward propagating Bragg mode and also with backward propagating cladding modes. Thus it is imperative to employ coupled mode relation between the various core and cladding modes as mentioned below [182, 185].

$$\frac{\mathrm{dA}_{01}}{\mathrm{d}z} = if_{01-01}A_{01} + ig^{+}_{01-01}B_{01}e^{-2i\delta_{01-01}z} \tag{3.15}$$

$$\frac{\mathrm{dB}_{01}}{\mathrm{d}z} = -iB_{01-01}g^{-}_{01-01}e^{2i\delta_{01-01}z} - iB_{01}f_{01-01} \tag{3.16}$$

$$\delta_{01-01} = \frac{2\pi n_{eff}}{\lambda} - \frac{\pi}{\Lambda}\cos\theta \tag{3.17}$$

where A_{01}, B_{01} are the amplitudes of the forward and backward core modes propagating along z direction. The coupling coefficients f_{01-01} and $g^{\pm}_{01-01}$ for forward and backward propagation core modes are estimated using the following relations:

$$g^{\pm}_{01-01} = \frac{\omega\epsilon_0 n_1^2 n(z)\nu}{4}\int_0^{2\pi} d\phi \int_0^{a_1} (re^{\mp 2i\frac{\pi}{\Lambda}r\cos\phi\sin\theta}) \times (E_r^{01}E_r^{01*} + E_\phi^{01}E_\phi^{01*})dr \quad (3.18)$$

$$f_{01-01} = \frac{\omega\epsilon_0 n_1^2 n(z)}{2}\int_0^{2\pi} d\phi \int_0^{a_1} (r) \times (E_r^{01}E_r^{01*} + E_\phi^{01}E_\phi^{01*})dr \quad (3.19)$$

where E_r^{01}, E_ϕ^{01} are the radial and azimuthal components of the electric field of the fundamental core mode, ω is the angular frequency, a_1 is the core radius, n_1 is the average RI of the core region, ν is an scaling factor and $n(z)$ is the RI modulation along z directions. These equations can be utilized to find the different coupling coefficients and employ the previously PUA approach to estimate the performance of the TFBGs. However, it should be noted that the above mentioned approach will provide correct result only for tilting angle $\theta < 20^\circ$. Other approaches for estimating the performance of TFBGs using full vectorial method, TMM approach are well discussed in [182, 183, 184].

3.3 Simulation Methodology and Results

3.3.1 Simulation Methodology

For simulation, we have employed eqn. (3.14) to write an in-house code in MATLAB® R2021a to estimate the reflected signal spectrum for different cascaded FBG structures. To validate our in-house code, we have simulated a CFBG with the design parameters: $L = 4.5$ cm, $\Delta n = 7.5\times10^{-4}$, $\Lambda = 524$ nm, and chirp rate of +6.73 nm/cm. The same design parameters are utilized in an experimental study as mentioned in [25]. The obtained simulation result is matching with the experimental results obtained in [25]. From simulation, the estimated value of λ_B is approximately 1550 nm while the same is also reported value in [25]. Similarly the estimated normalized reflectivity using our code is 0.8799 while the reported reflectivity of such CFBG is 0.7702. A slight mismatch is present as the insertion loss (IL) of the measuring equipment is not considered in our code. So, the accuracy for the obtained

value of 0.7702 with the existing value of 0.8799 is approximately 12.47%. As the results obtained using our in-house code are corroborating with the experimental study, we have employed the same code for simulating the proposed structures in this chapter.For simulation, we have considered that the proposed structure will be operating in C-band (1530-1565 nm), and the number of uniform FBGs are chosen to be 150 for each CFBG. We also assumed that each of the CFBGs is built on SMF-28, and each has a length L of 70 mm, while Δn_{max} is fixed for each PUA section. The number of grating periods considered in each FBG section of length 0.466 mm was found to be 878. The design parameters and other spectral characteristics of different CFBGs are listed in Table-3.1.As per the simu-

Table 3.1: Spectral Characteristics of Individual CFBGs

CFBG	$\mathbf{\Delta n_{max}}$	**Chirp rate (nm/cm)**	**Reflectivity (%)**	**FWHM (nm)**	λ_B **(nm)**
I	5×10^{-4}	1	88.67	7.87	1553.41
	6×10^{-4}	1	95.66	8.16	1553.47
	7×10^{-4}	1	98.60	8.45	1553.64
II	5×10^{-4}	-1	88.67	7.87	1546.33
	6×10^{-4}	-1	95.66	8.16	1546.47
	7×10^{-4}	-1	98.60	8.45	1546.62

lated spectral characteristics, the individual CFBG offers wider FWHM (maximum 8.45 nm) making them unsuitable for narrow-band filter applications. This is true for both LIC (Design I) and LDC (Design II) based CFBGs. To reduce the FWHM of such CFBGs, we have cascaded one LIC CFBG and one LDC CFBG as mentioned in the earlier sections. We have also considered that their chirp rate can be the same or different in each design. To design an arbitrary optical band-pass filter using the proposed configuration, we first choose the center wavelength of the proposed filter to be same with the Bragg wavelength λ_B. For our study, we have fixed $\lambda_B = 1550$ nm keeping in mind the C-band telecommunication applications. The Λ for LIC and LDC CFBGs are varied in the range of 531.18 nm to 538.13 nm, and in the range of 531.18 nm to 524.22 nm, respectively, as depicted in structure III. All other mathematical relations between different design parameters are already discussed in Section 2. A similar design rule has been employed for structure IV, where Λ is varied

between 531.18 nm to 538.13 nm for LIC CFBG and from 531.18 nm to 520.75 nm for LDC CFBG. Similarly, for Structure V, Λ has been varied between 531.18 nm to 541.60 nm for LIC-FBG and while the same for LDC CFBG is varied between 531.18 nm to 524.22 nm for LDC-FBG.

3.3.2 Proposed Experimental Setup

For proof-of-concept experiment related to the proposed structures, one can employ the experimental setup as depicted in Fig. 3.3.As illustrated, the two constituting CFBGs are to

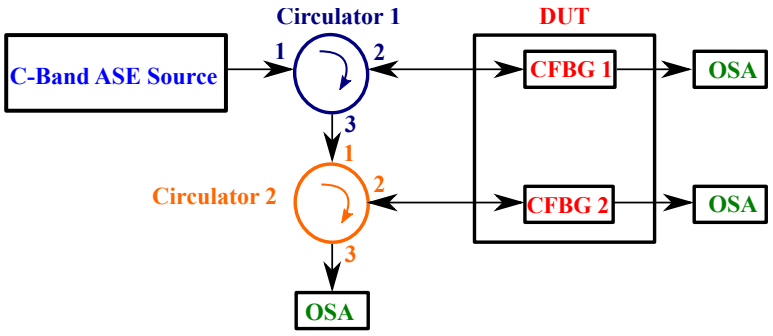

Figure 3.3: Experimental setup for the proposed cascaded structure(s).

be connected using two broadband optical circulators. The input excitation signal from the C-Band amplified spontaneous emission (ASE) source is connected to the terminal 1 of the Circulator 1. Alternatively, one can use a C-band tunable laser source instead of ASE source too. The output from of the circulator 1 (refer to port 2) will excite the CFBG 1. Most of the light will pass through CFBG 1 and only a selected band of input light will be collected in port 3 of the circulator 1. Assuming very high isolation between the ports of the circulator, the reflected signal will maintain its spectral purity. To estimate the transmitted spectrum of the CFBG 1, an optical spectrum analyzer (OSA) can be connected to the output terminal of the CFBG 1. The reflected signal from CFBG 1 is then passed to the CFBG 2 via circulator 2. A similar operation as discussed earlier will result the final reflected signal to be received at the terminal 3 of the circulator 2. To study the spectrum of the reflected signal, an OSA

can be connected to the terminal 3 of the circular 2. For this study, we have assumed that the device-under- test (DUT) is kept in a temperature-controlled enclosure. To study the effect of temperature on the proposed structure, the temperature of the enclosure should be altered gradually and the output optical spectrum at terminal 3 of the circulator 2 needs to be recorded at each temperature. Such a study can reveal thermal sensitivity of the proposed structure.

3.3.3 Simulation Results

First we have simulated a LIC based CFBG and another LDC based CFBG with design parameters $\Delta n_{max} = 7 \times 10^{-4}$ and chirp rate ± 1 nm/cm. The simulated reflected signal spectrum is depicted in Fig. 3.4(a). In Fig. 3.4(a), the spectrum in blue and green color is designated for LDC and LIC CFBGs, respectively. For the rest of the chapter, we have maintained the same legend for all simulation results. From the simulation results, the estimated values of λ_B are 1553.64 nm for LIC CFBG and 1546.62 nm for LDC CFBG, respectively, while the FWHM and reflectivity are 8.45 nm and 0.986 for both CFBGs. If we change the value of Δn_{max}, the corresponding values of FWHM, reflectivity and λ_B vary significantly. Simulation results for the same CFBG with varying Δn_{max} are listed in Table-3.1. Typically wide FWHM is desired for WDM applications, while narrower FWHM is desired for narrow-band bandpass filtering applications. To reduce the FWHM, we have connected the two CFBGs as discussed in Section 2.2.

For narrow-band BPFs applications, we have simulated three different cascaded CFBG structures (structure III, IV, and V in Fig. 3.2) in MATLAB® R2021a and the corresponding normalized reflected signal spectrums are depicted in Fig. 3.4(b-d). As per the obtained simulation results in Fig. 3.4(b), almost 6.68 nm reduction (from 8.45 nm to 1.77 nm, indicating almost fivefold change) in FWHM and approximately 17.32% reduction in the reflectivity (from 0.9860 to 0.8128).It is important to note the two different reasons behind

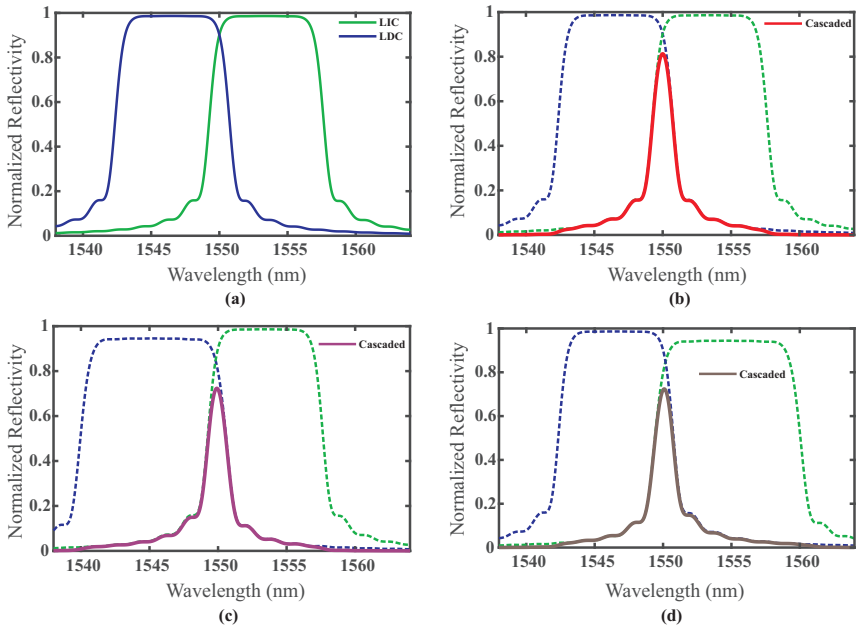

Figure 3.4: Simulated normalized reflected spectral profiles for the proposed cascaded CFBG based structures: (a) broadband spectral profiles obtained using individual CFBGs (one LIC-FBG and one LDC-FBG) with chirp rate 1 nm/cm. (b) spectral profile (red color) obtained using cascaded CFBGs with LIC and LDC of 1 nm/cm. (c) spectral profile (violet color) resulted from cascaded CFBGs with LIC of 1 nm/cm and LDC of 1.5 nm/cm. (d) Narrow-band spectral profile (brown color) gained from cascaded CFBGs with LIC of 1.5 nm/cm and LDC of 1 nm/cm.

the lower reflectivity of the cascaded structure compared to a single CFBG structure. At first, in cascaded dual CFBGs structure additional device insertion loss is introduced and hence reduction in the reflectivity. Secondly, the Bragg wavelength of the cascaded structure is significantly different from the Bragg wavelength of each constituting CFBGs. For example refer to Fig. 3.4(a-b). The Bragg wavelength of the constituting LIC and LDC are 1553.64 nm and 1546.62 nm, respectively while the cascaded structure offers the center wavelength of 1550 nm, which is almost ± 3.51 nm far way from each constituting CFBG. At 1550 nm, the LIC and LDC CFBG offers a normalized reflectivity of 0.9012 and 0.9018. Since the reflectivity of each CFBGs are already low hence the overall reflectivity at 1550 nm is also low (approximately 0.8128) due to the cascaded structure. It is imperative to state that further refinement in design parameter can improve the overall normalized reflectivity in the proposed structure. In this case, the considered CFBG design parameters are

$\Delta n_{max} = 7 \times 10^{-4}$, and chirp rate $= \pm 1$ nm/cm. In this design, we have optimized the response of cascaded CFBG in such a way that we can achieve λ_B for the combined structure to be 1550 nm. However, the value of λ_B for cascaded structure is a strong function of chirp rate which we shall discuss later in this chapter. Keeping the chirp rate constant for both CFBGs, if we vary the value of Δn_{max}, then we can optimize the normalized reflectivity of the system and such simulation results are listed in Table-3.2. Next, we have considered that Structure-IV (as per Fig. 3.2), where the chirp rate of LIC CFBG is 1 nm/cm while the chirp rate of LDC CFBG is -1.5 nm/cm. Intuitively, we can expect a reduced FWHM in such a cascaded system while there will be a change in λ_B and normalized reflectivity. Simulation results for such a system are shown in Fig. 3.4(c). For such a system, the simulated value of normalized reflectivity, and λ_B are 0.7239, and 1549.92 nm at Δn_{max} of 7×10^{-4}. In such case, the 3-dB wavelengths of the FBG are 1549.06 nm and 1550.80 nm, resulting a FWHM of 1.74 nm. However, if we change Δn_{max} to 5×10^{-4}, then the corresponding FWHM, normalized reflectivity, and λ_B changes to 1.58 nm, 0.3884, and 1549.94 nm, respectively. Results for $\Delta n_{max} = 6 \times 10^{-4}$, are incorporated in Table-3.2. In the third variant of design (Structure-V as per Fig. 3.2), we have considered the chirp rate of LIC CFBG increases to +1.5 nm/cm while the chirp rate of LDC CFBG reduces to -1 nm/cm. In such case, if we consider $\Delta n_{max} = 7 \times 10^{-4}$, then the estimated values of the normalized reflectivity, and λ_B are 0.7239, and 1550.07 nm. In this case, the 3-dB wavelengths of the FBG are 1549.19 nm and 1550.93 nm, exhbiting a FWHM of 1.74 nm. Further reduction in FWHM can be achieved if we change the value of Δn_{max} to 5×10^{-4} at the expense of reflectivity of the cascaded system. As mentioned earlier, we have noticed a shift in λ_B with varying chirp rates for both LIC CFBG and LDC CFBG. Analytically this shifting can also be estimated using the following relations [35, 39],

$$\lambda_B = \lambda + \frac{c\tau(\lambda)\Delta\lambda_{chirp}}{2n_{eff}L_g} \tag{3.20}$$

where $\Delta\lambda_{chirp}$ denotes the chirped bandwidth, $\tau(\lambda)$ is the time delay for each wavelength along the CFBG, and c is the speed of light.

Table 3.2: Spectral Characteristics of Proposed Structure(s)

Cascaded CFBG structure	$\mathbf{\Delta n_{max}}$	**Reflectivity (%)**	**FWHM (nm)**	λ_B **(nm)**
III	5×10^{-4}	48.15	**1.56**	1550.00
	6×10^{-4}	66.92	1.66	1550.00
	7×10^{-4}	81.28	1.77	1550.00
IV	5×10^{-4}	38.84	**1.58**	1549.94
	6×10^{-4}	56.82	1.61	1549.92
	7×10^{-4}	72.39	1.74	1549.92
V	5×10^{-4}	38.84	**1.58**	1550.05
	6×10^{-4}	56.82	1.61	1550.07
	7×10^{-4}	72.39	1.74	1550.07

3.3.4 Effect of Temperature on the Proposed Structure(s)

Generally, the performance of FBGs are sensitive to temperature variations. Hence, the study of temperature effect in the proposed structure utilizing CFBGs will help designer for athermal designs. The temperature dependence of the refractive index n(T) in the grating region of an FBG can be written as [186], $n(T) = n_0 + \beta_n T$, where $n(T)$ and n_0 are the refractive index at temperatures T and 0°C, respectively. β_n is the first order thermo-optic coefficient of silica fiber and is assumed to be $1.045 \times 10^{-5}/$°C. Considering PUA models of CFBGs, the dependence of λ_B on temperature in absence of strain can be expressed as [18],

$$\Delta\lambda_B = (\alpha + \beta_n)\, \Delta T\, \lambda_B \tag{3.21}$$

where $\alpha = 0.55 \times 10^{-6}/$°C is the thermal expansion coefficient of the fused silica [186], [68], [187], [188].We have considered this theory in our simulation study. It is also very important to note that, the proposed dual cascaded structures will offer higher thermal sensitivity compared to a single CFBG based structure. As the variation of temperature affects the Bragg wavelength of both constituting CFBGs, it is expected that the thermal sensitivity will be enhanced in proposed cascaded structure. To validate this inference, we have

simulated a single CFBG with $\Delta n = 7 \times 10^{-4}$ and chirp rate of +1 nm/cm over a temperature range of 0 to 100°C and estimated the thermal sensitivity of such structure to be approximately 13.04 pm/°C. In Fig. 3.5(a), and Fig. 3.5(b), we have incorporated the simulation results indicating the effect of the temperature on the performance of the proposed devices.As depicted, the thermal shifting of λ_B can be observed clearly with varying op-

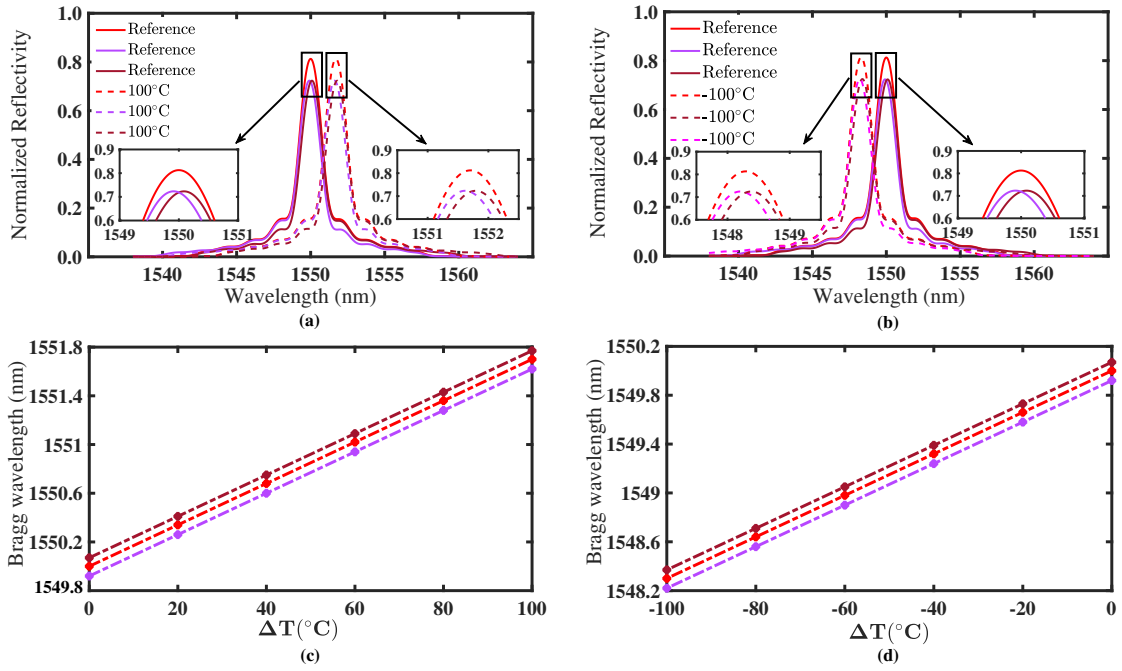

Figure 3.5: Effect of temperature on proposed structure(s): (a) complete spectrum shift in λ_B for $\Delta T = +100$°C in a step of +20°C, (b) complete spectrum shift in λ_B for $\Delta T = -100$°C in a step of −20°C, (c) estimated values of λ_B w.r.t ΔT for 0 to 100°C (d) estimated values of λ_B w.r.t ΔT for 0 to −100°C.

erating temperature. Simulated narrow-band spectral profiles (red, violet, and solid brown lines) are superimposed at reference temperature (i.e., ΔT = 0). If $\Delta T = 100$°C, then λ_B shifts +1.701 nm. This change can be visible for all the designs. λ_B shifts from 1550 nm to 1551.701 nm, 1549.92 to 1551.621 nm, and 1550.07 to 1551.771 nm for structure III, IV, and V, respectively. A similar kind of shift in λ_B can be observed from Fig. 3.5(b) for $\Delta T = -100$°C. The shifted λ_B for structure III, IV, and V are 1548.299 nm, 1548.219 nm, and 1548.369 nm, respectively. Intuitive calculation reveals an average thermal sensitivity

of 17.01 pm/°C over ± 100°C for all the proposed structures. As expected, the thermal sensitivity of the proposed structure(s) is higher compared to a single CFBG structure which is also confirmed in [25, 50, 161, 189, 190]. Further investigation reveals a linear dependence of λ_B on ΔT, when operating temperature is varied from -100°C to 0°C. These variations in λ_B with ΔT are illustrated in Fig. 3.5(c-d).

3.3.5 Comparative Study

A comparative study between the proposed structures and other recently reported similar structures are also carried out in Table-3.3. The study is done in terms of the type of FBG, number of FBGs used for cascading, FWHM, and temperature sensitivity. A cascaded FBG structure formed with four uniform FBG to reduce the dispersion of an optical signal in a WDM system has been reported in [35]. Similarly, a narrow-band with minimized side-lobes in the reflection spectrum can be gained with the proposed cascaded uniform FBG structure is presented in [154]. Also, various apodized grating functions such as Barthan, Hamming, Nuttal, and Sinc functions are used to optimize the spectral characteristics of a proposed structure. In case of uniform cascaded FBGs, the achieved FWHM is 0.16 nm while the lowest FWHM reported by the authors are 0.008 nm using apodized FBGs. However, one should note that, the reflectivity decreases as the number of FBGs in a structure increases. So, to improve the reflectivity, a cascaded uniform FBGs structure of varying lengths has been introduced [191]. Such an introduced structure with four FBGs has given a FWHM of 0.177 nm. An apodized cascaded FBG structure is also recently reported in [155] to reduce the spectral width of the pulse and thus enhancing the system performance. Such structure offers a FWHM of 0.102 nm with Cauchy's apodization function. In this study, we have considered only CFBGs based structures (one LIC-FBG and the other LDC-FBG). In the other studies mentioned here, no one has calculated the effect of temperature in the spectral profile. The proposed devices in this chapter offer wider FWHM which can

be further reduced by increasing the number of CFBGs without significant reduction in reflectivity of the overall structure.

Table 3.3: Comparative study of various recently reported cascaded FBG structures

Year	Ref.	Type of FBG	Number of FBGs cascaded	FWHM (nm)	Temperature Sensitivity
2020	[35]	Uniform	04	-	-
2020	[154]	Uniform & Apodized	04	0.16 & 0.008	-
2020	[191]	Uniform	04	0.177	-
2021	[155]	Apodized	04	0.102	-
2022	Present work	Chirped (LIC and LDC)	02	1.56	17.01 pm/°C

3.4 Conclusion

In this chapter, we have proposed a cascaded CFBG based narrow-band bandpass filter operating in the C-band. Cascading one LIC-FBG with another LDC-FBG reduces the FWHM almost five folds while the overall reflectivity reduces by 17.32% compared to a single CFBG is presented. A suitable analytical formulation based on a piecewise uniform approach (PUA) for the proposed structure(s) is also incorporated in this chapter. For the three proposed structures, we have considered each CFBG may have equal or different chirp rates keeping all other design parameters the same. As per the simulation results, the narrowest and widest FWHM achieved by the proposed structures is 1.56 nm and 1.77 nm, respectively. In such designs, the highest and lowest reflectivity offered by the cascaded CFBG structures is approximately 0.81 and 0.39. The effect of temperature on the spectral characteristics of all the proposed structures is also studied. Simulation results reveal that λ_B of the proposed cascaded structures have a linear dependence on ΔT. Estimated thermal sensitivity is found to be 17.01 pm/°C for all the proposed structures.

Chapter 4

Narrow-band Optical Bandpass Filter Using Dual Cascaded Apodized Linearly Chirped FBGs

4.1 Introduction

Chirped fiber Bragg gratings (CFBGs), a passive optical device, in some portion of the core of an optical fiber (single mode or multi-mode fiber), can be modelled by varying the refractive index modulation amplitude and/or period of the refractive index modulation along the grating length [168, 169, 170]. Usually, for practical applications that include sensing and communications, CFBGs have gained significant attention due to their inherent advantages. The reason for using CFBGs or non-uniformity gratings in the core is to reduce the side lobes in the reflection spectrum, which are undesirable as in their uniform counterpart. In addition to this, they are also used for dispersion compensation and pulse shaping purposes [173, 174, 176, 177]. In comparison to the CFBGs, apodized linearly chirped fiber

Bragg gratings (LCFBG) have proved to be an effective solution to compensate the chromatic dispersion of high bit-rate optical communicationsystems [63, 192]. However, owing to advantages such as narrow bandwidth and reduced strength of sidelobes in the reflection spectrum, the cascaded FBG or CFBG structures for communication purposes are currently being in use. Hence, the study of spectral characteristics using cascaded apodized CFBGs is needed. In this chapter, we propose narrow band BPFs by cascading dual apodized CFBGs (one with linearly increased chirp (LIC) and another with linearly decreased chirp (LDC), and we analyse the performance of these BPFs. One apodized CFBG's reflection has been used as the input for the other apodized CFBG in the suggested structure(s). We have considered the chirp rates of two CFBGs may be the same or different. The analytical formulation of the suggested cascaded linearly apodized CFBG structures utilizing the PUA approach is described in Section 4.2. Section 4.3 contains simulation findings that support the analytical formulation of three distinct linearly apodized cascaded CFBG structures. Additionally, the impact of various operating temperatures on the proposed structures is discussed here. Finally, we concluded the chapter in section 4.4.

4.2 Analytical Formulation for Proposed structure(s)

The reflected spectrum of a single apodized CFBG shown in Fig. 3.1(a) can be estimated with eqn. (3.11). Here, the reflectivity from each section of a CFBG was denoted with $r_j(\lambda)$. Since we have considered apodized CFBGs instead normal CFBGs in this work, the value of κ can be considered as per the eqn. (2.14) and eqn. (2.16). So the reflectivity of structure I and structure II of Fig. 4.1 changes accordingly. In structure III of Fig. 4.1, the reflected optical signal B_{01} from a apodized LIC CFBG is given as the input optical signal A_{02} to apodized LDC CFBG and thus gives a condition $B_{01} = A_{02}$. Similar kind of profile can be attained even the chirp rates of a apodized CFBG varied. The varying chirp rate cases are considered for different structures (structure IV and structure V) are described in Fig.

4.1.Mathematically, one can represent the reflectivity of a proposed structures (Structure III,

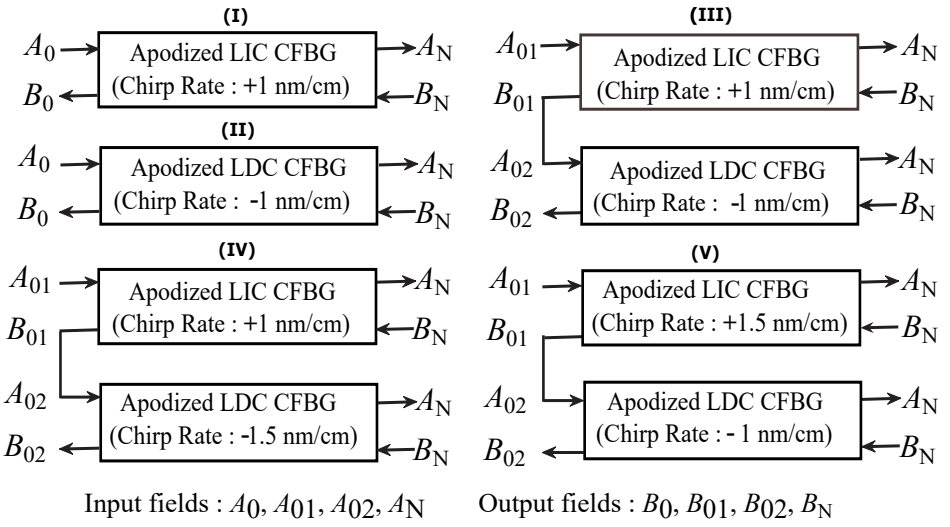

Figure 4.1: Block diagram representation of various apodized CFBGs. Structure I and II indicates individual apodized LIC and LDC CFBG. Structure III, IV and V indicates cascading scheme of apodized LIC and apodized LDC CFBGs with same and different chirp rates.

structure IV and structure V) can be demonstrated as,

$$R_{cascaded}(\lambda) = \left|\frac{B_{02}(\lambda)}{A_{01}(\lambda)}\right|^2 = \left|\frac{B_{01}(\lambda)}{A_{01}(\lambda)}\right|^2 \left|\frac{B_{02}(\lambda)}{A_{02}(\lambda)}\right|^2 \tag{4.1}$$

The above equation (i.e., eqn. (4.1)) can also be estimated as mentioned in eqn. (3.11) as ,

$$R_{cascaded}(\lambda) = \left[1 - \prod_{j=1}^{N}(1 - r_j(\lambda))\right]\left[1 - \prod_{k=1}^{N}(1 - r_k(\lambda))\right] \tag{4.2}$$

where r_j is the reflection from j^{th} section of apodized LIC grating and r_k is the reflection from k^{th} section of apodized LDC grating. The above equation can be rearranged as,

$$\begin{aligned} R_{cascaded}(\lambda) = 1 - \prod_{k=1}^{N}(1 - r_k(\lambda)) \; - \prod_{j=1}^{N}(1 - r_j(\lambda)) \\ + \prod_{j=1}^{N}\prod_{k=1}^{N}(1 - r_j(\lambda))\,(1 - r_k(\lambda)) \end{aligned} \tag{4.3}$$

Considering equal number of sections in both apodized LIC and LDC CFBGs, eqn. (4.3) can further be reshaped as,

$$R_{cascaded}(\lambda) = 1 - 2\prod_{m=1}^{N}(1 - r_m(\lambda)) + \prod_{m=1}^{N}(1 - r_m(\lambda))^2 \tag{4.4}$$

4.3 Simulation methodology and results

4.3.1 Simulation Methodology

To estimate the reflected signal spectrum for various cascading of apodized CFBG structures, we used eqn. (4.4) to create an in-house MATLAB® R2021a code for simulation. For simulation, we assumed that the proposed structure would operate in the C-band (1530–1565 nm), and 150 sections (each section is assumed to be a uniform FBG) are used for piecewise approximation of the entire length of CFBG. We further assumed that Δn_{max} is fixed for each PUA section, and that each CFBG is constructed on SMF-28 with a length L of 70 mm. The design parameters and other spectral characteristics of different apodized CFBGs are listed in Table-4.1 and Table-4.2 for Gaussian and Hyperbolic tangent functions respectively.

According to the simulated spectral characteristics, the individual apodized CFBG have wider FWHM (maximum of 8.25 nm and 8.45 nm for Gaussian and hyperbolic tangent apodizations respectively), which makes them unsuitable for applications requiring narrow-band filters. This holds true for both apodized LIC and LDC-based (Design I and II) CFBGs. To reduce the FWHM of such CFBGs, we have cascaded oneapodized LIC CFBG and one apodized LDC CFBG as mentioned in the earlier sections. We have also taken into account the possibility that each designs chirp rate could be the same or different. Initially, we initially selected the centre wavelength of the proposed filter to be the same as the Bragg

Table 4.1: Spectral characteristics of individual Gaussian apodized CFBGs

Apodized CFBG	Δn_{max} ($\times 10^{-4}$)	Chirp rate (nm/cm)	$\alpha = 0.5$			$\alpha = 1$			$\alpha = 2$		
			Reflectivity (%)	FWHM (nm)	λ_B (nm)	Reflectivity (%)	FWHM (nm)	λ_B (nm)	Reflectivity (%)	FWHM (nm)	λ_B (nm)
	5	1	81.73	7.73	1553.46	73.46	7.57	1553.41	55.43	7.37	1553.39
I	6	1	91.35	7.99	1553.33	85.20	7.80	1553.23	68.76	7.52	1553.14
	7	1	96.43	8.25	1553.15	92.57	8.04	1553.14	79.48	7.68	1553.12
	5	-1	81.73	7.73	1546.56	73.46	7.57	1546.46	55.43	7.37	1546.32
II	6	-1	91.35	7.99	1546.47	85.20	7.80	1546.28	68.76	7.52	1546.14
	7	-1	96.43	8.25	1546.38	92.57	8.04	1546.17	79.48	7.68	1546.06

Table 4.2: Spectral characteristics of individual apodized CFBGs with Hyperbolic tangent function

Apodized CFBG	Δn_{max} ($\times 10^{-4}$)	Chirp rate (nm/cm)	$\alpha = \beta$			$\alpha < \beta$			$\alpha > \beta$		
			Reflectivity (%)	FWHM (nm)	λ_B (nm)	Reflectivity (%)	FWHM (nm)	λ_B (nm)	Reflectivity (%)	FWHM (nm)	λ_B (nm)
	5	1	88.65	7.90	1553.46	87.79	7.88	1553.23	54.19	7.42	1553.41
I	6	1	95.65	8.19	1553.33	95.16	8.20	1553.41	67.50	7.51	1553.41
	7	1	98.60	8.44	1553.28	98.38	8.45	1553.23	78.35	7.68	1553.51
	5	-1	88.79	7.88	1546.51	87.93	7.89	1546.38	54.38	7.43	1546.33
II	6	-1	95.72	8.20	1546.28	95.24	8.13	1546.28	67.71	7.52	1546.38
	7	-1	98.63	8.45	1546.87	98.42	8.40	1546.28	78.53	7.68	1546.38

wavelength λ_B in order to create an arbitrary optical band-pass filter using the proposed configuration. For our study, we have fixed $\lambda_B = 1550$ nm keeping in mind the C-band telecommunication applications. According to structure III, the Λ for apodized LIC and apodized LDC CFBGs varies between 531.18 nm and 538.13 nm and between 531.18 nm and 524.22 nm, respectively. All other mathematical relationships between various design parameters are already covered in Section 4.2. A similar design rule has been employed for structure IV, where Λ is varied between 531.18 nm to 538.13 nm for apodized LIC CFBG and from531.18 nm to 520.75 nm for apodized LDC CFBG. Similarly, for Structure V, Λ has beenvaried between 531.18 nm to 541.60 nm for apodized LIC-FBG and while the same forapodized LDC CFBG is varied between 531.18 nm to 524.22 nm for apodized LDC-FBG.

4.3.2 Proposed Experimental Setup

For a practical perspective, one can employ the experimental setup depicted in Fig. 4.2. As illustrated, the two apodized CFBGs are to be connected using two broadband optical circulators. The input optical signal generated from a C-band amplified spontaneous emission (ASE) source is given to terminal 1 of circulator 1.The output from circulator 1 (refer to port

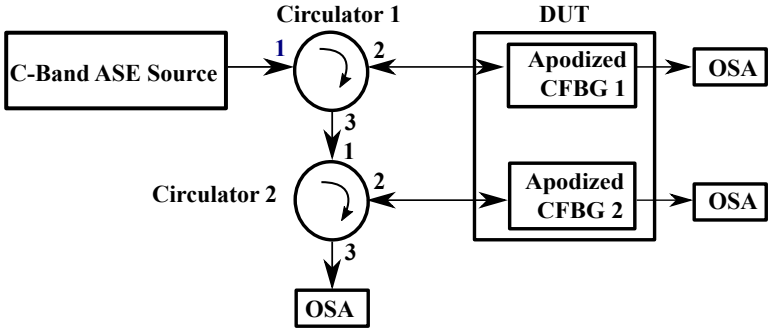

Figure 4.2: Experimental setup for the proposed cascaded structure(s).

2) will excite apodized CFBG 1. Most of the light will pass through apodized CFBG 1 and only a selected band of input light will be collected in port 3 of the circulator 1. Assuming very high isolation between the ports of the circulator, the reflected signal will maintain its spectral purity. To estimate the transmitted spectrum of the apodized CFBG 1, an optical spectrum analyzer (OSA) can be connected to the output terminal of the CFBG 1. The reflected signal from apodized CFBG 1 is then transmitted to apodized CFBG 2 through circulator 2. The final reflected signal will be received at terminal 3 of circulator 2 as a result of an operation similar to that earlier mentioned. For this study, we have assumed that the device-under- test (DUT) is kept in a temperature-controlled enclosure. To study the effect of temperature on the proposed structure, the temperature of the enclosure should be altered gradually and the output optical spectrum at terminal 3 of the circulator 2 needs to be recorded at each temperature. Such a study can reveal thermal sensitivity of the proposed structure.

4.3.3 Simulation Results

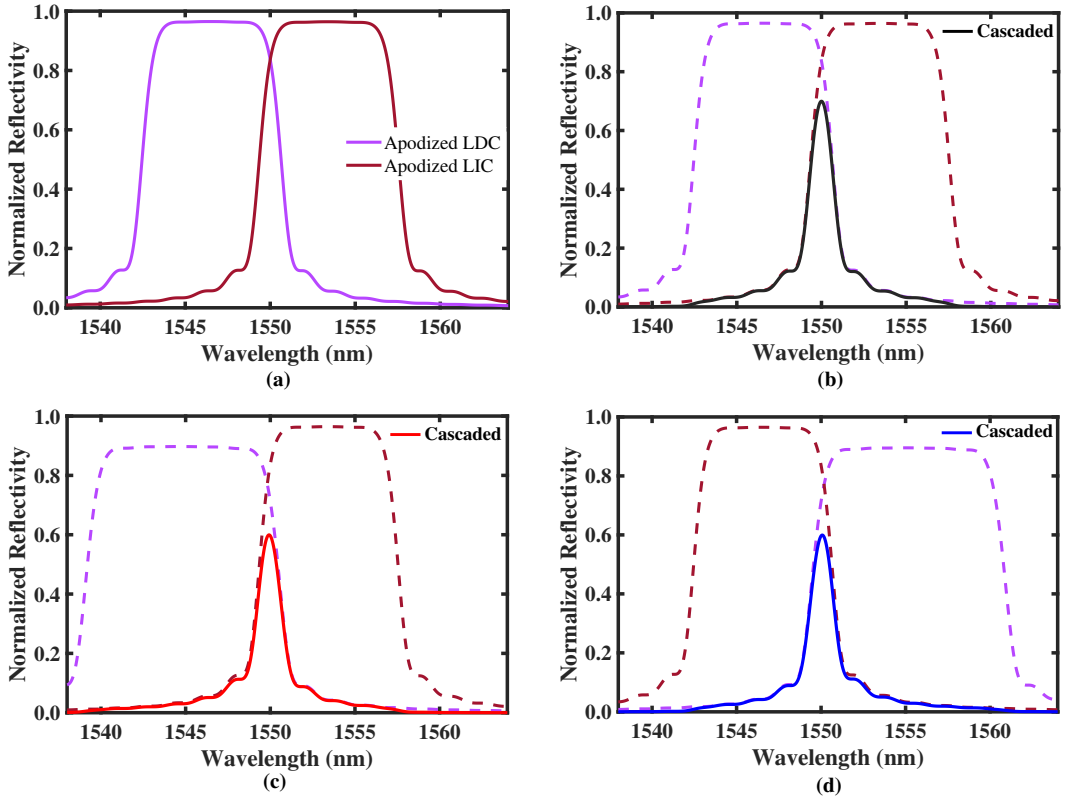

Figure 4.3: Simulated normalized reflected spectral profiles for the proposed cascading of Gaussian apodized CFBG based structures at an α of 0.5: (a) broadband spectral profiles obtained using individual apodized CFBGs (one apodized LIC-FBG and one apodized LDC-FBG) with chirp rate 1 nm/cm. (b) spectral profile (black color) obtained using cascading of apodized CFBGs with LIC and LDC of 1 nm/cm. (c) spectral profile (red color) resulted from cascading of apodized CFBGs with LIC of 1 nm/cm and LDC of 1.5 nm/cm. (d) Narrow-band spectral profile (blue color) gained from cascading of apodized CFBGs with LIC of 1.5 nm/cm and LDC of 1 nm/cm.

First, using the design parameters $\Delta n_{max} = 7 \times 10^{-4}$ and chirp rate 1 nm/cm, we simulated a Gaussian apodized LIC-based CFBG and another Gaussian apodized LDC-based CFBG. Fig.4.3 shows the spectrum of the simulated reflected signal. The violet and brown portions of the spectrum in Fig. 4.3 correspond to the apodized LDC and apodized LIC CFBGs, respectively. We have kept the same legend for all simulation results throughout the rest of the chapter. According to the simulation findings, the estimated values of λ_B

for the apodized LIC CFBG and apodized LDC CFBG are 1553.15 nm and 1546.38 nm, respectively. The FWHM and reflectivity for both CFBGs are 8.45 nm and 0.964, respectively. If we change the value of Δn_{max}, the corresponding values of FWHM, reflectivity and λ_B vary significantly. The same is true for different values of α. Simulation results for different Gaussian apodized CFBGs with varying Δn_{max} and α are shown in Table-4.1. But, Table-4.2 will give us the spectral characteristics of Hyperbolic tangent apodized CFBGs for different cases of α and β. For α=β, we have considered both the values are equal to 0.1. When $\alpha < \beta$, α has a value of 0.1 and β of 1.2. For $\alpha > \beta$, α has a value of 1.2 whereas β has a value of 0.1. It is evident from Table-4.2 that the reflectivity attained for the case α=β recorded as approximately 98.60$\%$ for both the apodized FBGs. The FWHM for both the CFBGs are noted as approximately 8.45 and λ_B for an LIC and LDC based CFBGs are marked as 1553.28 nm and 1546.87 nm, respectively. If we change the value of Δn_{max}, the corresponding values of FWHM, reflectivity and λ_B vary significantly for both the CFBGs. The same is true for different cases of α and β. Typically wide FWHM is desired for WDM applications, while narrower FWHM is desired for narrow-band bandpass filtering applications. To reduce the FWHM, we have connected the two apodized CFBGs as discussed in section 4.2.

Table 4.3: Spectral characteristics of proposed structure(s) with Gaussian apodized CFBGs

Apodized CFBG	$\mathbf{\Delta n_{max}}$ ($\times 10^{-4}$)	$\alpha = 0.5$			$\alpha = 1$			$\alpha = 2$		
		Reflectivity (%)	**FWHM (nm)**	λ_B **(nm)**	**Reflectivity (%)**	**FWHM (nm)**	λ_B **(nm)**	**Reflectivity (%)**	**FWHM (nm)**	λ_B **(nm)**
III	5	36.39	1.55	1550.00	26.42	1.49	1550.00	12.65	1.46	1550.00
	6	54.12	1.61	1550.00	41.74	1.54	1550.00	21.99	1.51	1550.00
	7	69.95	1.66	1550.00	57.25	1.58	1550.00	33.34	1.56	1550.00
IV	5	28.49	1.57	1549.97	20.18	1.53	1549.97	09.31	1.51	1549.97
	6	44.34	1.59	1549.95	33.12	1.54	1549.95	16.61	1.50	1549.95
	7	59.94	1.64	1549.92	47.30	1.58	1549.92	25.91	1.55	1549.92
V	5	28.49	1.57	1550.02	20.18	1.53	1550.02	09.31	1.51	1550.02
	6	44.33	1.59	1550.04	33.12	1.54	1550.04	16.61	1.50	1550.04
	7	59.94	1.64	1550.07	47.30	1.58	1550.07	25.91	1.55	1550.07

For narrow-band BPF applications, three distinct cascaded apodized CFBG structures (structures III, IV, and V in Fig. 4.2) have been simulated in MATLAB® R2021a and the corresponding normalized reflected spectrums are depicted in Fig. 4.3(b-d). According to

Table 4.4: Spectral characteristics of proposed structure(s) with Hyperbolic tangent apodization

Apodized CFBG	Δn_{max} ($\times 10^{-4}$)	$\alpha = \beta$			$\alpha < \beta$			$\alpha > \beta$		
		Reflectivity (%)	FWHM (nm)	λ_B (nm)	Reflectivity (%)	FWHM (nm)	λ_B (nm)	Reflectivity (%)	FWHM (nm)	λ_B (nm)
III	5	48.12	1.54	1550.00	46.41	1.56	1550.00	11.97	1.46	1550.00
	6	66.89	1.64	1550.00	65.15	1.66	1550.00	20.93	1.51	1550.00
	7	81.25	1.75	1550.00	79.82	1.76	1550.00	31.91	1.56	1550.00
IV	5	38.81	1.55	1549.95	37.27	1.57	1549.95	08.79	1.53	1549.92
	6	56.79	1.64	1549.94	55.02	1.59	1549.92	15.76	1.53	1550.00
	7	72.36	1.71	1549.92	70.71	1.73	1549.92	24.71	1.55	1549.97
V	5	38.81	1.57	1550.05	37.27	1.59	1550.05	08.79	1.55	1549.97
	6	56.79	1.62	1550.05	55.02	1.64	1550.08	15.76	1.53	1550.02
	7	72.35	1.73	1550.08	70.70	1.71	1550.10	24.71	1.56	1550.05

the simulation findings shown in Fig. 4.3(b), the FWHM was reduced by nearly 6.59 nm (from 8.25 nm to 1.66 nm, for $\alpha = 0.5$ representing a nearly fivefold shift), and the reflectivity was decreased by about 26.48% (from 0.9643 to 0.6995). The two distinct causes of the cascaded structure's decreased reflectivity relative to a single apodized CFBG structure must be noted. First, additional device insertion loss and a resulting decrease in reflectivity are introduced in the cascaded dual CFBGs structure. Second, each apodized CFBG that makes up the cascaded structure has a significantly different Bragg wavelength than with the Bragg wavelength of the designed structure. In this case, the considered designed parameters such as chirp rate and Δn_{max} are chosen to be as $\pm$ 1 nm and 7×10^{-4}. In this design, in order to obtain λ_B for the combined structure to be 1550 nm, we have optimised the cascaded apodized CFBG response. If we change the value of Δn_{max} while keeping the chirp rate constant for both the apodized CFBGs, we can improve the system's normalised reflectivity. Such simulation results are shown in Table-4.3. Next, we have considered structure -IV(shown in Fig. 4.1), where the chirp rate of an LDC CFBG is -1.5 nm/cm while the chirp rate of apodized LIC CFBG is 1 nm/cm. In such a cascaded system, it makes intuitive sense to anticipate a reduced FWHM while observing a change in λ_B and normalised reflectivity. Simulation results for such a structure are shown in Fig. 4.3(c). For such a structure, the simulated value of the reflectivity, FWHM and λ_B are 59.94%,1.64 nm and 1549.92 nm respectively at Δn_{max} of 7×10^{-4}. However, if we change the value of Δn_{max} to 5×10^{-4} then the corresponding reflectivity, FWHM and λ_B changes to 28.49%, 1.57

nm and 1549.97 nm respectively. The spectral characteristics related to Δn_{max} of 6×10^{-4} are incorporated in Table-4.3. In the third design or structure -V(shown in Fig. 4.1), the value of chirp rate for an apodized LDC CFBG is -1 nm/cm while the chirp rate of apodized LIC CFBG is 1.5 nm/cm. In such a cascaded system, it makes intuitive sense to anticipate a reduced FWHM while observing a change in λ_B and normalised reflectivity. Simulation results for such a structure are shown in Fig. 4.3(d). For such a structure, the simulated value of the reflectivity, FWHM and λ_B are 59.94%,1.64 nm and 1550.07 nm respectively at Δn_{max} of 7×10^{-4}. However, if we change the value of Δn_{max} to 5×10^{-4} then the corresponding reflectivity, FWHM and λ_B changes to 28.49%, 1.57 nm and 1550.02 nm respectively. A shift in λ_B with varying chirp rates for both apodized LIC and LDC CFBGs can be analytically estimated using eqn. (3.20). However, for different values of α, changes in the spectral attributes of various designs of Fig. 4.1 for the Gaussian apodization is incorporated in Table-4.3. One can note from Table-4.3 that at a fixed value of Δn_{max}, the reflectivity and FWHM are getting reduced as the α increases from 0.5 to 2. Also, a maximum reflectivity of 69.95% for the case $\alpha = 0.5$ and a minimum FWHM of 1.46 nm for the case $\alpha = 2$ are recorded. Similarly, if we consider hyperbolic tangent apodization, one can note from Table-4.4 that at a fixed value of Δn_{max}, the reflectivity and FWHM are getting reduced for all the cases considered for different designs. In all such designs, a maximum reflectivity of 81.25 % for the case $\alpha = \beta$ and a minimum FWHM of 1.46 nm for the case $\alpha > \beta$ are recorded.

4.3.4 Effect of Temperature on the Proposed Structure(s)

FBG performance is typically sensitive to temperature variations. Therefore, the study of the influence of temperature on the proposed structure using apodized CFBGs will help in the development of athermal designs. In the grating region of an FBG, the temperature dependence of the refractive index n(T) can be expressed as $n(t) = n_0 + \beta_n T$, where n_0 and $n(T)$ are the refractive index at temperatures $0°$C and T, respectively. The first order

thermo-optic coefficient of silica fiber and is considered to be $1.045 \times 10^{-5}/^{\circ}$C. Addressing PUA models of apodized CFBGs, the dependence of λ_B on temperature in the absence of strain can be represented as,

$$\Delta\lambda_B = (\alpha + \beta_n)\, \Delta T\, \lambda_B \tag{4.5}$$

where $\alpha = 0.55 \times 10^{-6}/^{\circ}$C is the thermal expansion coefficient of the fused silica [186], [68], [187], [188].This theory was considered in our simulation study. It is important to note that , the proposed dual cascaded structures will have a greater thermal sensitivity than a single CFBG-based structure. As temperature variation influences the Bragg wavelength of both constituting apodized CFBGs, it is anticipated that the thermal sensitivity of the proposed cascaded structure will be increased. We have included simulation results showing the impact of temperature on the performance of the suggested devices in Fig. 4.4(a) and Fig. 4.4(b).With various operating temperatures, the thermal shifting of λ_B can be seen clearly, as shown. The spectral profiles (black,red and blue solid lines) shown are superimposed at a reference temperature ($\Delta T = 0$). If ΔT changes to 100°C then corresponding change in λ_B shifts the spectrum to +1.702 nm. This change can be reflected to all designs. The shift in λ_B from 1550 nm to 1551.702 nm , 1549.92 to 1551.622 nm, and 1550.07 to 1551.772 nm for structure III, IV and V shown in Fig. 4.4(a). A similar kind of shift can be observed for ΔT = 100°C and the same is depicted in Fig. 4.4(b). The change in λ_B to 1548.298 nm, 1548.218 nm, and 1548.368 nm for structure III, IV and V, respectively. All proposed structures have an average thermal sensitivity of 17.02 pm/°C over $\pm 100^{\circ}$C, according to intuitive calculation. Further investigation reveals a linear relationship between λ_B and ΔT when the operating temperature is varied from $\pm 100^{\circ}$C to 0°C is shown in Fig. 4.4(c-d).

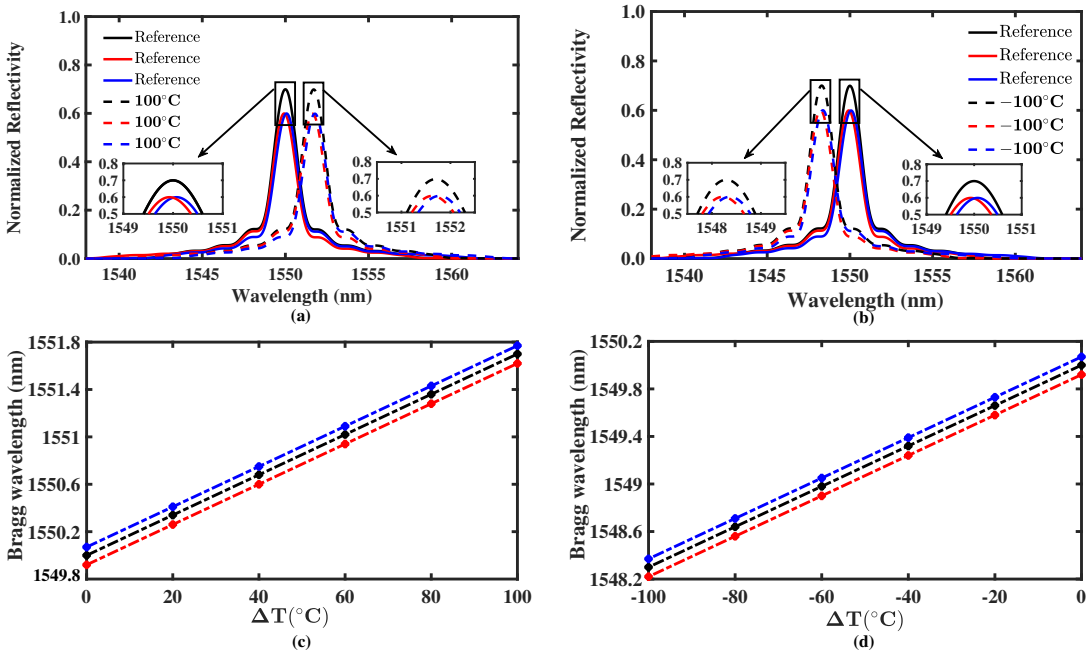

Figure 4.4: Effect of temperature on proposed structure(s): (a) complete spectrum shift in λ_B for $\Delta T = +100°\text{C}$ in a step of $+20°\text{C}$, (b) complete spectrum shift in λ_B for $\Delta T = -100°\text{C}$ in a step of $-20°\text{C}$, (c) estimated values of λ_B w.r.t ΔT for 0 to $100°\text{C}$ (d) estimated values of λ_B w.r.t ΔT for 0 to $-100°\text{C}$.

4.4 Conclusion

In this chapter, we have proposed a group of narrow-band optical bandpass filters operating on C-band. Here, we have used cascading of two apodized linearly chirped FBGs to get a narrow-band profile. Analytical formulation based on the PUA approach of the proposed cascaded structure(s) is incorporated. Also, we have used two apodization functions namely the Gaussian and Hyperbolic tangent functions to analyse the spectral profiles of the introduced structure(s). However, simulation results corroborating the analytical formulations are also presented. As per the simulations,the narrowest FWHM attained using both the apodization functions is recorded as 1.46 nm. But, the widest FWHM values are recorded as 1.66 nm and 1.76 nm for the proposed structure with Gaussian and Hyperbolic tangent

apodizations, respectively. The highest reflectivity of 0.812 and 0.699 are noted for Hyperbolic tangent and Gaussian apodized CFBGs, respectively. Further, the linear dependence of λ_B of the proposed structure with ΔT is incorporated. The thermal sensitivity of 17.02 pm/$^{\circ}$C was recorded forthe proposed structure(s).

Chapter 5

Performance Enhancement of Optical Communication System with Cascaded FBGs of Varying Lengths

5.1 Introduction

Nowadays, researchers are using cascaded FBG structures in optical communication systems to enhance its performance by reducing the spectral width of the laser source, thus reducing the dispersion [35, 155, 156, 159].Therefore, studying the spectral attributes of a cascaded FBG structure and its impact on the optical communication system is noteworthy. In this chapter, we have discussed the system-level integration of the designed cascaded FBG based device and its effect on the system's performance. Among all the optical devices proposed in chapters 2,3 and 4, the optical device introduced in chapter 2 has given a narrow FWHM. A narrow bandwidth of 0.07 nm corresponding to a reflectivity of 59.81 % with an SLSR of 89.41 dB has been achieved with the optical device introduced in chapter

2. Hence, we have used such a device to enhance the performance of the optical communication system. In particular, such a device has been kept immediately next to the optical source to reduce the source spectral width is discussed in this chapter.The effect of such a device on the system performance at various operating distances is discussed. Further, the system performance is studied with the apodized FBGs in the passive optical device. In the end, we had investigated the effect of incorporating the cascaded FBG structure in the system utilizing four-level pulse amplitude modulation or PAM-4 modulation . Section 5.2 describes the analytical formulation of the single uniform FBG structure and the proposed cascaded FBG structure. An optical communication system formed with a cascaded FBG structure of varying lengths to enhance the system performance is discussed in section 5.3. It also covers the dispersion compensation with the aid of an FBG in the system. Simulation results supported the analytical theory, and the suggested system is comprised in section 5.4. Finally, we have concluded the chapter in section 5.5.

5.2 Proposed Cascaded Uniform FBG Structure of Varying Lengths

As per the discussion we had in section 2.2.2, one can conclude that the proposed cascaded structure reduces the spectral width $\Delta\lambda$ of the optical pulse launched. However, the extent of pulse broadening ΔT usually termed as 'dispersion'in the fixed fiber length L_f depends on the spectral width of the pulse launched. The same can be confirmed using $\Delta T = DL_f\Delta\lambda$, where D is the dispersion parameter [165]. Hence, it is important to consider the effect of source spectral width on the system performance. As different spectral components of the pulse will receive the other end of the fiber at different time instants, the optical pulse launched gets broadened resulting in inter-symbol interference (ISI), thus reducing the performance of the system. Therefore, placing the proposed structure in the optical communication system reduces the spectral width of the pulse emanating from the source

and thus improves system performance which is evaluated in terms of BER and Q-factor discussed in the subsequent sections.

5.3 Optical Communication System with Proposed Cascaded FBG Structure

In this section, the proposed structure discussed in section 2.2 has been kept in the optical communication system to estimate its performance. The same can be verified by looking at Fig. 5.1. The blue solid or dotted lines indicate the electrical signal path while the green color refers to the optical signal path. The system consists of a transmitter, communication channel and receiver. The purpose of the optical transmitter is to convert the electrical signal into an optical signal. In this case, the launched optical pulses from the transmitter reached the receiver through a communication channel mentioned as optical fiber cable (OFC). The role of a receiver is to convert the received optical signal from the other end of the OFC into the original electrical signal.In Fig. 5.1, one can identify the transmitter components

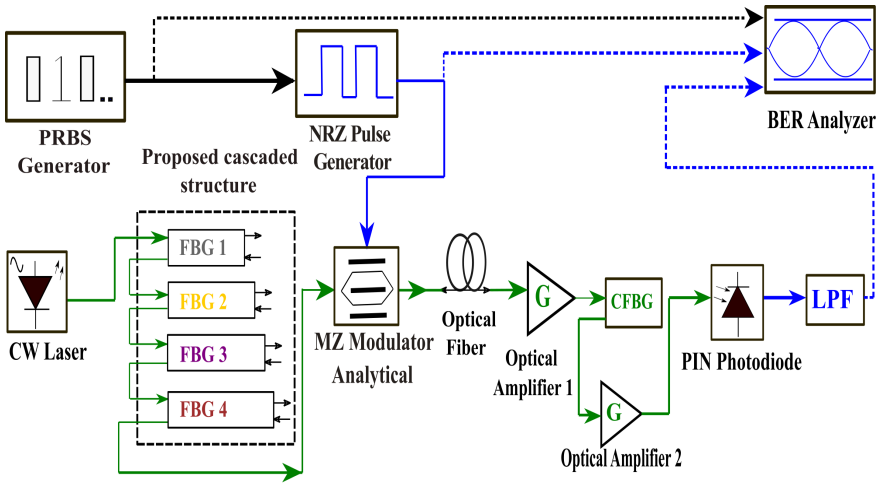

Figure 5.1: Performance enhancement of optical communication system with the proposed cascaded FBG structure.

as a pseudo-random bit sequence (PRBS) generator, CW laser, non-return to zero (NRZ)

pulse generator, proposed cascaded FBG structure, and a Mach-Zender (MZ) modulator. The output of a PRBS generator contains the sequence of ones and zeros emanating at a bit rate of 12.5 Gbps and is connected as an input to the NRZ pulse generator. The NRZ pulse generator is responsible for creating a sequence of non-return to zero electrical pulses that are coded by a digital signal format with a duty cycle of 0.5. The electrical pulses from the pulse generator are given as one of the two inputs of the MZ-modulator. Similarly, a continuous type output from a CW laser with a frequency of 193.41 THz (wavelength of 1550.00 nm) and power level of $+5$ dBm connected as an input to the proposed cascaded structure (particularly given as input signal to FBG 1). The proposed structure is responsible for reducing the spectral width of the source or the given input signal (as discussed in section 2.2.2). Hence, the reflected optical signal from FBG 4 of the proposed structure has reduced spectral width and is connected as an input to the other terminal of MZ-modulator. The extinction ratio of $+30$ dB of the modulator can perform the phase modulation. The phase-modulated output from the modulator reached the receiver through the OFC.

The L_f of the OFC for the constructed system has been considered as 105 km. Also, the attenuation offered and the dispersion parameter D of the fiber are taken as 0.2 dB$/$km and 16.75 ps$/$(km-nm), respectively. The optical signal travelled through the OFC cable must be amplified using an optical amplifier. Typically, the reason for using optical amplifiers is to compensate for the fiber losses for proper recovery of the signal at the receiver. Hence, erbium-doped fiber amplifiers (EDFAs) with a gain (G) of 10 dB and noise figure (NF) of 4.9 dB are used for the optical amplification purposes before and after the chirped fiber Bragg grating (CFBG). However,a CFBG of length 13 mm, linear chirp parameter of 1 nm$/$cm and Δn of 1×10^{-4} had been used as a dispersion compensation element in the system to enhance its performance. After the post-amplification of an optical signal from the CFBG, it is given to the receiver or Photodetector (PD). The used PD in the system is considered a PIN photodiode with a responsivity of 0.69 A$/$W and has a dark current of 10 nA. Using PD in the system is to convert the optical signal into an electrical signal. So, the electrical signal from a PIN is connected as an input to the low pass filter (LPF) of the

Bessel type with a cut-off frequency of 0.75 times the bit rate. Finally, the output from the LPF can be visualized using a BER analyzer. The keyparameters of the equipment used in the transmission system for the simulation are depicted in Table-5.1.

Table 5.1: Key parameters of the equipment used in the optical transmission system

Equipment/component	Parameter	Value
Uniform FBG	Grating length	10 mm
	Induced refractive index	0.0002
	Frequency	193.41 THz
	Effective refractive index	1.45
Apodized FBG	Gauss parameter	0.5
	Tanh Parameter	0.5
Chirped FBG	Chirp parameter	+1 nm/cm
	Effective refractive index	1.45
	Induced refractive index	0.0001
	Length of grating	13 mm
MZ-Modulator	Extinction ratio	+30 dB
	Symmentry factor	-1
	Insertion loss	3.28 dB
Single Mode Fiber	Attenuation	0.2 dB/km
	Dispersion	16.75 ps/(km-nm)
	Maximum operating length	105 km
EDFA	Gain	10 dB
	Noise figure	4.9 dB
PIN Photodetector	Responsivity	0.69 A/W
	Dark current	10 nA
Bessel LPF	Cutoff frequency	0.75$\times$ bitrate

5.3.1 Dispersion Compensation using FBG

To bare the parameters include insertion loss, non-linear effects and expensiveness, one can use FBGs for dispersion compensation purposes instead of dispersion compensation fiber

(DCF) [175, 193]. Particularly, a chirped FBG or CFBG can be used for dispersion compensation purposes [39, 194]. Generally, the grating pitch of a CFBG is not constant rather it is linearly varied as per the relation $\Lambda_N = \Lambda_1 + bz_N$, where b in terms of (nm/cm) represents the linear chirp parameter while N indicates the number of uniform FBG sections used to piecewise approximate the CFBG [35, 50, 160]. Λ_1, Λ_N are the grating pitch of the first and N^{th} uniform FBG section, respectively.In a linearly increased chirp (LIC) FBG, the low-frequency components of a pulse through the CFBG get delayed more due to the increasing optical pitch in the grating region. Such a LIC FBG provides an anomalous group velocity dispersion (GVD)and the same can be used to nullify the normal GVD. The dispersion parameter D_g of a LIC FBG of length L_g can be written as, $D_g = T_{Rt}/(L_g \times \Delta\lambda)$.Where T_{Rt} is the round trip time in the grating region of the fiber equals to $2n_{eff}L_g/c$, c is the velocity of light in vacuum, and $\Delta\lambda$ denotes the bandwidth of the CFBG [165].Therefore D_g can be reshaped and made equal to $2 \times n_{eff}/(c \times \Delta\lambda)$.

5.4 Simulation Results and Discussion

First we have constructed a cascaded FBG structure as shown in Fig. 2.2 and observed its spectral characteristics using MATLAB® R2021a as depicted in Fig. 2.3. Next, we have kept the same proposed structure in an optical communication system to reduce the spectral width of the source. The performance of the system in terms of BER, Q-factor, and eye height is visualised using OptiSystem™ 18 software.In this work, each FBG of a cascaded structure is built on SMF-28 fiber and the design parameters for the proposed cascaded structure and the system are considered as per the earlier discussion in sections 2 and 3, respectively. In Fig. 5.2 and Fig. 5.3, black and pink colors are designated to estimate the performance of the system without and with the proposed structure, respectively. It is evident from Fig. 5.2(a) that the system operated on C-band (1530 -1565 nm) at abit rate of 12.5 Gbps with L_f of 105 km has given us a maximum Q-factor of 6.398 without the

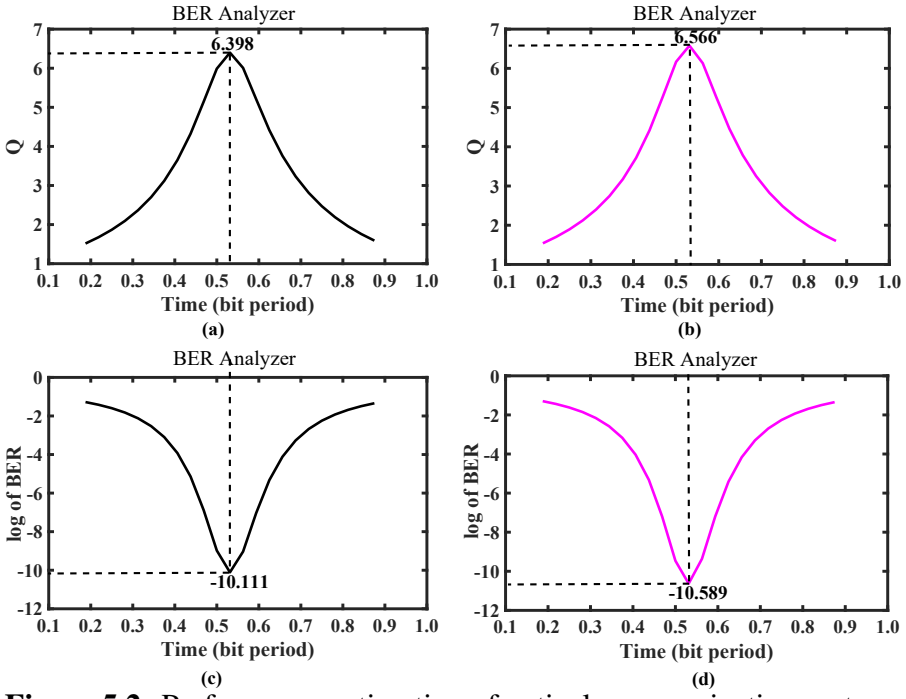

Figure 5.2: Performance estimation of optical communication system: (a) Q-factor without cascaded structure. (b) Q-factor with cascaded structure. (c) Logarithm value of BER without cascaded structure. (d) Logarithm value of BER with cascaded structure.

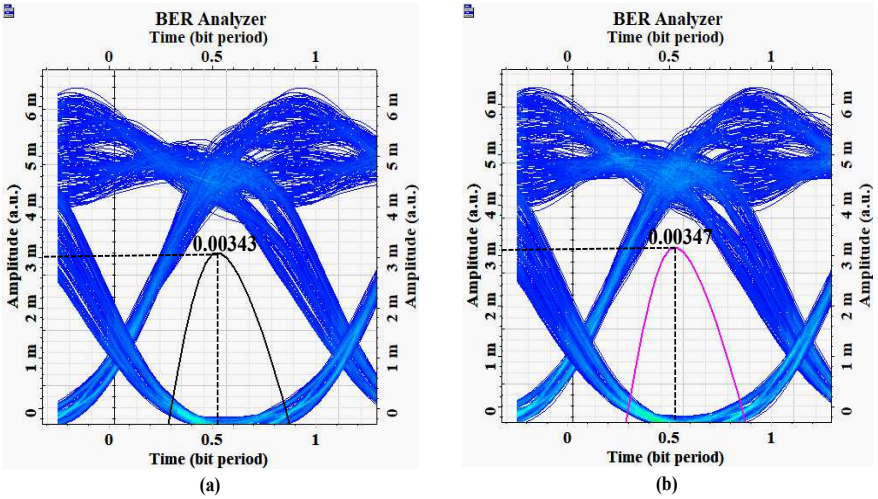

Figure 5.3: A model of eye diagram analysis with regard to eye height at L_f of 80 km: (a) without cascaded (b) with cascaded structure.

proposed structure. The corresponding minimum BER for this particular case is recorded as 7.7358×10^{-11} and one can verify the same using Fig. 5.2(c). The value of BER attained

using Q-factor can be made equal to $0.5\text{erfc}(\text{Q}/\sqrt{2})$[195, 196].

Apart from the Q-factor and BER, the performance of the system is analysed in terms of eye height which reflects the quality of the signal is noted as 0.00069 a.u. in the absence of the cascaded structure. As shown in Fig. 5.2(b), the value of Q attained with the proposed structure in the system can be marked as 6.566. Similarly, the corresponding value of BER for this case has resulted as 2.5713×10^{-11}. An eye height of 0.00071 a.u. is being noted for this case. Hence, it is evident from the above discussion that the values like Q-factor, BER and eye height achieved with the proposed cascaded structure are better than compared to without the presence of cascaded structure in the system.

In the preceding discussion we have considered the L_f as 105 km for the system and the proposed system can be used for WDM applications. Now, we are varying the L_f and keeping all the design parameters same for the system shown in Fig. 5.1 to check its performance. It has been observed from the Table-5.2 that as the L_f changes from 60 km to 130 km, the value of Q decreases from 26.758 to 02.401 and from 27.344 to 02.426 in the absence and presence of a cascaded structure, respectively. As we already know that decrease in a Q affects the increase in the BER value. Accordingly, the value of BER changes from 0 to 8.1564×10^{-03} and 0 to 7.4628×10^{-03} for without and with the presence of the cascaded structure, respectively.Similarly, the eye height decreases from 0.01088 a.u.

Table 5.2: Performance Estimation of the System with uniform FBGs in the structure for Different Lengths of the Fiber

L_f	**Q-factor**		**BER**		**Eye Height (a.u.)**	
(km)	Without cascaded structure	With cascaded structure	Without cascaded structure	With cascaded structure	Without cascaded structure	With cascaded structure
60	26.758	27.344	0	0	0.01088	0.01090
70	18.923	19.921	0	0	0.00634	0.00639
80	11.824	12.330	0	0	0.00343	0.00347
90	10.474	10.682	0	0	0.00194	0.00195
100	07.513	07.530	2.8540×10^{-13}	2.5039×10^{-14}	0.00096	0.00097
110	05.429	05.479	2.8252×10^{-08}	2.1237×10^{-08}	0.00041	0.00042
120	03.607	03.673	1.5434×10^{-04}	1.1893×10^{-04}	0.00009	0.00010
130	02.401	02.426	8.1564×10^{-03}	7.4628×10^{-03}	-0.00007	-0.00006

to -0.00007 a.u. and from 0.01090 a.u. to -0.00006 a.u. for the absence and presence of the cascaded structure respectively. Hence it is emphasized from the discussion that the performance of the system is degraded as the L_f increases. It is also important to note that one cannot use the system at distances greater than 105 km for WDM applications as the maximum Q becomes smaller than 6.00 and the minimum BER will go with greater than 10^{-9}. As a result, this is the maximum distance that can be covered while maintaining adequate Q and BER. In addition to the Q and BER estimation, a simulated model of an eye-diagram analysis regarding the eye height is shown in Fig. 5.3. It is observed from Fig. 5.3(a) that in the absence of cascaded structure one can get the eye height as 3.43×10^{-3} a.u. at L_f of 80 km. Likewise, in the presence of a cascaded structure, we can achieve an eye height of 3.47×10^{-3} a.u. which is better in value than compared to without the presence of the cascaded structure is shown in Fig. 5.3(b).

5.4.1 Performance Estimation of the System with the Apodized FBGs in the Structure

In the earlier discussion one can note that the performance of the system is improved with the cascaded structure. Further improvement in the system performance can be attained with the aid of apodized FBGs in the cascaded structure and the same can be observed by looking at the performance metrics of the system from Table-5.3 and Table-5.4, respectively. Here, we have considered two different functions for the apodization of FBGs, namely the Gaussian and hyperbolic tangent [163, 197, 198]. To get the optimum response of the system the value of Gauss and tanh parameters are considered as 0.5. Therefore, it is evident from Table-5.3 and Table-5.4 that the value of Q changes from 27.361 to 02.471 for Gaussian apodized FBGs whereas the value of Q switches from 27.372 to 02.485 for hyperbolic tangent apodized FBGs in the structure. The corresponding BER values vary from 0 to 6.5721×10^{-03} for the case of Gaussian apodized FBGs while the values are altered from 0 to 6.3781×10^{-03} for hyper tangent apodized FBGs. An eye height variation

from 0.01091 a.u to 0.00043 a.u. and from 0.01092 a.u. to 0.00044 a.u are being observed up to a distance 110 km for the Gaussian and tanh apodized FBGs, respectively. But, there is no further enhancement in eye height beyond the distance of 110 km compared to uniform FBGs in the structure.However, at the maximum operating distance (i.e., 105 km) the values

Table 5.3: Performance Estimation of the System with Gaussian apodized FBGs in the structure for Different Lengths of the Fiber

L_f	**Q-factor**		**BER**		**Eye Height (a.u.)**	
(km)	Without cascaded structure	With cascaded structure	Without cascaded structure	With cascaded structure	Without cascaded structure	With cascaded structure
60	26.758	27.361	0	0	0.01088	0.01091
70	18.923	19.958	0	0	0.00634	0.00640
80	11.824	12.341	0	0	0.00343	0.00348
90	10.474	10.691	0	0	0.00194	0.00196
100	07.513	07.536	2.8540×10^{-13}	2.4017×10^{-14}	0.00096	0.00098
110	05.429	05.484	2.8252×10^{-08}	2.0813×10^{-08}	0.00041	0.00043
120	03.607	03.681	1.5434×10^{-04}	1.1584×10^{-04}	0.00009	0.00011
130	02.401	02.471	8.1564×10^{-03}	6.5721×10^{-03}	-0.00007	-0.00006

Table 5.4: Performance Estimation of the System with Hyperbolic Tangent apodized FBGs in the structure for Different Lengths of the Fiber

L_f	**Q-factor**		**BER**		**Eye Height (a.u.)**	
(km)	Without cascaded structure	With cascaded structure	Without cascaded structure	With cascaded structure	Without cascaded structure	With cascaded structure
60	26.758	27.372	0	0	0.01088	0.01092
70	18.923	19.972	0	0	0.00634	0.00641
80	11.824	12.348	0	0	0.00343	0.00349
90	10.474	10.699	0	0	0.00194	0.00197
100	07.513	07.687	2.8540×10^{-13}	7.4539×10^{-15}	0.00096	0.00099
110	05.429	05.487	2.8252×10^{-08}	2.0292×10^{-08}	0.00041	0.00044
120	03.607	03.686	1.5434×10^{-04}	1.0411×10^{-04}	0.00009	0.00011
130	02.401	02.485	8.1564×10^{-03}	6.3781×10^{-03}	-0.00007	-0.00006

of Q are obtained as 06.601 and 06.712 for Gaussian and hyperbolic tangent apodized FBGs, respectively. The related values of BER are being noted as 2.0281×10^{-11} and 9.5321×10^{-12}. Similarly, the values of eye height for Gaussian and hyperbolic tangent apodized FBGs resulted in 0.00072 a.u. and 0.00073 a.u. respectively.Hence, it is deduced from the above discussion that Gaussian and hyperbolic tangent apodized FBGs have given a better performance than compared to the uniform and without FBGs in the structure. In particular, hyperbolic tangent apodized FBGs given better performance compared to the

Gaussian apodized FBGs in the structure and the same can be confirmed from Table-5.5.On

Table 5.5: Performance estimation of the system with single and cascaded FBG structure at the maximum operating distance

Cascaded FBG structure	**Length of FBG (mm)**	**Q-factor**	**BER**
Absence of proposed structure	-	**06.398**	$\mathbf{7.7358 \times 10^{-11}}$
Single uniform FBG	10	06.410	7.2291×10^{-11}
	11	06.440	5.9351×10^{-11}
	12	06.470	4.8685×10^{-11}
Presence of proposed structure with uniform FBGs	varying lengths	**06.566**	$\mathbf{2.5713 \times 10^{-11}}$
Single Gaussian apodized FBG	10	06.501	3.9634×10^{-11}
	11	06.530	3.2668×10^{-11}
	12	06.545	2.9551×10^{-11}
Presence of proposed structure with Gaussian apodized FBGs	varying lengths	**06.601**	$\mathbf{2.0281 \times 10^{-11}}$
Single Hyperbolic Tangent apodized FBG	10	06.570	2.4991×10^{-11}
	11	06.585	2.2592×10^{-11}
	12	06.600	2.0420×10^{-11}
Presence of proposed structure with Hyperbolic Tangent apodized FBGs	varying lengths	**06.712**	$\mathbf{9.5321 \times 10^{-12}}$

the other hand, as the length of the single FBG changes from 10 mm to 12 mm (depicted in Table-5.5), the value of Q alters from 06.410 to 06.470 for the case of uniform FBGs, whereas the value of Q switches from 06.501 to 06.545 for Gaussian apodized FBGs. The corresponding BER values vary from 7.2291×10^{-11} to 4.8685×10^{-11} for the case of uniform FBGs while the values are changes from 3.9634×10^{-11} to 2.9551×10^{-11} for Gaussian apodized FBGs.Similarly, the values of Q for a single hyperbolic tangent apodized FBG in the system vary from 06.570 to 06.600, and the corresponding BERs are altered from 2.4991×10^{-11} to 2.0420×10^{-11}. However, with the proposed structure, the value of Q has been improved to 06.566 and 06.601 for uniform and Gaussian apodized FBGs of varying lengths (lengths are varied as discussed in section 2.2.2, with the first FBG of length

10 mm). In contrast, the value Q for hyperbolic tangent apodized FBGs of varying lengths in the structure is recorded as 06.712. The corresponding values of BER are recorded as 2.5713×10^{-11} and 2.0281×10^{-11} for uniform and Gaussian apodized FBGs, whereas the value of BER for hyperbolic tangent apodized FBGs is achieved as 9.5321×10^{-12} . Hence, one can confirm from the above discussion that the presence of a cascaded uniform FBG structure has given better performance than the single uniform FBGs of varying lengths in the system. The same is true for the proposed structure with Gaussian and Hyperbolic tangent apodized FBGs.

5.4.2 Performance Test of the System with Multilevel Modulation Format

So far, we have used the NRZ modulation format and the cascaded FBG structure in the proposed system to transmit data over the fiber. The performance of the proposed system has also been tested for multilevel modulation format. In this case we have used 4-level pulse amplitude modulation (PAM-4). Usually, such a modulation format doubles the data rate of the system compared to the NRZ modulation format and one does not need any expensive coherent optical receiver to detect the signal. Hence such a modulation format can be used for data center applications to increase the serial line rate of the NRZ link. However, the generation of such an optical PAM-4 signal using two NRZ signals is demonstrated in [199]. Here, we have initially checked the system's performance without a cascaded structure using PAM-4 modulation for different data rates and fiber lengths. Later we used a cascaded FBG structure in the system to reduce the source spectral width, thereby enhancing the system performance is checked. After that, we studied the system's performance by considering different apodized FBGs in the cascaded structure. It is evident from Fig. 5.4 that as the data rate increases from 5 Gbps to 40 Gbps, the BER getting increases for different L_f's (1 km, 5 km, 10 km, 20 km, and 25 km) of the OFC. Therefore the opening of the eye is getting reduced. The red line in each eye diagram indicates the minimum BER curve.An

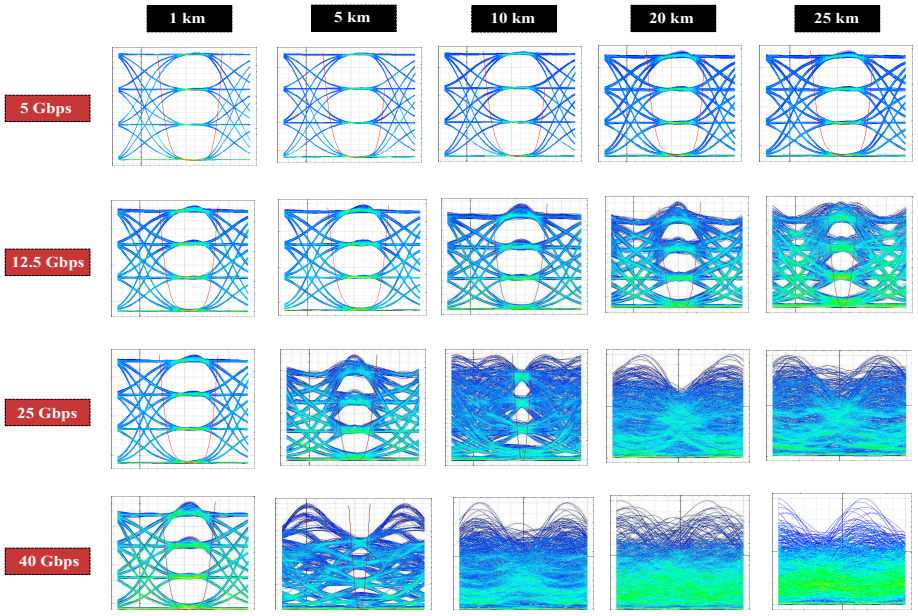

Figure 5.4: Eye diagram analysis using PAM-4 modulation format for different data rates of the proposed system in the absence of the cascaded structure.

improvement in the system performance in terms of BER achieved with the cascaded FBG structure in the system is depicted in Fig. 5.5. Compared with Fig. 5.4, Fig. 5.5 has given us better eye diagram. Therefore one can say that the proposed system also supports the multilevel modulation format. Similarly,as we already know that apodized FBG will give us better performance than the normal or uniform FBG. Hence we have considered Gaussian and hyperbolic tangent apodized FBGs in the cascaded structure and used them along with PAM-4. It can be demonstrated from Fig. 5.6 and Fig. 5.7 that the system has given improved performance in terms of BER or opening of an eye for the Gaussian and hyperbolic tangent apodized FBGs compared to without or with uniform FBGs in the structure. In particular, hyperbolic tangent apodized FBGs in the structure have given us better performance than all the cases we discussed earlier.

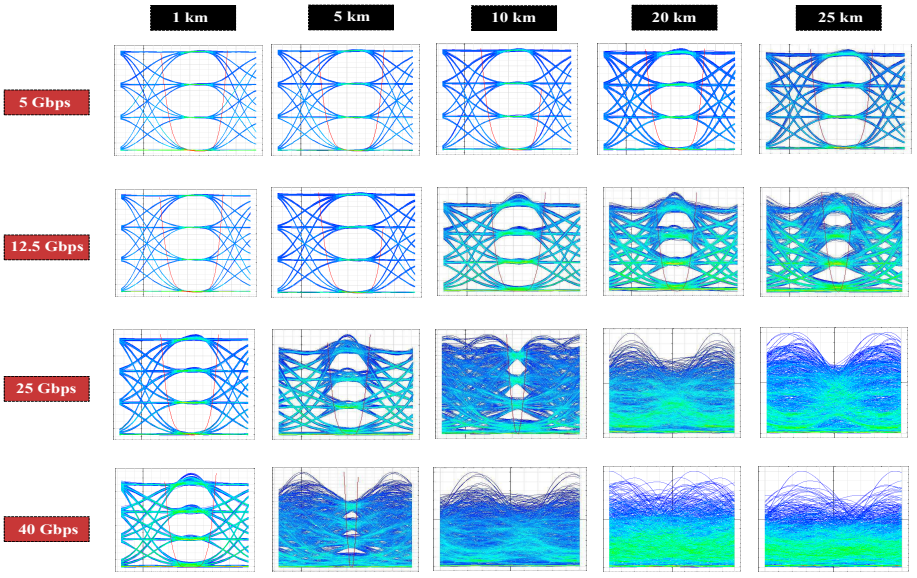

Figure 5.5: Eye diagram analysis using PAM-4 modulation format for different data rates of the proposed system in the presence of the cascaded structure.

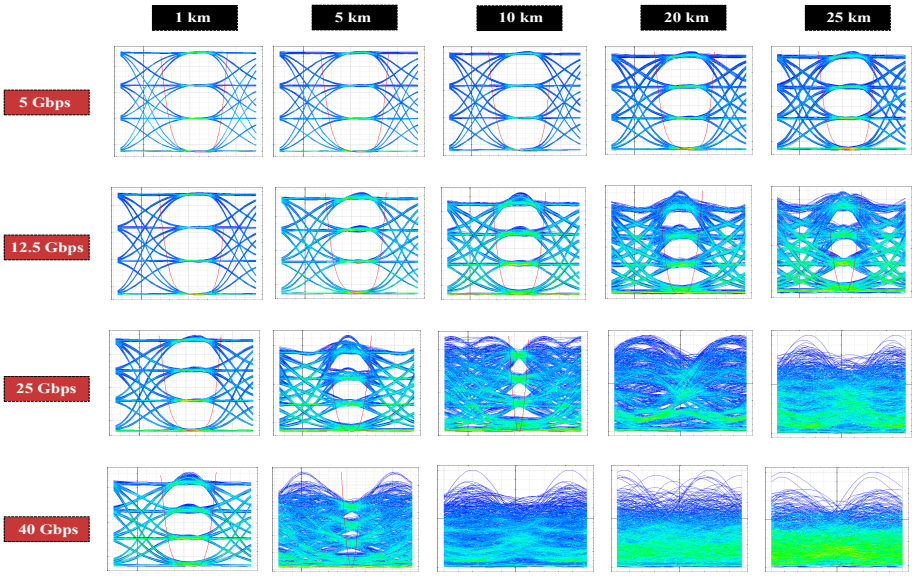

Figure 5.6: Effect of system performance for different data rates by considering Gaussian apodized FBGs in the cascaded structure along with PAM-4 modulation format.

5.4.3 Comparative Study

A comparative study of various recently reported cascaded structures and their performances on the optical transmission systems with the present work is reported in Table-5.6. In all

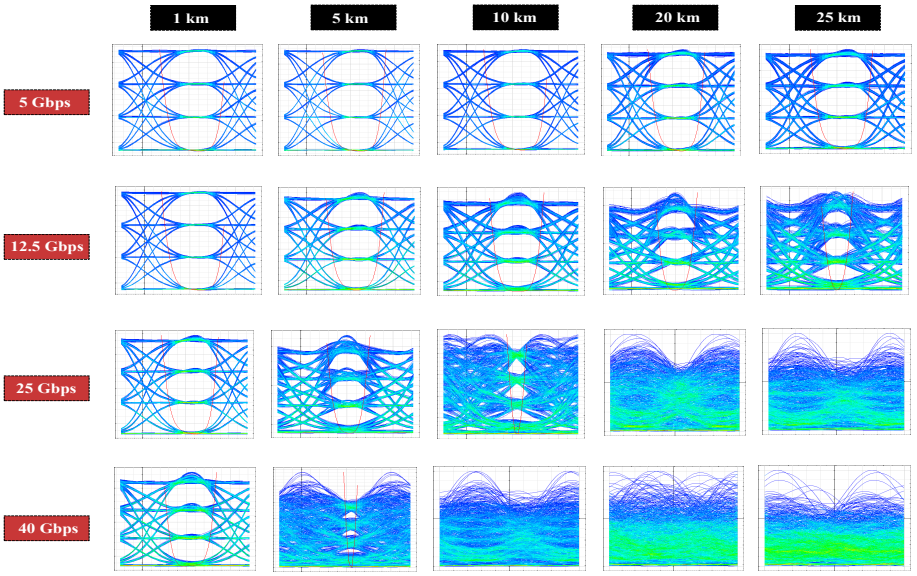

Figure 5.7: Effect of system performance for different data rates by considering hyperbolic tangent apodized FBGs in the cascaded structure along with PAM-4 modulation format.

the listed cascaded structures [154, 155, 157, 158], authors used the same type and same length of FBGs except the one presented in [160]. In the present work, we have used the same type of FBGs in the structure with varying lengths and tested its performance in the optical link. The reason for using a varying length cascaded structure over the same length structure is discussed in chapter 2.It is evident from the table that the presented cascaded structure with four uniform FBGs [154] of the same type and same length has given an FWHM of 0.160 nm. However, this value has been improved to 0.008 nm with the apodized FBGs in the structure.Similarly, a cascaded structure formed using Cauchy's apodized FBGs has given us an FWHM of 0.102 nm [155]. This structure has been used to reduce the source spectral width of the optical link, which is operated at a bit rate of 10 Gbps and tested up to 100 km and has given a minimum BER of 4.24×10^{-10} at 30 km. To improve the performance by reducing the chromatic dispersion of an optical link of 100 km, a cascaded Hyperbolic tangent apodized FBG structure of the same lengths in symmetrical compensation mode along with the modified duobinary modulation scheme is introduced in [157]. The introduced transmission system is tested at a bit rate of 10 Gbps and has given a BER of 8.44×10^{-11}. Further improvement in the BER to 2.59×10^{-13}

can be achieved using four identical types of LIC FBGs of the same lengths used in 70 km link operated with a bit rate of 10 Gbps along with the differential phase shift keying or DPSK modulation is presented in [158]. However, a cascaded CFBG structure formed with one linearly increased chirp (LIC) and one linearly decreased chirp (LDC) FBGs has given an FWHM of 1.56 nm is mentioned in [160]. On the other hand, a proposed four-stage cascaded FBG structure formed with hyperbolic tangent apodized FBGs has given better spectral characteristics (narrow FWHM of 0.07 nm and SLSR of 89.41 dB) than the structures in [154, 155, 157, 158] is listed in the table as present work. The structure's performance is tested on a 105 km optical link operated at a bit rate of 12.5 Gbps, giving a BER of 9.53×10^{-12}. Therefore, one can deduce from the above discussion that the introduced optical system with the proposed structure can carry more information over a longer distance than the existing systems with acceptable BER (generally considered less than 10^{-9} for telecommunications).

Table 5.6: Performance comparisonof recently reported cascaded structures on the optical transmission system

Year	Ref.	Type of FBG	Number of FBGs cascaded	FWHM (nm)	SLSR (dB)	Bit rate (Gbps)	L_f (km)	BER
2019	[154]	Uniform	04	0.160	-	-	-	-
2021	[155]	Cauchys apodized	04	0.102	-	10	100	4.24×10^{-10}
2022	[157]	Hyperbolic Tangent apodized	04	-	-	10	100	8.44×10^{-11}
2022	[158]	LIC FBGs	04	-	-	10	70	2.59×10^{-13}
2022	[160]	LIC and LDC FBGs	02	1.56	-	-	-	-
2023	Present work	Hyperbolic Tangent apodized (Varying lengths)	04	0.07	89.41	12.5	105	9.53×10^{-12}

5.5 Conclusion

In this chapter, we have proposed an optical communication system formed with a passive optical device operating in the C-band. The optical device constructed using four cascaded

FBGs of varying lengths is demonstrated. Simulation results corroborating the analytical formulation are included. Simulation results confirm that in the presence of the optical device, the system performance (in terms of Q-factor, BER, and eye height) has been increased compared to the absence of the device. As per the simulation results, the proposed device has given a maximum reflectivity and minimum FWHM of 98.39% and 0.175 nm for uniform FBGs, respectively. But with the apodized FBGs, an FWHM of 0.07 nm with a reflectivity of 59.81% has been achieved. Also, at the maximum operating distance of the system with apodized FBGs, the Q-factor and bit error rate (BER) are recorded as 6.712 and 9.5321×10^{-12}, respectively. Based on the simulated findings, one can infer that the system formed with a cascaded structure also supports the PAM-4 modulation for short-distance applications. Furthermore, a comparative study of the system performance for various operating distances with uniform and apodized FBGs in the optical device is furnished. Based on such a study, we found that hyperbolic tangent apodized FBGs in the structure have given us better performance than uniform and Gaussian apodized FBGs.

Chapter 6

Conclusion and Future Work

6.1 Conclusion

In this thesis, the design, analysis, and simulation of various cascaded FBG based structures operated on the C-band are proposed for the performance enhancement of the optical transmission system for long-haul communications.Initially, a cascaded uniform FBG structure of varying lengths operated on the C-band has been proposed. A suitable analytical formulation for such a structure has been included. Such a proposed structure has given a maximum reflectivity of 98.39 $\%$ corresponding to the FWHM of 0.175 nm with an SLSR of 45.76 dB. However, for better spectral characteristics in terms of FWHM and SLSR, an apodized cascaded FBG structure of varying lengths operated on the C-band has been introduced. The proposed device can attain an FWHM of 0.08 nm corresponding to a reflectivity of 55.95$\%$ with an SLSR of 87.38 dB with the Gaussian apodization. One can note that the further improvement in FWHM or a narrow bandwidth of 0.07 nm corresponding to a reflectivity 59.81 $\%$ with SLSR of 89.41 dB has been achieved with the Hyperbolic tangent apodized FBGs in the structure.

Next, we have proposed a cascaded CFBG-based structure operating in the C-band. A suitable analytical formulation based on a piecewise uniform approach (PUA) for the proposed structure(s) is also incorporated in this thesis. Cascading one LIC-FBG with another LDC-FBG will result in the narrowest and widest FWHMs being 1.56 nm and 1.77 nm, respectively. With the proposed cascaded CFBG structures, the highest and lowest reflectivity achieved is approximately 0.81 and 0.39, respectively. The effect of temperature on the spectral characteristics of proposed structures is also studied. Simulation results reveal that λ_B of the proposed cascaded structures have a linear dependence on ΔT.Finally, we have proposed and analyzed a cascaded apodized CFBG-based structure operating in the C-band. Here, we have used cascading of two apodized linearly chirped FBGs (one is linearly increased chirp while the other is linearly decreased chirp)to get a narrow-band profile. The narrowest FWHM attained using both the apodization functions is recorded as 1.46 nm. But, the widest FWHM values are recorded as 1.66 nm and 1.76 nm for the proposed structure with Gaussian and Hyperbolic tangent apodizations, respectively. The highest reflectivity of 0.812 and 0.699 are noted for Hyperbolic tangent, and Gaussian apodized CFBGs, respectively. Based on the above discussion, one cancompare that the apodized CFBGs have given narrower FWHM than normal CFBGs. Also, the effect of temperature on the proposed devices reveals that λ_B has a linear dependence on ΔT.

Among all the optical devices proposed, the optical device presented with apodized FBGs has better spectral characteristics than others. Hence, such a cascaded structure has been used in the optical communication system immediately next to the source to reduce the source spectral spectra width, thus enhancing the performance by reducing the dispersion in the fiber. Simulation results confirm that in the presence of the optical device, the system performance (in terms of Q-factor, BER, and eye height) has been increased compared to the absence of the device. Also, at the maximum operating distance (i.e., 105 km) of the system with Hyperbolic tangent apodized FBGs, the Q-factor and bit error rate (BER) is recorded as 6.712 and 9.5321×10^{-12}, respectively. Based on the simulated findings, one can infer

that the system formed with a cascaded structure also supports the PAM-4 modulation for short-distance applications.

The primary contribution of this thesis is the design and analysis of various cascaded FBG or CFBG-based structures with better spectral characteristics operated on the C-band for communication or sensing purposes as follows,

- To enhance the performance of the optical transmission system, the source spectral width of a pulse, which is proportional to the dispersion in the fiber, has been reduced in this thesis using various cascaded FBG structures.
- A cascaded FBG structure designed using hyperbolic tangent apodized FBGs of varying lengths has given better spectral characteristics. The introduced device can provide a FWHM of 0.07 nm with an SLSR of 87.38 dB.
- A cascaded CFBG structure has been designed and analyzed using a piecewise uniform approach with two linearly chirped FBGs (One is of linearly increased chirp while the other is of linearly decreased chirp) for narrow-band bandpass filtering purposes.
- The designed cascaded structure with hyperbolic tangent apodized FBGs has been integrated with the optical transmission system to enhance its performance by reducing the dispersion in the fiber for long-haul communications.
- The designed cascaded structures can be used for sensing purposes to measure various operating temperatures.

6.2 Future Work

This thesis presents the design and analysis of cascaded FBG-assisted optical devices. This work complements the research and development activities in the field of fiber optic communications and FBG-based sensing. Here are some possible extensions of this thesis work

that can be looked into for future research endeavors;

- One can use multi-channel optical communication systems to achieve higher data transmission capacity and increased network efficiency. Hence, studying the performance of the multi-channel system using cascaded FBG structures is one of the future aspects.
- In this work, cascaded FBG based devices are constructed using single-mode fibers. As multi-mode systems offer a lower cost for short-range, high-speed communications, creating cascaded FBG based devices using multi-mode fiber presents an avenue for future work.
- Apodized FBGs can be used to get narrower FWHM with reduced strength of side lobes in the reflection spectrum. In this work, Gaussian and Hyperbolic tangent apodized FBGs are considered for optimizing FBGs in the cascaded structures. Other apodization functions can also be considered for future work.
- Since the proposed devices can be used for communication and sensing purposes, an increase in the thermal sensitivity of the cascaded device can be done using coated materials on each FBG of the cascaded structure. Such a coated cascaded FBG device will present an avenue for future FBG-based sensing devices. As an example, to enhance the sensitivity, metal coated FBGs can be used for the application of surface plasmon effect in grating assisted FBGs.
- To enhance the optical transmission system performance for long-haul communications advanced modulation formats can be used along with the cascaded FBG structures.
- In addition to the various FBGs considered for the cascaded FBG structures, other types of FBGs such as phase-shifted FBGs and tilted FBGs, can also be considered.

- The integration of deep learning techniques with cascaded Fiber Bragg Grating (FBG) structurescan be used for sensing purposes.

Bibliography

[1] Norbert Kaplan, Jozef Jasenek, Jozefa Červeňová, and MarianaUšáková. Magnetic optical fbg sensors using optical frequency-domainreflectometry. *IEEE Transactions on Magnetics*, 55(1):–4, 2018.

[2] Danqing Yang, Yinggang Liu, Yuxi Wang, Ting Zhang, Min Shao, Dakuan Yu, HaiweiFu, and Zhenan Jia. Integrated optic-fiber sensor based on enclosed efpi and structuralphase-shift for discriminating measurement of temperature, pressure and ri. *Optics & Laser Technology*, 126:106112, 2020.

[3] Khong Nee Koo, Ahmad Fauzi Ismail, Mohd Hafiz Dzarfan Othman, Alireza Samavati,Zhong Sheng Tai, Mukhlis A Rahman, Hazri Bakhtiar, and Muhammad Aizi Mat. Fabrication and modification of temperature fbg sensor: role ofoptical fiber type and cu sputtered thickness. *Physica Scripta*, 95(9):095509, 2020.

[4] G Meltz, W_W Morey, and WH Glenn. Formation of bragg gratings in optical fibers by a transverseholographic method. *Optics letters*, 14(15):823–825, 1989.

[5] Kenneth O Hill and Gerald Meltz. Fiber bragg grating technology fundamentals and overview. *Journal of lightwave technology*, 15(8):–1276, 1997.

[6] Graham D Marshall, Robert J Williams, Nemanja Jovanovic, MJ Steel, andMichael J Withford. Point-by-point written fiber-bragg gratings and their application incomplex grating designs. *Optics express*, 18(19):19844–19859, 2010.

[7] Jiqiang Wang, Lin Zhao, Tongyu Liu, Zhen Li, Tong Sun, and Kenneth TV Grattan. Novel negative pressure wave-based pipeline leak detection systemusing fiber bragg grating-based pressure sensors. *Journal of Lightwave Technology*, 35(16):–3373, 2016.

[8] Jiajian Wang, Liang Ren, Tao Jiang, Ziguang Jia, and Guo-xin Wang. A novel gas pipeline burst detection and localization method based onthe fbg caliber-based sensor array. *Measurement*, 151:107226, 2020.

[9] Yinggang Liu, Danqing Yang, Yuxi Wang, Ting Zhang, Min Shao, Dakuan Yu, HaiweiFu, and Zhenan Jia. Fabrication of dual-parameter fiber-optic sensor by cascading fbgwith fpi for simultaneous measurement of temperature and gas pressure. *Optics Communications*, 443:166–171,2019.

[10] Arnaldo G Leal-Junior, Carlos Marques, Anselmo Frizera, and Maria Jose Pontes. Multi-interface level in oil tanks and applications of optical fibersensors. *Optical Fiber Technology*, 40:82–92, 2018.

[11] Mohd Raffi Samsudin, Yu Gang Shee, Faisal Rafiq Mahamd Adikan, BushroaBinti Abdul Razak, and Mahidzal Dahari. Fiber bragg gratings hydrogen sensor for monitoring the degradationof transformer oil. *IEEE Sensors Journal*, 16 (9):2993–2999,2016.

[12] Zhenwei Zhou, Chunfeng Wan, Da Fang, Liyu Xie, Hesheng Tang, Caiqian Yang,Youliang Ding, and Songtao Xue. Quasi-static macrostrain-based structural damage detection withdistributed long-gauge fiber bragg grating sensing. *Journal of Intelligent Material Systems and Structures*,31(18):2137–2151, 2020.

[13] António Barrias, Joan R Casas, and Sergi Villalba. A review of distributed optical fiber sensors for civil engineeringapplications. *Sensors*, 16(5):748, 2016.

[14] Natalia Reggiani Manzo, Gabriel T Callado, Cristiano MB Cordeiro, and LuizCarlos M Vieira Jr. Embedding optical fiber bragg grating (fbg) sensors in 3d printedcasings. *Optical Fiber Technology*, 53:102015, 2019.

[15] Zhi Zhou and Jinping Ou. Development of fbg sensors for structural health monitoring in civilinfrastructures. pages 197–207, 2005.

[16] V Dewynter-Marty, P Ferdinand, E Bocherens, R Carbone, H Beranger,S Bourasseau, M Dupont, and D Balageas. Embedded fiber bragg grating sensors for industrial composite curemonitoring. *Journal of intelligent material systems and structures*,9(10):785–787, 1998.

[17] Alex Dante, Rodrigo Moreira Bacurau, Anderson Wedderhoff Spengler,Elnatan Chagas Ferreira, and José Antônio Siqueira Dias. A temperature-independent interrogation technique for fbg sensorsusing monolithic multilayer piezoelectric actuators. *IEEE Transactions on Instrumentation and Measurement*,65(11):2476–2484, 2016.

[18] Vivekanand Mishra, Mukesh Lohar, and Angela Amphawan. Improvement in temperature sensitivity of fbg by coating of differentmaterials. *Optik*, 127(2):825–828, 2016.

[19] Valmir De Oliveira, Marcia Muller, and Hypolito José Kalinowski. Bragg gratings in standard nonhydrogenated fibers forhigh-temperature sensing. *Applied Optics*, 50 (25):E55–E58, 2011.

[20] Katerina Krebber, Wolfgang Habel, Toivo Gutmann, and C Schram. Fiber bragg grating sensors for monitoring of wind turbine blades. In *17th International Conference on Optical Fibre Sensors*,volume 5855, pages 1036–1039. International Society for Optics andPhotonics, 2005.

[21] Hyung-Joon Bang, Hong-Il Kim, and Kang-Su Lee. Measurement of strain and bending deflection of a wind turbine towerusing arrayed fbg sensors. *International journal of precision engineering andmanufacturing*, 13(12):2121–2126, 2012.

[22] K Bremer, E Lewis, G Leen, B Moss, S Lochmann, I Mueller, Thomas Reinsch, andJörg Schrötter. Fibre optic pressure and temperature sensor for geothermal wells. In *SENSORS, 2010 IEEE*, pages 538–541. IEEE, 2010.

[23] Chi-wen Yu, Shih-chang Lei, Wen-shan Chen, and Sheng-rong Song. Downhole fiber optic temperature-pressure innovative measuring systemused in sanshing geothermal test site. *Geothermics*, 74:190–196, 2018.

[24] Daniele Tosi, Sven Poeggel, Iulian Iordachita, and Emiliano Schena. Fiber optic sensors for biomedical applications. In *Opto-Mechanical Fiber Optic Sensors*, pages 301–333.Elsevier, 2018.

[25] Giovanna Palumbo, Daniele Tosi, Agostino Iadicicco, and Stefania Campopiano. Analysis and design of chirped fiber bragg grating for temperaturesensing for possible biomedical applications. *IEEE Photonics Journal*, 10(3):1–15, 2018.

[26] Hani Hareiza Abd Raziff, Daryl Tan, Kok-Sing Lim, Chai Hong Yeong, Yin How-Wong, Basri Johan Jeet Abdullah, Norshazriman Sulaiman, and Harith Ahmad. A temperature-controlled laser hot needle with grating sensor forliver tissue tract ablation. *IEEE Transactions on Instrumentation and Measurement*, 2020.

[27] L D'Acquisto, F Scardulla, and S Pasta. Steam sterilization processes affect the stability of clinicalthermometers: Thermistor and prototypal fbg probe comparison. *Optical Fiber Technology*, 55:102156, 2020.

[28] Sidney Goossens, Ben De Pauw, Thomas Geernaert, Mohammad Saleh Salmanpour,Zahra Sharif Khodaei, Evangelos Karachalios, Diego Saenz-Castillo, HugoThienpont, and Francis Berghmans. Aerospace-grade surface mounted optical fibre strain sensor forstructural health monitoring on composite structures evaluated againstin-flight conditions. *Smart Materials and Structures*, 28(6):, 2019.

[29] Matthew J Nicolas, Rani W Sullivan, and W Lance Richards.Large scale applications using fbg sensors: determination ofin-flight loads and shape of a composite aircraft wing.*Aerospace*, 3(3):18, 2016.

[30] Raffaella Di Sante.Fibre optic sensors for structural health monitoring of aircraftcomposite structures: Recent advances and applications. *Sensors*, 15(8):18666–18713, 2015.

[31] Karolina Bednarska, Piotr Sobotka, Tomasz Ryszard Woliński, OliwiaZakrecka, Wiktor Pomianek, Agnieszka Nocoń, and Piotr Lesiak. Hybrid fiber optic sensor systems in structural health monitoring inaircraft structures.*Materials*, 13(10):2249, 2020.

[32] Qiuming Nan, Sheng Li, Yiqiang Yao, Zhengying Li, Honghai Wang, Lixing Wang,and Lizhi Sun. A novel monitoring approach for train tracking and incursion-detection in underground structures based on ultra-weak fbg sensing array. *Sensors*, 19(12):2666, 2019.

[33] YW Wang, YQ Ni, and X Wang. Real-time defect detection of high-speed train wheels by usingbayesian forecasting and dynamic model. *Mechanical Systems and Signal Processing*, 139:, 2020.

[34] Jianping He, Peigang Li, and Shihai Zhang.Continuous deformation measurement for track based on distributedoptical fiber sensor.*Structural monitoring and maintenance*, 7(1):1–12, 2020.

[35] Ahmed F Sayed, Fathy M Mustafa, Ashraf AM Khalaf, and Moustafa H Aly. An enhanced wdm optical communication system using a cascaded fiberbragg grating. *Optical and Quantum Electronics*, 52(3):–21, 2020.

[36] Md Mahiuddin.Development of an oadm to reduce the incoherent crosstalk in wdm-system.*ICT Express*, 2020.

[37] Chee S Goh, Sze Y Set, and Kazuro Kikuchi. Widely tunable optical filters based on fiber bragg gratings. *IEEE photonics technology letters*, 14(9):–1308, 2002.

[38] Jun Huang, Duc Truong Pham, Chunqian Ji, Zechao Wang, and Zude Zhou. Multi-parameter dynamical measuring system using fibre bragg gratingsensors for industrial hydraulic piping. *Measurement*, 134:226–235, 2019.

[39] Chiranjit Ghosh and Vishnu Priye. Dispersion compensation in a 24× 20 gbps dwdm system bycascaded chirped fbgs. *Optik*, 164:335–344, 2018.

[40] David B Talam, El-Sayed A El-Badawy, Hossam MH Shalaby, and Moustafa H Aly. Edfa gain flattening using fiber bragg gratings employing differenthost materials. *Optical and Quantum Electronics*, 52(3):–17, 2020.

[41] Carlo Edoardo Campanella, Antonello Cuccovillo, Clarissa Campanella, AbdulkadirYurt, and Vittorio Passaro. Fibre bragg grating based strain sensors: review of technology andapplications. *Sensors*, 18(9):3115, 2018.

[42] CR Liao and DN Wang. Review of femtosecond laser fabricated fiber bragg gratings for hightemperature sensing. *Photonic Sensors*, 3(2):97–101, 2013.

[43] Rongqing Hui and Maurice O'Sullivan. *Fiber optic measurement techniques*. Academic Press, 2009.

[44] Turan Erdogan. Fiber grating spectra. *Journal of lightwave technology*, 15(8):–1294, 1997.

[45] Jasjot K Sahota, Neena Gupta, and Divya Dhawan. Fiber bragg grating sensors for monitoring of physical parameters: acomprehensive review. *Optical Engineering*, 59 (6):060901, 2020.

[46] Frédéric Monet, Sébastien Loranger, Victor Lambin-Iezzi, AntoineDrouin, Samuel Kadoury, and Raman Kashyap. The rogue: a novel, noise-generated random grating. *Optics express*, 27(10):13895–13909, 2019.

[47] Bai-Ou Guan, Yang Ran, Fu-Rong Feng, and Long Jin. Formation and applications of the secondary fiber bragg grating. *Sensors*, 17(2):398, 2017.

[48] Eric Lindner, Christoph Chojetzki, Sven Brückner, Martin Becker, ManfredRothhardt, and Hartmut Bartelt. Thermal regeneration of fiber bragg gratings in photosensitivefibers. *Optics express*, 17(15):12523–12531, 2009.

[49] Sher Shermin A Khan and Md Saiful Islam. Determination of the best apodization function and grating length oflinearly chirped fiber bragg grating for dispersion compensation. *JCM*, 7(11):840–846, 2012.

[50] Daniele Tosi. Review of chirped fiber bragg grating (cfbg) fiber-optic sensors andtheir applications. *Sensors*, 18(7):2147, 2018.

[51] JS Leng, Wei Zhang, and John AR Williams. Optimization of superstructured fiber bragg gratings for microwavephotonic filters response. *IEEE Photonics technology letters*, 16(7):–1738, 2004.

[52] Y Nasu and S Yamashita. Multiple phase-shift superstructure fibre bragg grating for dwdmsystems. *Electronics Letters*, 37(24):1471–1472,2001.

[53] Srivastava Deepa and Bhargab Das. Interrogation techniques for π-phase-shifted fiber bragg gratingsensor: A review. *Sensors and Actuators A: Physical*, page 112215, 2020.

[54] Zhihong Li, Zhuying Yu, Yubing Shen, Xiukai Ruan, and Yuxing Dai. Graphene enhanced leaky mode resonance in tilted fiber bragg grating:a new opportunity for highly sensitive fiber optic sensor. *IEEE Access*, 7:26641–26651, 2019.

[55] Georgios Violakis, Maria Konstantaki, and Stavros Pissadakis. Accelerated recording of negative index gratings in ge-doped opticalfibers using 248-nm 500-fs laser radiation. *IEEE photonics technology letters*, 18(10):–1184, 2006.

[56] L Dong and WF Liu. Thermal decay of fiber bragg gratings of positive and negative indexchanges formed at 193 nm in a boron-codoped germanosilicate fiber. *Applied optics*, 36(31):8222–8226, 1997.

[57] K Cook, AAP Pohl, and J Canning.High-temperature type iia gratings in 12-ring photonic crystal fibrewith germanosilicate core.*Journal of the European Optical Society-Rapid Publications*, 3,2008.

[58] Yang Ran, Long Jin, Shuai Gao, Li-Peng Sun, Yun-Yun Huang, Jie Li, and Bai-OuGuan. Type iia bragg gratings formed in microfibers. *Optics letters*, 40(16):3802–3805,2015.

[59] Steven Trpkovski, Daniel J Kitcher, Gregory W Baxter, Stephen F Collins, and-Scott A Wade. High-temperature-resistant chemical composition bragg gratings in er3+-doped optical fiber. *Optics letters*, 30(6):607–609, 2005.

[60] Yang Ran, Fu-Rong Feng, Yi-Zhi Liang, Long Jin, and Bai-Ou Guan. Type iia bragg grating based ultra-short dbr fiber laser with hightemperature resistance. *Optics Letters*, 40(24):5706–5709,2015.

[61] Fu-Rong Feng, Yang Ran, Yi-Zhi Liang, Shuai Gao, Yuan-Hua Feng, Long Jin, andBai-Ou Guan. Thermally triggered fiber lasers based on secondary-type-in bragggratings. *Optics Letters*, 41(11):2470–2473,2016.

[62] Fu-Rong Feng, Tong Liu, Peng Xiao, Yang Ran, Hao Liang, Long Jin, and Bai-OuGuan. 1-μm-wavelength ytterbium-doped fiber laser based on the thirdharmonic reflection in secondary-type-in bragg gratings. *Optics letters*, 41(21):4999–5002,2016.

[63] Raman Kashyap. *Fiber bragg gratings*. Academic press, 2009.

[64] Dhanalakshmi Samiappan, AVS Kesarikiran, Venkatesh Chakravartula, CR UmaKumari, Kumar Shubham, Bolisetty Aakash, and R Kumar. Enhancing sensitivity of

fiber bragg grating-based temperaturesensors through teflon coating. *Wireless Personal Communications*, 110(2):–604, 2020.

[65] Elton Soares de Lima Filho, Mohamad Diaa Baiad, Mathieu Gagné, and RamanKashyap.Fiber bragg gratings for low-temperature measurement.*Optics Express*, 22(22):27681–27694, 2014.

[66] R Mahakud, J Kumar, O Prakash, and SK Dixit. Study of the nonuniform behavior of temperature sensitivity in bareand embedded fiber bragg gratings: experimental results and analysis.*Applied optics*, 52(31):7570–7579, 2013.

[67] Gordon MH Flockhart, Robert RJ Maier, James S Barton, William N MacPherson,Julian DC Jones, Karen E Chisholm, Lin Zhang, Ian Bennion, Ian Read, andPeter D Foote. Quadratic behavior of fiber bragg grating temperature coefficients. *Applied optics*, 43(13):2744–2751, 2004.

[68] Grigory Adamovsky, Sergei F Lyuksyutov, Jeffrey R Mackey, Bertram M Floyd,Ujitha Abeywickrema, Igor Fedin, and Mindaugas Rackaitis. Peculiarities of thermo-optic coefficient under different temperatureregimes in optical fibers containing fiber bragg gratings.*Optics Communications*, 285(5):766–773,2012.

[69] Suchandan Pal, Tong Sun, Kenneth TV Grattan, Scott A Wade, Stephen F Collins,Gregory W Baxter, Bernard Dussardier, and Gérard Monnom. Non-linear temperature dependence of bragg gratings written indifferent fibres, optimised for sensor applications over a wide range oftemperatures.*Sensors and Actuators A: Physical*, 112(2-3):211–219, 2004.

[70] Toru Mizunami, Hiroaki Tatehata, and Hideo Kawashima.High-sensitivity cryogenic fibre-bragg-grating temperature sensorsusing teflon substrates.*Measurement Science and Technology*, 12(7):, 2001.

[71] Saidi Parne, RLN Sai Prasad, Sen Gupta Dipankar, M Sai Shankar, andSrimannarayana Kamineni. Polymer-coated fiber bragg grating sensor for cryogenic temperaturemeasurements. *Microwave and optical technology letters*, 53(5):1154–1157, 2011.

[72] Meng-Chou Wu, Ruth H Pater, and Stanton L DeHaven. Effects of coating and diametric load on fiber bragg gratings ascryogenic temperature sensors. In *Smart Sensor Phenomena, Technology, Networks, and Systems2008*, volume 6933, page 693303. International Society for Optics andPhotonics, 2008.

[73] Max B Reid and Meric Ozcan. Temperature dependence of fiber optic bragg gratings at lowtemperatures. *Optical Engineering*, 37(1):237–240, 1998.

[74] Meenu Ahlawat, Bachir Saoudi, Elton Soares de Lima Filho, Michael R Wertheimer,and Raman Kashyap. Use of an fbg sensor for in-situ temperature measurements of gasdielectric barrier discharges. In *Bragg Gratings, Photosensitivity, and Poling in GlassWaveguides*, pages BTu2E–4. Optical Society of America, 2012.

[75] H Yamada, Y Tanaka, M Ogata, K Mizuno, K Nagashima, S Okumura, and Y Terada. Measurement and improvement of characteristics using optical fibertemperature sensors at cryogenic temperatures. *Physica C: Superconductivity and its Applications*,471(21-22):1570–1575, 2011.

[76] Wen Zhang, Wei Zhuang, Mingli Dong, Lianqing Zhu, and Fanyong Meng. Dual-parameter optical fiber sensor for temperature and pressurediscrimination featuring cascaded tapered-fbg and ball-efpi. *IEEE Sensors Journal*, 19(14):5645–5652,2019.

[77] Chen Zhu, Rex E Gerald, and Jie Huang. Progress towards sapphire optical fiber sensors for high-temperatureapplications. *IEEE Transactions on Instrumentation and Measurement*,69(11):8639–8655, 2020.

[78] Te-Ching Hsiao, Tso-Sheng Hsieh, Yi-Chian Chen, Shyh-Chour Huang, and Chia-ChinChiang. Metal-coated fiber bragg grating for dynamic temperature sensor. *Optik*, 127(22):10740–10745, 2016.

[79] Fengqin Huang, Tao Chen, Jinhai Si, Xuantung Pham, and Xun Hou. Fiber laser based on a fiber bragg grating and its application inhigh-temperature sensing. *Optics Communications*, 452:233–237,2019.

[80] Jianyu He, Liyun Ding, Jun Cai, Wenjie Zhu, and Jixiang Dai. A novel high temperature resistant mo-cu functional gradient coatingfor optic fiber bragg grating. *Results in Physics*, 14:102456, 2019.

[81] Yani Zhang, Dun Qiao, Yuyu Zhu, and Peng Jiang.High-order fiber bragg grating fabricated by femtosecond laser pulsesfor high-sensitivity temperature and strain sensing. *Optik*, 222:165423, 2020.

[82] Jitendra Kumar, Om Prakash, Sachin Kumar Agrawal, Ramakanta Mahakud, AnaghaMokhariwale, Sudhir K Dixit, and Shankar V Nakhe. Distributed fiber bragg grating sensor for multipoint temperaturemonitoring up to 500 c in high-electromagnetic interference environment. *Optical Engineering*, 55(9):090502, 2016.

[83] Shuo Yang, Daniel Homa, Hanna Heyl, Logan Theis, John Beach, Billy Dudding,Glen Acord, Dwyn Taylor, Gary Pickrell, and Anbo Wang. Application of sapphire-fiber-bragg-grating-based multi-pointtemperature sensor in boilers at a commercial power plant. *Sensors*, 19(14):3211, 2019.

[84] Glenn N Merberg and James A Harrington. Optical and mechanical properties of single-crystal sapphire opticalfibers. *Applied optics*, 32(18):3201–3209, 1993.

[85] Hui Chen, Michael Buric, Paul R Ohodnicki, Jinichiro Nakano, Bo Liu, andBenjamin T Chorpening. Review and perspective: Sapphire optical fiber cladding developmentfor harsh environment sensing. *Applied Physics Reviews*, 5(1):011102,2018.

[86] Qi Guo, Yong-Sen Yu, Zhong-Ming Zheng, Chao Chen, Peng-Long Wang, Zhen-NanTian, Yang Zhao, Xin-Yu Ming, Qi-Dai Chen, Han Yang, et al. Femtosecond laser inscribed sapphire fiber bragg grating for hightemperature and strain sensing. *IEEE Transactions on Nanotechnology*, 18:208–211,2019.

[87] Yanhui Zhang and Wenyu Yang. Simultaneous precision measurement of high temperature and largestrain based on twisted fbg considering nonlinearity and uncertainty. *Sensors and Actuators A: Physical*, 239:185–195,2016.

[88] Umesh Sampath, Daegil Kim, Hyunjin Kim, and Minho Song. Polymer-coated fbg sensor for simultaneous temperature and strainmonitoring in composite materials under cryogenic conditions. *Applied optics*, 57(3):492–497, 2018.

[89] Yong Du, Qun Han, Haofeng Hu, Mei Sang, Xueru Zhao, Xiaowei Song, Hongyuan-Wang, and Tiegen Liu. High-sensitivity refractive index and temperature sensor based oncascading fbgs and droplet-like fiber interferometer. *Sensors and Actuators A: Physical*, 299:111631, 2019.

[90] Haiwei Fu, Shuai Wang, Huimin Chang, and Yongtao You. A high resolution and large range fiber bragg grating temperaturesensor with vortex beams. *Optical Fiber Technology*, 60:102369, 2020.

[91] Ching-Yu Hsu, Chia-Chin Chiang, Tso-Sheng Hsieh, Hsiang-Cheng Hsu, Liren Tsai,and Chang-Hsiang Hou. Study of fiber bragg gratings with tin-coated for cryogenictemperature measurement. *Optics & Laser Technology*, 136:106768, 2021.

[92] Raphael AG dos Santos, Arnaldo G Leal-Junior, Moisés RN Ribeiro, Eduardo ABenincá, Carlos AF Marques, Luis Pereira, Paulo Antunes, João HGMCorrêa, Maria J Pontes, Anselmo Frizera Neto, et al. Datacenter thermal monitoring without blind spots: Fbg-basedquasi-distributed sensing. *IEEE Sensors Journal*, 21(8):9869–9876,2021.

[93] Shaohua Deng, Tao Wang, Wei Yu, and Guangtao Lu. A multiplexed fiber bragg grating angle sensor for bolt looseningmonitoring. *IEEE Sensors Journal*, 22(23): 22661–22669,2022.

[94] Yushan Liu, Song Xie, Yuanyuan Zheng, and Xiaozhan Yang. Simultaneous measurement of refractive index and temperature based ontapered no-core fiber cascaded with a fiber bragg grating.*Results in Optics*, 9:100300, 2022.

[95] Ze-Rui Zhang, Yong Zhao, and Lu Cai.High-sensitivity temperature sensor based on transmissive solc-likefilter and cascaded fiber bragg grating. *IEEE Sensors Journal*, 23(6):5585–5592,2023.

[96] Shaode Li, Wei He, Qimeng Tan, Haochong Liu, Zhihan Li, and Lianqing Zhu.High temperature and strain dual-parameters fiber sensing based onintermodal interference and femtosecond laser fabricated fiber bragg grating.*Physica Scripta*, 98(5):055505, 2023.

[97] Tobias Habisreuther, Tino Elsmann, Zhiwen Pan, Albrecht Graf, ReinhardtWillsch, and Markus A Schmidt. Sapphire fiber bragg gratings for high temperature and dynamictemperature diagnostics.*Applied Thermal Engineering*, 91:860–865, 2015.

[98] Cristian Vendittozzi, Ferdinando Felli, and Carla Lupi. Modeling fbg sensors sensitivity from cryogenic temperatures to roomtemperature as a function of metal coating thickness.*Optical Fiber Technology*, 42:84–91, 2018.

[99] KS Vasu, S Asokan, AK Sood, et al. Enhanced strain and temperature sensing by reduced graphene oxidecoated etched fiber bragg gratings. *Optics letters*, 41(11): 2604–2607, 2016.

[100] Jitendra Kumar, Gitender Singh, Manoj K Saxena, Om Prakash, Sudhir K Dixit, andShankar V Nakhe.Development and studies on fbg temperature sensor for applications innuclear fuel cycle facilities.*IEEE Sensors Journal*, 2020.

[101] Andreas Othonos. Fiber bragg gratings. *Review of scientific instruments*, 68(12):–4341, 1997.

[102] Daniele Tosi. Review and analysis of peak tracking techniques for fiber bragggrating sensors. *Sensors*, 17(10):2368, 2017.

[103] Yong Zheng, Zheng-Wei Zhu, Wang Xiao, and Quan-Xiang Deng. Review of fiber optic sensors in geotechnical health monitoring. *Optical Fiber Technology*, 54:102127, 2020.

[104] Aydin Rajabzadeh, Richard Heusdens, Richard C Hendriks, and Roger M Groves. Calculation of the mean strain of smooth non-uniform strain fieldsusing conventional fbg sensors. *Journal of Lightwave Technology*, 36(17):–3725, 2018.

[105] M Kharshiduzzaman, A Gianneo, and A Bernasconi. Experimental analysis of the response of fiber bragg grating sensorsunder non-uniform strain field in a twill woven composite. *Journal of Composite Materials*, 53(7):–908, 2019.

[106] Hang-yin Ling, Kin-tak Lau, Li Cheng, and Kwok-wing Chow. Embedded fibre bragg grating sensors for non-uniform strain sensingin composite structures. *Measurement science and technology*, 16(12):, 2005.

[107] Alan D Kersey, Michael A Davis, Heather J Patrick, Michel LeBlanc, KP Koo,CG Askins, MA Putnam, and E Joseph Friebele. Fiber grating sensors. *Journal of lightwave technology*, 15(8):–1463, 1997.

[108] Simon Pevec and Denis Donlagić. Multiparameter fiber-optic sensors: a review. *Optical Engineering*, 58(7):072009,2019.

[109] CE Campanella. Coupled π-shifted fibre bragg grating ring resonant strainsensors. *Electronics Letters*, 52(22):1873–1875,2016.

[110] P Malara, CE Campanella, A Giorgini, S Avino, and G Gagliardi. Fiber bragg grating laser sensor with direct radio-frequency readout. *Optics Letters*, 41(7):1420–1422, 2016.

[111] Carlo Edoardo Campanella, Lorenzo Mastronardi, Francesco De Leonardis, Pietro-Malara, Gianluca Gagliardi, and Vittorio MN Passaro. Investigation of fiber bragg grating based mode-splitting resonantsensors. *Optics express*, 22(21):25371–25384,2014.

[112] P Malara, L Mastronardi, CE Campanella, A Giorgini, S Avino, VMN Passaro, andG Gagliardi. Split-mode fiber bragg grating sensor for high-resolution staticstrain measurements. *Optics letters*, 39(24):6899–6902, 2014.

[113] P Malara, CE Campanella, F De Leonardis, A Giorgini, S Avino, VMN Passaro, andG Gagliardi. Enhanced spectral response of π-phase shifted fiber bragggratings in closed-loop configuration. *Optics Letters*, 40(9):2124–2126, 2015.

[114] Carlo Edoardo Campanella, CM Campanella, Francesco De Leonardis, andVittorio MN Passaro. Ii-shifted fiber bragg grating ring resonator as a splitting moderesonant sensor. In *20th IMEKO TC4 Int. Symp*, pages 414–419,2014.

[115] CE Campanella, A Giorgini, S Avino, P Malara, R Zullo, G Gagliardi, andP De Natale. Localized strain sensing with fiber bragg-grating ring cavities. *Optics express*, 21 (24):29435–29441, 2013.

[116] Biswajit Ghosh and Sanjoy Mandal. Mathematical modeling of π-phase-shifted fiber bragg grating andits application for strain measurement in epoxy resin cantilever beam. *IEEE Sensors Journal*, 2020.

[117] A Lamberti, S Vanlanduit, B De Pauw, and F Berghmans. A novel fast phase correlation algorithm for peak wavelengthdetection of fiber bragg grating sensors. *Optics Express*, 22(6):7099–7112, 2014.

[118] Daniele Tosi. Klt-based algorithm for sub-picometer accurate fbg tracking withcoarse wavelength sampling. *IEEE Photonics Technology Letters*, 27(20):–2137, 2015.

[119] Jiwen Cui, Yang Hu, Kunpeng Feng, Junying Li, and Jiubin Tan. Fbg interrogation method with high resolution and response speedbased on a reflective-matched fbg scheme. *Sensors*, 15(7):16516–16535, 2015.

[120] Rui Cheng, Li Xia, Yanli Ran, Jalal Rohollahnejad, Jiaao Zhou, and YongqiangWen. Interrogation of ultrashort bragg grating sensors using shiftedoptical gaussian filters. *IEEE Photonics Technology Letters*, 27(17):–1836, 2015.

[121] Hongjie Zhang, Qiuliang Wang, Housheng Wang, Shousen Song, Baozhi Zhao, YinmingDai, Guojun Huang, and Zhonghua Jiang. Fiber bragg grating sensor for strain sensing in low temperaturesuperconducting magnet. *IEEE Transactions on Applied Superconductivity*, 20(3):1798–1801, 2010.

[122] Wu Yuan, Alessio Stefani, and Ole Bang. Tunable polymer fiber bragg grating (fbg) inscription: fabrication ofdual-fbg temperature compensated polymer optical fiber strain sensors. *IEEE Photonics Technology Letters*, 24(5):–403, 2011.

[123] Zuyuan He, Qingwen Liu, and Tomochika Tokunaga. Ultrahigh resolution fiber-optic quasi-static strain sensors forgeophysical research. *Photonic Sensors*, 3(4):295–303, 2013.

[124] Marta S Ferreira, Jörg Bierlich, Martin Becker, Kay Schuster, José LSantos, and Orlando Frazão. Ultra-high sensitive strain sensor based on post-processed opticalfiber bragg grating. *Fibers*, 2(2):142–149, 2014.

[125] Yupeng Wang, Xueguang Qiao, Hangzhou Yang, Dan Su, Ling Li, and Tuan Guo. Sensitivity-improved strain sensor over a large range of temperaturesusing an etched and regenerated fiber bragg grating. *Sensors*, 14(10):18575–18582, 2014.

[126] Kishore Bhowmik, Gang-Ding Peng, Yanhua Luo, Eliathamby Ambikairajah, VedranLovric, William R Walsh, and Ginu Rajan. High intrinsic sensitivity etched polymer fiber bragg grating pairfor simultaneous strain and temperature measurements. *IEEE Sensors Journal*, 16(8):2453–2459,2016.

[127] Lei Zhang, Xinlong Chang, Youhong Zhang, and Fan Yang. Large strain detection of srm composite shell based on fiber bragggrating sensor. *Photonic Sensors*, 7(4): 350–356, 2017.

[128] Tingting Yang, Xueguang Qiao, Qiangzhou Rong, and Weijia Bao. Fiber bragg gratings inscriptions in multimode fiber using 800 nmfemtosecond laser for high-temperature strain measurement. *Optics & Laser Technology*, 93:138–142, 2017.

[129] Hongli Xiang and Yajun Jiang. Fiber bragg grating inscription in multi-core photonic crystal fiberby femtosecond laser. *Optik*, 171:9–14, 2018.

[130] Yinggang Liu, Xiaoya Song, Bowen Li, Jingfei Dong, Liang Huang, Dakuan Yu, andDequan Feng. Simultaneous measurement of temperature and strain based on scf-basedmzi cascaded with fbg. *Applied Optics*, 59(30):9476–9481, 2020.

[131] ZhiChao Ding, ZhongWei Tan, YunShu Gao, Yue Wu, and Bin Yin. Strain and temperature discrimination using a fiber bragg gratingconcatenated with panda polarization-maintaining fiber in a fiber loopmirror. *Optik*, 221:165352, 2020.

[132] S Sridhar, Suneetha Sebastian, Ajay K Sood, and Sundarrajan Asokan. A study on mos_2 nanolayer coated etched fiber bragg gratingstrain sensor. *IEEE Sensors Journal*, 21(7):9171–9178,2021.

[133] Ruilei Zhang, Xi Wu, Li Hong, Jiheng Jin, and Guoxi Li. High-sensitivity fiber bragg grating strain sensor of the substratetype. *Applied Optics*, 61(35):10567–10573, 2022.

[134] Wuyi Li, Shi Chen, Yuanyuan Chu, Pengyu Huang, and Guang Yan. Wide-range fiber bragg grating strain sensor for load testing ofaircraft landing gears. *Optik*, 262: 169290, 2022.

[135] Chaoyi Liu, Hailiang Chen, Qiang Chen, Zhigang Gao, Biao Wu, Xiaoya Fan, and-Mingjian Ma. Sagnac interferometer-based optical fiber strain sensor withexceeding free spectral measurement range and high sensitivity. *Optics & Laser Technology*, 159:108935, 2023.

[136] Yen-jie Ee, Zieauddin Kufian, Kok-sing Lim, Kok-soon Tey, Cheong-weng Ooi,Waldo Udos, Zurina Osman, and Harith Ahmad. Highly sensitive vernier sensor based on chirp grating fabry-perotinterferometer (cg-fpi) for the strain detection in lithium polymer (lipo)batteries. *Sensors and Actuators A: Physical*, 350:114080, 2023.

[137] Jing Tian, Mei-jiang Hou, Yang Jiang, Hao Luo, and Chuan-yu Tang.Fiber ring laser cavity for strain sensing via beat frequencydemodulation. *Optics Communications*, 476:126326, 2020.

[138] Teng Guo, Tianxi Zhang, and Xueguang Qiao. Fbg-efpi sensor for large strain measurement with low temperaturecrosstalk. *Optics Communications*, page 125945, 2020.

[139] Fouzia Khan, Abdulhamit Donder, Stefano Galvan, Ferdinando Rodriguez y Baena,and Sarthak Misra. Pose measurement of flexible medical instruments using fiber bragggratings in multi-core fiber.*IEEE Sensors Journal*, 2020.

[140] Xinbo Huang, Long Zhao, Ziliang Chen, and Cheng Liu. An online monitoring technology of tower foundation deformation oftransmission lines.*Structural Health Monitoring*, 18(3):–962, 2019.

[141] Ruoshui Tan, Chen Chen, Yongqiu Zheng, Jiamin Chen, and Liyun Wu. High-precision calibration method for fiber bragg grating strainsensing based on an optical lever. *Optical Fiber Technology*, 61:102392, 2021.

[142] Ruiya Li, Yiyang Chen, Yuegang Tan, Zude Zhou, Tianliang Li, and Jian Mao. Sensitivity enhancement of fbg-based strain sensor.*Sensors*, 18(5):1607, 2018.

[143] Mingyao Liu, Wenzhi Wang, Han Song, Shiguang Zhou, and Weijian Zhou. A high sensitivity fbg strain sensor based on flexible hinge. *Sensors*, 19(8):1931, 2019.

[144] Jun Peng, Xing Zhou, Shuhai Jia, Yiming Jin, Shouping Xu, and Jizhong Chen. High precision strain monitoring for lithium ion batteries based onfiber bragg grating sensors. *Journal of Power Sources*, 433:226692, 2019.

[145] Mohsen Mansoursamaei and Abdollah Malakzadeh. Simultaneous measurement of temperature and strain using a singlefiber bragg grating on a tilted cantilever beam. *Optical Review*, 28(3):289–294, 2021.

[146] Selin Ece Kipriksiz and Murat Yücel. Tilted fiber bragg grating design for a simultaneous measurement oftemperature and strain. *Optical and Quantum Electronics*, 53 (1):–15, 2021.

[147] Simon Pevec and Denis Donlagić. Multiparameter fiber-optic sensors: A review. *Optical Engineering*, 58(7):072009,2019.

[148] Kun Yao, Qijing Lin, Zhuangde Jiang, Na Zhao, Bian Tian, and Gang-Ding Peng. Design and analysis of a combined fbg sensor for the measurement ofthree parameters. *IEEE Transactions on Instrumentation and Measurement*,70:1–10, 2021.

[149] Jiaji He, Chennan Hu, Di Hu, and Anbo Wang. High-temperature all-fiber non-destructive multi-parameter sensingsystem with consistent performance. *Optics letters*, 45(7):1722–1725,2020.

[150] Qihao Hu, Pengrui Wang, Binyu Rao, Meng Wang, Zefeng Wang, and Xiaojun Xu. Simultaneous measurement of temperature and strain usingdouble-cladding fiber based hybrid bragg grating. *OSA Continuum*, 3(4):1031–1037, 2020.

[151] Kuikui Guo, Jun He, Laipeng Shao, Gaixia Xu, and Yiping Wang. Simultaneous measurement of strain and temperature by a sawtoothstressor-assisted highly birefringent fiber bragg grating. *Journal of Lightwave Technology*, 38(7):–2066, 2020.

[152] M Divya Shree, A Sangeetha, and Prabu Krishnan. Design and analysis of fbg sensor for explosive detectionapplications. *Plasmonics*, pages 1–7, 2019.

[153] Hacen Khlaifi, Amira Zrelli, and Tahar Ezzedine. Optical fiber sensors in border detection application: Temperature,strain and pressure distinguished detection using fiber bragg grating andfluorescence intensity ratio. *Optik*, 229:166257, 2021.

[154] Mofreh Toba, Fathy M Mustafa, and Tamer M Barakat. New simulation and analysis fiber bragg grating: Narrow bandwidthwithout side lobes. *Journal of Physics Communications*, 4(7):, 2020.

[155] Ahmed F Sayed, Fathy M Mustafa, Ashraf AM Khalaf, and Moustafa H Aly. Spectral width reduction using apodized cascaded fiber bragg gratingfor post-dispersion compensation in wdm optical networks. *Photonic Network Communications*, 41(3):–241, 2021.

[156] Fathy M Mustafa, Mohamed M Abdelhalim, Moustafa H Aly, and Tamer M Barakat. Dispersion compensation analysis of optical fiber link using cascadedapodized fbgs hybrid with maximum time division multiplexing transmissiontechnique. *Optical and Quantum Electronics*, 53(7):–21, 2021.

[157] Fathy M Mustafa, Sayed A Zaky, Ashraf AM Khalaf, and Moustafa H Aly. Chromatic dispersion compensation by cascaded fbg with duobinarymodulation scheme. *Optical and Quantum Electronics*, 54(12):, 2022.

[158] Fathy M Mustafa, Sayed A Zaky, Ashraf AM Khalaf, and Moustafa H Aly. A cascaded fbg scheme based oqpsk/dpsk modulation for chromaticdispersion compensation. *Optical and Quantum Electronics*, 54(7):, 2022.

[159] Fathy M Mustafa, Asmaa Mohamed, Ashraf AM Khalaf, Ahmed F Sayed, and Moustafa HAly. Dispersion compensation using cascaded apodized cfbgs under mt-dmtransmission technique: Enhanced system performance. *Optical and Quantum Electronics*, 55(1):32,2023.

[160] Chaluvadi V Naga Bhaskar, Subhradeep Pal, and Prasant Kumar Pattnaik. Narrow-band optical band-pass filter using dual cascaded chirpedfbgs. *Optik*, page 168979, 2022.

[161] Sanzhar Korganbayev, Yerzhan Orazayev, Sultan Sovetov, Ali Bazyl, EmilianoSchena, Carlo Massaroni, Riccardo Gassino, Alberto Vallan, Guido Perrone,Paola Saccomandi, Michele Arturo Caponero, Giovanna Palumbo, Stefania-Campopiano, Agostino Iadicicco, and Daniele Tosi. Detection of thermal gradients through fiber-optic chirped fiberbragg grating (cfbg): Medical thermal ablation scenario. *Optical Fiber Technology*, 41:48–55, 2018.

[162] Chaluvadi V Naga Bhaskar, M Balasubramanian, Subhradeep Pal, and Prasant KumarPattnaik. Spectral characteristics of cascaded apodized fbgs of varyinglengths. In *2022 Workshop on Recent Advances in Photonics (WRAP)*, pages1–2. IEEE, 2022.

[163] Nazmi A Mohammed, Taha A Ali, Moustafa H Aly, and OSA Member. Evaluation and performance enhancement for accurate fbg temperaturesensor measurement with different apodization profiles in single andquasi-distributed dwdm systems. *Optics and Lasers in Engineering*, 55:22–34, 2014.

[164] Nazmi A Mohammed, Taha A Ali, and Moustafa H Aly. Performance optimization of apodized fbg-based temperature sensors insingle and quasi-distributed dwdm systems with new and different apodizationprofiles. *AIP Advances*, 3(12):122125, 2013.

[165] Govind P Agrawal. *Fiber-optic communication systems*, volume 222. John Wiley & Sons, 2012.

[166] KS Khalid, M Zafrullah, SM Bilal, and MA Mirza. Simulation and analysis of gaussian apodized fiber bragg gratingstrain sensor. *Journal of Optical Technology*, 79 (10):–673, 2012.

[167] Aasif Bashir Dar and Rakesh Kumar Jha. Design and comparative performance analysis of different chirpingprofiles of tanh apodized fiber bragg grating and comparison

with thedispersion compensation fiber for long-haul transmission system. *Journal of Modern Optics*, 64(6):555–566,2017.

[168] Song Gao, Chams Baker, Liang Chen, and Xiaoyi Bao. Fabrication of chirped fiber bragg gratings in a non-uniformsingle-core As_2Se_3-PMMA tapered fiber. *Journal of Lightwave Technology*, 38(15):–4113, 2020.

[169] Aleksandr A Markvart, Leonid B Liokumovich, Iurii O Medvedev, and Nikolai AUshakov.Smartphone-based interrogation of a chirped fbg strain sensorinscribed in a multimode fiber.*Journal of Lightwave Technology*, 39(1):–289, 2021.

[170] E Vorathin, ZM Hafizi, AM Aizzuddin, Muhammad Khairol Annuar Zaini, and-Kok Sing Lim. A novel temperature-insensitive hydrostatic liquid-level sensor usingchirped fbg.*IEEE Sensors Journal*, 19(1):157–162,2018.

[171] Anbhawa Nand, Daniel J Kitcher, Scott A Wade, Thinh B Nguyen, Greg W Baxter,Rhys Jones, and Stephen F Collins. Determination of the position of a localized heat source within achirped fibre bragg grating using a fourier transform technique. *Measurement Science and Technology*, 17(6):, 2006.

[172] S Yashiro, T Okabe, N Toyama, and N Takeda. Monitoring damage in holed cfrp laminates using embedded chirped fbgsensors. *International Journal of Solids and Structures*, 44(2):603–613, 2007.

[173] Ahmed F Sayed, Fathy M Mustafa, Ashraf AM Khalaf, and Moustafa H Aly. Apodized chirped fiber bragg grating for postdispersion compensationin wavelength division multiplexing optical networks.*International Journal of Communication Systems*, 33(14):e4551, 2020.

[174] Gorka Peraita, Adrián J Torregrosa, Haroldo Maestre, and Carlos RFernández-Pousa. Broadband linearization of dispersive delay line using a chirpedfiber bragg grating. *IEEE Photonics Technology Letters*, 27(10):–1047, 2015.

[175] ML Meena and Raj Kumar Gupta. Design and comparative performance evaluation of chirped fbgdispersion compensation with dcf technique for dwdm optical transmissionsystems. *Optik*, 188:212–224, 2019.

[176] Miguel A Preciado, Vctor Garcia-Munoz, and Miguel A Muriel. Grating design of oppositely chirped fbgs for pulse shaping. *IEEE Photonics Technology Letters*, 19 (6):–437, 2007.

[177] Hong Chang, Zhaochen Cheng, Ruoyu Sun, Zhigang Peng, Miao Yu, Yu You, Min Wang,and Pu Wang. 172-fs, 27-μj, yb-doped all-fiber-integrated chirped pulseamplification system based on parabolic evolution by passive spectralamplitude shaping. *Optics express*, 27(23):34103–34112, 2019.

[178] Javier Hervás, Daniele Tosi, Héctor García-Miquel, David Barrera,Carlos R Fernández-Pousa, and Salvador Sales. Klt-based interrogation technique for fbg multiplexed sensortracking. *Journal of Lightwave Technology*, 35(16):–3392, 2016.

[179] Mark Froggatt. Distributed measurement of the complex modulation of a photoinducedbragg grating in an optical fiber. *Applied Optics*, 35(25):5162–5164, 1996.

[180] Mark Froggatt and Jason Moore. High-spatial-resolution distributed strain measurement in opticalfiber with rayleigh scatter. *Applied optics*, 37(10):1735–1740, 1998.

[181] Nai-Hsiang Sun, Jiun-Jie Liau, Yean-Woei Kiang, Shih-Chiang Lin, Ru-Yen Ro,Jung-Sheng Chiang, and Hung-Wen Chang. Numerical analysis of apodized fiber bragg gratings using coupledmode theory. *Progress In Electromagnetics Research*, 99:289–306,2009.

[182] Kyung Shik Lee and Turan Erdogan. Fiber mode coupling in transmissive and reflective tilted fibergratings. *Applied optics*, 39(9):1394–1404, 2000.

[183] Yu-Chun Lu, Wei-Ping Huang, and Shui-Sheng Jian. Full vector complex coupled mode theory for tilted fiber gratings. *Optics express*, 18(2):713–726, 2010.

[184] Jiangang Sang, Zhengtian Gu, Qiang Ling, and Wenbin Feng. Film sensor based on cascaded tilted long-period and tilted fiberbragg grating. *Journal of Optics*, 20(6): 065402, 2018.

[185] Luigi Fazzi, Dmitry Klyukin, and Roger M Groves.Transfer matrix method for fundamental lp01 core mode coupling in atilted fbg sensor.In *AIP Conference Proceedings*, volume 2293, page 200010. AIPPublishing LLC, 2020.

[186] Hongchun Gao, Yi Jiang, Yang Cui, Liuchao Zhang, Jingshan Jia, and Lan Jiang. Investigation on the thermo-optic coefficient of silica fiber withina wide temperature range.*Journal of Lightwave Technology*, 36(24):–5886, 2018.

[187] Ning Yang, Qi Qiu, Jun Su, and Shuang-jin Shi.Research on the temperature characteristics of optical fiberrefractive index. *Optik*, 125(19):5813–5815, 2014.

[188] Yong Guo, Zhi-Yong Wang, Qi Qiu, Jun Su, Yunxiang Wang, Shuangjin Shi, andZhenfang Yu. Theoretical and experimental investigations on the temperature-dependence of the refractive index of amorphous silica. *Journal of Non-Crystalline Solids*, 429:198–201,2015.

[189] Xueguang Qiao, Yupeng Wang, Hangzhou Yang, Tuan Guo, Qiangzhou Rong, Ling Li,Dan Su, Kok-Sing Lim, and Harith Ahmad. Ultrahigh-temperature chirped fiber bragg grating through thermalactivation.*IEEE Photonics Technology Letters*, 27(12): –1308, 2015.

[190] Ravil F Idrisov, Sergey V Varzhel, Andrey V Kulikov, Igor K Meshkovskiy,Manfred Rothhardt, Martin Becker, Kay Schuster, and Hartmut Bartelt.Spectral characteristics of draw-tower step-chirped fiber bragggratings. *Optics & Laser Technology*, 80:112–115, 2016.

[191] V Naga Bhaskar Chaluvadi and Prasant Kumar Pattnaik. Spectral characteristics of cascaded uniform fbgs of varying lengths.In *2020 IEEE 17th India Council International Conference(INDICON)*, pages 1–4. IEEE, 2020.

[192] Sher Shermin Azmiri Khan and Md Saiful Islam. Performance evaluation of different apodization profiles of linearlychirped fbg for dispersion compensation. In *14th International Conference on Computer and InformationTechnology (ICCIT 2011)*, pages 350–354. IEEE, 2011.

[193] Pei Li, Jian Shuisheng, Ning Tigang, Wang Zhi, et al. Long-haul wdm system through conventional single mode optical fiberwith dispersion compensation by chirped fiber bragg grating. *Optics communications*, 222(1-6):169–178,2003.

[194] Deepika Meena and ML Meena. Design and analysis of novel dispersion compensating model with chirpfiber bragg grating for long-haul transmission system. In *Optical and Wireless Technologies*, pages 29–36. Springer,2020.

[195] F Matera and M Settembre. Role of q-factor and of time jitter in the performance evaluation ofoptically amplified transmission systems. *IEEE Journal of Selected Topics in Quantum Electronics*,6(2):308–316, 2000.

[196] CT Manimegalai, Himanshu Thakur, Hemanga Bhatta, and Afaan Iliyas. Analysis of data transmission in underwater optical wirelesscommunication in vertical channels. *Journal of Optics*, pages 1–9, 2022.

[197] Karin Ennser, N Zervas, and RL Laming. Optimization of apodized linearly chirped fiber gratings for opticalcommunications. *IEEE Journal of Quantum Electronics*, 34 (5):–778, 1998.

[198] Fathy M Mustafa, Ahmed F Sayed, and Moustafa H Aly. A reduced power budget and enhanced performance in a wdm system: anew fbg apodization function. *Optical and Quantum Electronics*, 54(8):–15, 2022.

[199] Subhradeep Pal, Abhishek Kumar, and Sumanta Gupta. Pam-4 generation using an electrostatic doping aided single siliconmicroring modulator driven by two binary electrical signals. *Optik*, 231:166373, 2021.

Publications Related to this Thesis

Journals:

- Chaluvadi V Naga Bhaskar, Subhradeep Pal, Prasant Kumar Pattnaik, "Performance enhancement of optical communication system with cascaded FBGs of varying lengths," in Journal of Optics, vol. 25, no. 12, pp.1-13, 2023.DOI: https://doi.org/10.1088/2040-8986/ad0def

- Chaluvadi V Naga Bhaskar, Subhradeep Pal, Prasant Kumar Pattnaik, "Narrow-band optical band-pass filter using dual cascaded chirped FBGs," in Optik-International Journal for Light and Electron Optics, vol. 262, pp. 168979, 2022.
  DOI: https://doi.org/10.1016/j.ijleo.2022.168979

- Chaluvadi V Naga Bhaskar, Subhradeep Pal, Prasant Kumar Pattnaik, "Recent advancements in fiber Bragg gratings based temperature and strain measurement," in Results in Optics, vol. 5, pp. 100130, 2021,DOI: https://doi.org/10.1016/j.rio.2021.100130

Conferences:

- Chaluvadi V Naga Bhaskar, Balasubramanian M, Subhradeep Pal, Prasant Kumar Pattnaik, "Spectral characteristics of cascaded FBGs with Hyperbolic Tangent apodization," in IEEE 6^{th} conference on Information and Communication Technology (CICT), November 18-20, 2022, Gwalior, India,DOI: 10.1109/CICT56698.2022.9997816

- Chaluvadi V Naga Bhaskar, M Balasubramanian, Subhradeep Pal, Prasant Kumar Pattnaik, "Spectral characteristics of cascaded apodized FBGs of varying lengths," in IEEE Workshop on Recent Advances in Photonics (WRAP), March 04-06, 2022, Mumbai, India,DOI: 10.1109/WRAP54064.2022.9758212

- V Naga Bhaskar Chaluvadi, Prasant Kumar Pattnaik, "Spectral characteristics of cascaded uniform FBGs of varying lengths," in IEEE 17^{th} India Council International Conference (INDICON), December 10-13, 2020, New Delhi, India,DOI: 10.1109/INDICON49873.2020.9342515

- V Naga Bhaskar Chaluvadi, Prasant Kumar Pattnaik, "Effect of strain and temperature on FBG," in IEEE 6^{th} International conference on Electronics, Computing and Communication Technologies (CONNECT) July 02-04, 2020, Bangalore, India,DOI: 10.1109/CONECCT50063.2020.9198339

Appendix A

The following are some implications and benefits of implementing apodized, chirped fiber Bragg gratings (FBGs) and cascaded FBGs utilizing the transfer matrix method (TMM) code:

1. **Accurate Modeling:** TMM provides a rigorous mathematical framework for modeling light propagation through complex FBG structures. By accurately representing the interaction between light and the grating structure, TMM-based simulations can predict the spectral response of apodized, chirped FBGs, and cascaded FBGs with high precision.

2. **Design Flexibility:** TMM allows for the design and optimization of FBG structures with tailored spectral characteristics. Designers can optimize parameters such as apodization profiles, chirp rates, and cascading configurations to achieve desired spectral shaping, dispersion compensation, or other specific requirements.

3. **Performance Optimization:** Using TMM-based simulations, one can optimize the performance of apodized, chirped FBGs, and cascaded FBGs for various applications. Optimization algorithms can be employed to maximize key performance metrics such as reflection bandwidth, dispersion compensation efficiency, or spectral shape fidelity.

4. **Understanding Physical Mechanisms:** Implementing FBG designs using TMM provides insights into the physical mechanisms governing their behavior. Researchers

can analyze how variations in grating parameters affect spectral responses, dispersion properties, and other performance characteristics, leading to a deeper understanding of FBG behavior.

5. **Simulation of Realistic Structures:** TMM-based simulations enable the virtual prototyping of complex FBG structures that may be challenging or costly to fabricate experimentally. Designers can explore a wide range of design parameters and configurations, gaining valuable insights into the feasibility and performance of proposed FBG designs.

6. **Time and Cost Savings:** TMM-based simulations offer a cost-effective alternative to experimental testing, allowing designers to iterate and optimize FBG designs efficiently in a virtual environment. This can lead to significant time and cost savings in the product development cycle.

Biography of the Candidate

Chaluvadi V Naga Bhaskar received his B-Tech degree in Electronics and Communication Engineering in 2011 and then completed his M-Tech in Communication Systems in 2014. He was associated with academics as an Assistant Professor from 2015 to 2019. Now he is pursuing his Ph.D in Photonics at Birla Institute of Technology and Science, Pilani, Hyderabad campus, India. He received an excellence in research award for presenting his research work in the sixth symposium conducted by the department of EEE, BITS Pilani, Hyderabad campus in 2022. He has been awarded as Best Teacher for excellence in teaching while working as an Assistant professor at Laki Reddy Bali Reddy College of Engineering, Andhra Pradesh. Also, he was awarded as a topper for the NPTEL online certification courses on Spread Spectrum Communications and Jamming in 2017 and Fiber Optics in 2018, conducted by IIT Kharagpur and IIT Roorkee, respectively. His main research interests are optical communication and FBG assisted optical devices for sensing and communications.

Biography of the Supervisor

Prasant Kumar Pattnaik is currently an Associate Professor with the Department of Electrical and Electronics Engineering BITS-Pilani, Hyderabad campus. Prior to this, he was Assistant Professor in the same department. Before joining BITS, he has worked as a Specialist, Design and Development at Tata Elxsi Ltd., Bangalore, and as a Post-Doctoral Research Associate at Indian Institute of Science, Bangalore.He did his BSc (Physics), M.Sc (Physics) and M.Tech (Applied Optics) from Sri Sathya Sai Institute of Higher Learning, Prasanthinilayam, India in 1993, 1995 and 1997 respectively.

He did his Ph.D in Electrical Communication Engineering from Indian Institute of Science, Bangalore in 2005. His main research interests are in Photonic Integrated Circuits, Optical Communication, MEMS and MOEMS, Microfluidics and Photonic Devices for Sensors and Communication. He has authored more than 80 papers in international journals and conferences. Also, he has filed five indian patents in the area of optical networking, multimedia communication, embedded devices and microfluidics. He has implemented a sponsored project from DST, Govt. of India. He has supervised/supervising 7 PhD students, several Masters and Bachelors students. He is member of IEEE and has been a reviewer of many IEEE, Elsevier, IOP and SPIE journals.

He was recipient of the University Gold Medal both in M.Sc (Physics) and M.Tech (Applied Optics). He received the Outstanding Potential for Excellence in Research and Academics (OPERA) Award from BITS Pilani in 2015.

Biography of the Co-Supervisor

Subhradeep Pal is presently working as an Assistant Professor in the Department of EEE, BITS-Pilani, Hyderabad Campus since 2020. He received the B.Tech.degree from the West Bengal University of Technology, Kolkata, India, in 2009, and the M.Tech. degree from the Indian Institute of Technology (IIT) Kharagpur, West Bengal, India, in 2013. In 2014, he joined the Department of Electrical Engineering, Indian Institute of Technology, Patna, India, as a Research Scholar, in the field of optical communication. His research interests include photodetectors, photonic integrated circuits, silicon photonic devices, high-speed optical transmission systems, memristor, and sensors.